Bachelor Thesis in Physics

submitted to the

Department of Physics and Astronomy

on

October 7, 2021

by

Jakob Stricker

Heidelberg University – Physikalisches Institut

stricker@physi.uni-heidelberg.de

Testing of a Method for the Sensor Thickness Determination and a Cluster Size Study for the MuPix10

under the supervision of

Prof. Dr. André Schöning

Abstract

The intent of this thesis is to characterize the *MuPix10* pixel sensor – a high-voltage monolithic active pixel sensor (HV-MAPS) prototype for the sensor that is planned to be used for particle tracking in the Mu3e experiment. The Mu3e experiment searches for the lepton-flavor violating decay $\mu^+ \to e^+e^+e^-$, which is highly suppressed to an unobservable order in the Standard Model of Particle Physics. Thus, its observation would point to physics beyond the Standard Model.
To identify such a decay an elaborate detector system has been developed in order to be capable of detecting the searched-for event and distinguish it from background events. The newly developed HV-MAPS are characterized and their performance is analyzed on testbeam campaigns by using a multi-layer telescope setup. In the scope of this thesis, the sensor performance data taken in a testbeam at DESY is analyzed.
A model for the formation of particle hit clusters on the MuPix10 has been developed by assuming diffusion of the generated charge carriers during the drift collection time. This model is introduced and its predictions are compared to results from the testbeam and discussed critically.
Furthermore, different models for the energy deposition distribution ("*straggling functions*") in a thin silicon detector are presented and the possibility to determine the sensor thickness from the shape of these functions has been tested. The results are discussed in view of the data obtained at the DESY-testbeam.

Zusammenfassung

Das Ziel der vorliegenden Arbeit ist die Charakterisierung des *MuPix10* Pixelsensors – eines hochspannungsbetriebenen monolithischen aktiven Pixelsensor (HV-MAPS)-Prototypen des Sensors, der für die Bestimmung von Teilchenspuren im Mu3e-Experiment zur Verwendung kommen soll. Das Mu3e-Experiment sucht nach dem Zerfall $\mu^+ \to e^+e^+e^-$, der die Erhaltung der Lepton-Familienzahl verletzt und im Standardmodell der Teilchenphysik ins Unbeobachtbare unterdrückt ist. Seine Beobachtung wäre damit ein Indiz für Physik jenseits des Standardmodells.
Um einen solchen Zerfall ausmachen zu können, wurde ein ausgeklügeltes Detektor-System entwickelt, das in der Lage ist, den gesuchten Zerfall zu detektieren und von Hintergrundereignissen zu unterscheiden. Die neu entwickelten HV-MAPS können auf Testbeam-Kampagnen, unter Verwendung eines aus mehreren Sensorlagen bestehenden Teleskops, charakterisiert und auf ihre Leistung untersucht werden. Im Rahmen dieser Arbeit werden Daten analysiert, die im Zuge eines Testbeams am DESY genommen wurden um die Leistung der Sensoren beurteilen zu können.

Unter der Annahme von Diffusion der bei einem Teilchen-Hit im Sensor generierten Ladung während deren Sammlung im elektrischen Driftfeld wurde ein Modell zur Beschreibung der Formation von Hit-Clustern entwickelt. Dieses Modell wird hier vorgestellt und die Vorhersagen, die es macht, werden verglichen mit Ergebnissen, die auf dem Testbeam erhalten wurden und außerdem in Hinblick auf diese kritisch diskutiert.
Des Weiteren werden verschiedene Modelle für die Verteilung der Energiedeposition in dünnen Silizium-Detektoren, sogenannte *straggling functions*, vorgestellt und die Möglichkeit, die Form dieser zu nutzen, um die Dicke der Sensoren zu bestimmen, wurde untersucht. Die Ergebnisse werden mit Blick auf die Daten des DESY-Testbeams diskutiert.

CONTENTS

Introduction

Experimental setup

Analysis and Models

Results

Conclusion

Appendix

Introduction

1. Motivation

It has been in the nature of humans to understand the surrounding world to take advantage of this understanding, as well as to just get the satisfaction from the knowledge – as has been pointed out in Goethe's *Faust*

> *„Dass ich erkenne, was die Welt*
> *Im Innersten zusammenhält“*

To „see, what holds the universe at its innermost parts“ mankind has made great effort – in the theoretical describing of ongoing processes in nature and also in their experimental observations.
This interplay between theory and experiment is very much likely to be as old as science itself.
Observations in nature are to be described by a theory and the theory should agree with all observations. If the latter is not the case, the theory has to be enhanced or new theories need to be put forward. It is therefore the aim of physical experiments to find limitations of current theories and hereby push the precision of our understanding of the universe to higher and higher accuracy or even find a point at which a theory completely fails and new physics can be found.

The *Mu3e* experiment, introduced in Section 3, is just such an experiment, searching for physics beyond the Standard Model, presented in Section 2. High precision particle tracking and vertexing is required for this experiment and is to be provided by high-voltage monolithic active pixel sensors (HV-MAPS). Extensive R&D is conducted in order to design such a sensor fully capable of dealing with the requirements set by the experiment. As such, dedicated testbeams campaigns can be undertaken with the aim of the characterization of recently developed sensors. Data taken at these testbeams can amount to several Terabyte from which essential conclusions on the sensor performance have to be drawn by extracting information that can be compared to expectations and model predictions. In turn, the information gathered on the performance allows for further improvement and development of the sensor needed for the final experiment.

2. The Standard Model of Particle Physics

The *Standard Model of Particle Physics* (SM) is one of the most precisely trialed theories in physics with respect to its prediction accuracy. Not only is it a theory to describe the world on a subatomic scale, but it also had the power to predict the existence of particles. The high variety of particles and their properties it is predicting and describing can be attributed to comparatively few elementary particles (see Figure 2.1). Those particles can be structured with regard to certain properties.

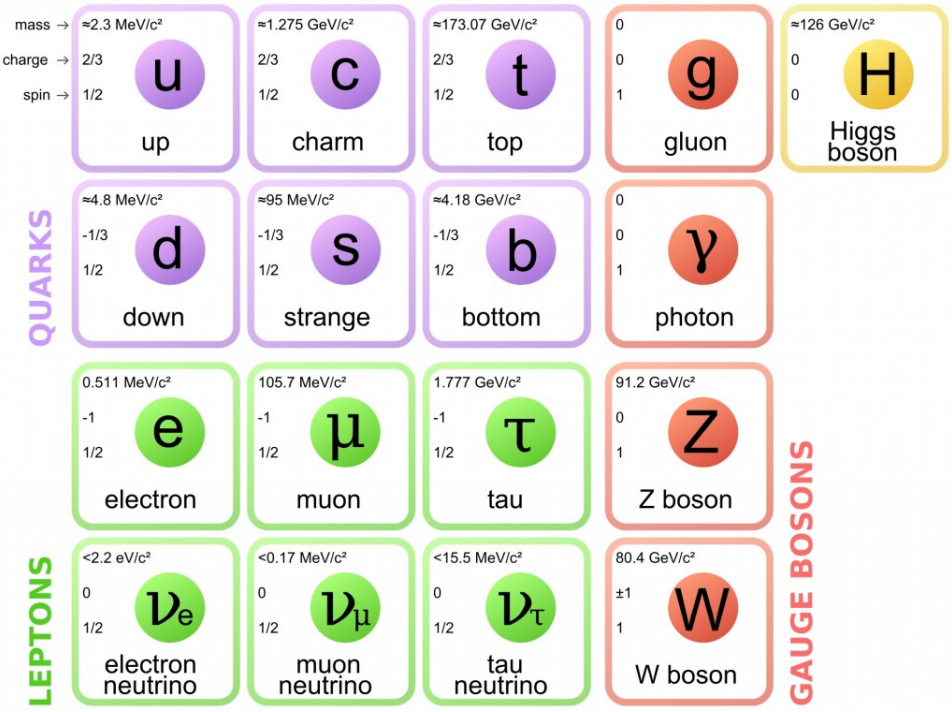

Figure 2.1: The Standard Model of Particle Physics [1].

The SM separates particles into two main groups: The *bosons* with an integer spin and the *fermions* with a half-integer spin.
The *Higgs boson*, with a spin of zero, is responsible for all fundamental particles acquiring mass, whereas the known *gauge bosons*, with a spin of one, are mediating the fundamental forces of electromagnetic (*photon*), weak (Z^0, $W^{\pm}$ *boson*) and strong (*gluon*) interactions.
The fermions can be separated into *quarks*, which are interacting electromagnetically and strongly, and *leptons*. The three leptons *electron*, *muon* and *tau* interact

electromagnetically and weakly, whereas their *neutrinos* only interact weakly. A further separation of the fermions is the one into three generations:
The first generation contains the *up* and *down quark* as well as the electron and the *electron neutrino*. Those particles make up all the known stable matter around us. The second generation contains the *charm* and *strange quark* and the muon and *muon neutrino*, while the third generation contains the heaviest quarks (*top* and *bottom quark*) and the heaviest lepton (tau) and its neutrino. The heavy particles of the second and third generation are rather short-lived and need high energies to be produced.

3. The Mu3e experiment

The *Mu3e* experiment is located at the Paul-Scherrer-Institut (PSI) in Villigen, Switzerland. Being a comparatively small particle physics experiment – in contrast to large-scale high energy experiments as found for example at the Large Hadron Collider (LHC) – the search for physics beyond the SM is conducted by high-precision measurements. Particularly, the aim of these measurements is to find the branching ratio (or an upper limit for it) of a muon decay into three electrons[1].

3.1. Theoretical background

A number of properties of interacting particles is conserved within the SM. One of them is the lepton number, describing the difference between the number of lepton particles and anti-particles. Following the SM, also the lepton flavor number, which is the lepton number for just one flavor of leptons (electron, muon, tau), should be conserved. However, since neutrino oscillations have been observed [2], evidence for the violation of the lepton flavor number conservation in the weak interaction of neutral particles has been found, calling for physics beyond the SM. Furthermore, the decay of a muon into three electrons (hence the name of the experiment *Mu3e*, which is searching for exactly this decay)

$$\mu^+ \to e^+ e^+ e^-$$

would violate the conservation of the lepton flavor number for charged particles. In contrast, the known decay channels (see [3]) of the positively charged muon

$$\begin{aligned}
\mu^+ &\to e^+ \, \nu_e \, \bar{\nu_\mu} \\
\mu^+ &\to e^+ \, \nu_e \, \bar{\nu_\mu} \, \gamma \\
\mu^+ &\to e^+ \, \nu_e \, \bar{\nu_\mu} \, e^+ \, e^-
\end{aligned}$$

conserve the lepton flavor number. It has to be mentioned, that nearly 100 % of the muon decays follow the first of the three modes mentioned above (Michel decay). The other two decay modes are restricted to certain energy limits and are rather rare with a decay probability of $\approx 6 \times 10^{-6}$ % (radiative decay with photon emission) and $\approx 3.4 \times 10^{-3}$ % (decay with inner conversion), respectively.
The decay $\mu \to eee$ is only possible including neutrino mixing (cf. Figure 3.1) within the SM, which is highly unlikely and suppressed by the order of $\mathcal{O}(10^{50})$ [4], making it practically negligible and unobservable. Therefore, the observation of such a decay would point to physics beyond the SM – in particular, the determination of the branching ratio could set limits to some theories, like for example some supersymmetry (SUSY) models that are predicting massive particles (c.f. [5], [6]).

The muon decay into three electrons is not the only process investigated in order

[1] Henceforth, the term *electron* in the context of a muon decay product implies the positrons as well.

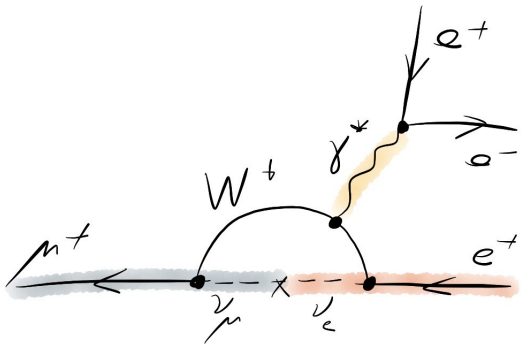

Figure 3.1: $\mu^+ \to e^+e^+e^-$ in a neutrino loop [4].

to find or discount (to a certain level of sensitivity) the lepton flavor violating decay. Experiments like MEG, located also at PSI and searching for the decay $\mu \to e\gamma$, or Mu2e at Fermilab, searching for the conversion of a captured muon into an electron, have the same aim as the Mu3e experiment.

3.2. The Mu3e detector

The aim of the Mu3e experiment in its final stage is to either find the lepton flavor violating decay $\mu \to eee$ or to set the limit of the branching ratio below 10^{-16} with a confidence level of 90 % [7].
The experiment makes use of the muon beam at PSI, which is currently the strongest in the world, yielding a rate of the order of 10^8 muons/s [7] created by a high-intensity proton beam fired on a fixed target. Since the expected rate of muons decaying into three electrons is really low, this high-rate muon beam is needed. The muons are extracted and directed to the detector setup, which is containing a target. The target consists of a Mylar foil which is double-cone shaped and aimed to stop the muons before the decay. A sketch of the detector is depicted in Figure 3.2. This setup is placed in a magnetic field such that the bending of the particle tracks allows for a precise momentum determination, and the bending direction can be used to discriminate electrons and positrons. As is sketched in Figure 3.2 the bending is in such a way that the electrons curl to the so called *recurl layers*. These layers are placed up- and downstream the beam pipe in an extent to cover the full range of the recurling electrons regarding their maximum energy of 53 MeV[2] and the strength of the magnetic field. The timing information is provided by scintillating fibers (time resolution of $\mathcal{O}(100\,\text{ps})$, [7]) placed around the target area and tiles (time resolution of $\approx 70\,\text{ps}$, [4]) placed within the cylindrical recurl layers. Close to the decay point on the target the four central pixel layers are located for the purpose of tracking and vertexing. The two inner layers have radii of about 2.3 cm and 3.0 cm and the two outer layers,

[2] Considerations of the conservation of energy and momentum allow for the calculation of the maximum kinetic energy of the electrons as the half of the muon rest mass.

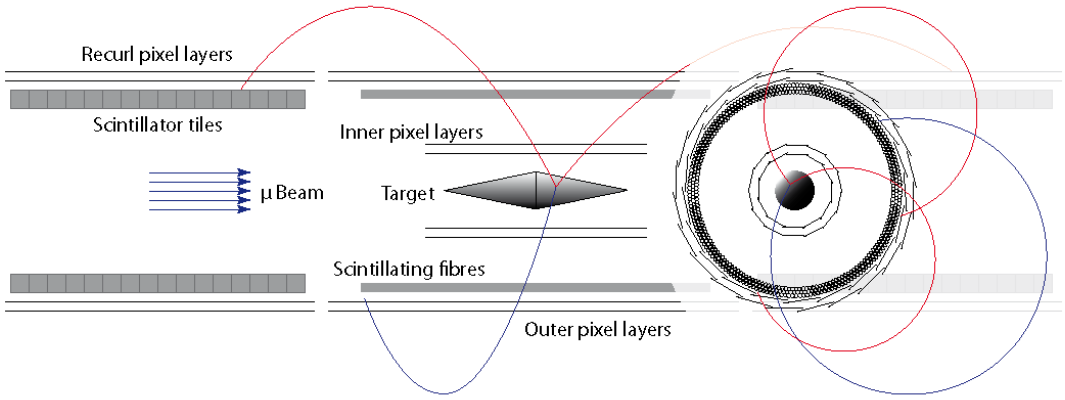

Figure 3.2: Setup of the Mu3e experiment [8].

outside the scintillating fibers, have radii of 7.4 cm and 8.6 cm, respectively [9]. The cooling of the detector, which is required due to the heat dissipation of the electronics, is achieved by gaseous helium.

3.3. Detector requirements

Several prerequisites have to be fulfilled in order to separate the rare, searched-for events from the background. One possible source of background is the decay $\mu \to eee\nu_\mu\nu_e$, which can be eliminated by precise energy measurements since kinetic energy is carried away by the neutrinos. This kind of background event, however, is intrinsic and can not be avoided by any means. To identify it as background the momenta of the electrons have to be determined precisely in order to get the energy of the particles. To reach the sensitivity for the branching ratio of 10^{-16} an energy resolution of 1.0 MeV is required [9].
Another source of background is the accidental background that can arise from coincidences of multiple single muon decays. Precise timing and vertexing allows for those events to be distinguished even at the high rates of 2×10^9 muons/s proposed for the final stage of Mu3e.
The momentum resolution is dominated by multiple Coulomb scattering (cf. Section 4.1.5). To reduce this scattering a low material budget and thus thin pixel sensors are required. To reduce the impact of multiple Coulomb scattering on the momentum resolution measurements even further the recurl layers are placed to detect the particles after bending about 180°. By this, the deflection by multiple scattering is eradicated in first order (for details see [7]). In fact, the multiple Coulomb scattering is the crucial point limiting the spatial resolution. The spatial resolution of the vertex detector has to be sufficiently good to distinguish different decays for the background elimination.

4. Silicon detectors

In this section the interaction of charged particles with matter will be addressed. Different processes can occur for particles traversing matter leading to energy losses (ionization, Bremsstrahlung) and deflections (Coulomb scattering) of the particle. In particular, the theory of energy deposition of electrons and positrons in silicon is introduced, allowing for a theoretical understanding of the working principle of semiconductor detectors. For a full understanding of the detectors the theory of semiconductor physics and p-n junctions is expedient as well and will be presented in the following.

4.1. Particle interaction with matter

In order to detect charged particles one has to make use of their energy loss while traversing matter. For this, various elaborate methods have been introduced, all based on the energy deposition due to one of the hereafter described processes. It is, however, important to distinguish between the energy loss of a particle and the energy that is deposited in the detector, as will be addressed in the further course.

4.1.1. Ionization and excitation

Charged particles experiencing the Coulomb field of the electrons in the matter they are traversing can transfer energy to these electrons. This energy transfer leads to excitation of the electrons and, if any, ionization. The energy loss of the traversing particle due to this process differs for heavy particles[3] and electrons and positrons.

Heavy particles

A heavy, charged particle traversing matter looses energy according to the Bethe-Bloch formula (adapted from [10])

$$-\left\langle \frac{dE}{dx} \right\rangle = K \frac{Z}{m_A} \rho \frac{z^2}{\beta^2} \left(\frac{1}{2} \ln \left(\frac{2 m_e c^2 \beta^2 \gamma^2 T_{max}}{I^2} \right) - \beta^2 - \frac{\delta(\beta\gamma)}{2} - \frac{C(\beta\gamma, I)}{Z} \right) \tag{4.1}$$

Here and in the following:

- $K \approx 50.97\,\mathrm{MeV\,fm^2}$ constant factor
- Z atomic number of the detector material
- m_A atomic mass of the detector material

[3] *Heavy* in this context means heavier than electrons.

- ρ density of the detector material
- z charge number of the traversing particle
- $\beta = \frac{v}{c}$ velocity of the traversing particle
- m_e electron mass
- $\gamma = \frac{1}{\sqrt{1-\beta^2}}$ Lorentz factor of the traversing particle
- T_{max} maximal possible energy deposition of a single particle
- I mean ionization energy of the detector material
- δ density-correction function (important for high energies)
- C shell-correction function (important for small velocities)

This formula holds for relativistic particles and describes the energy loss due to ionization and excitation of shell electrons in the traversing material. The proportionality to Z arises from the incoherent scattering on all electrons in the shell of the bulk material. For small values of the particle energy, this energy

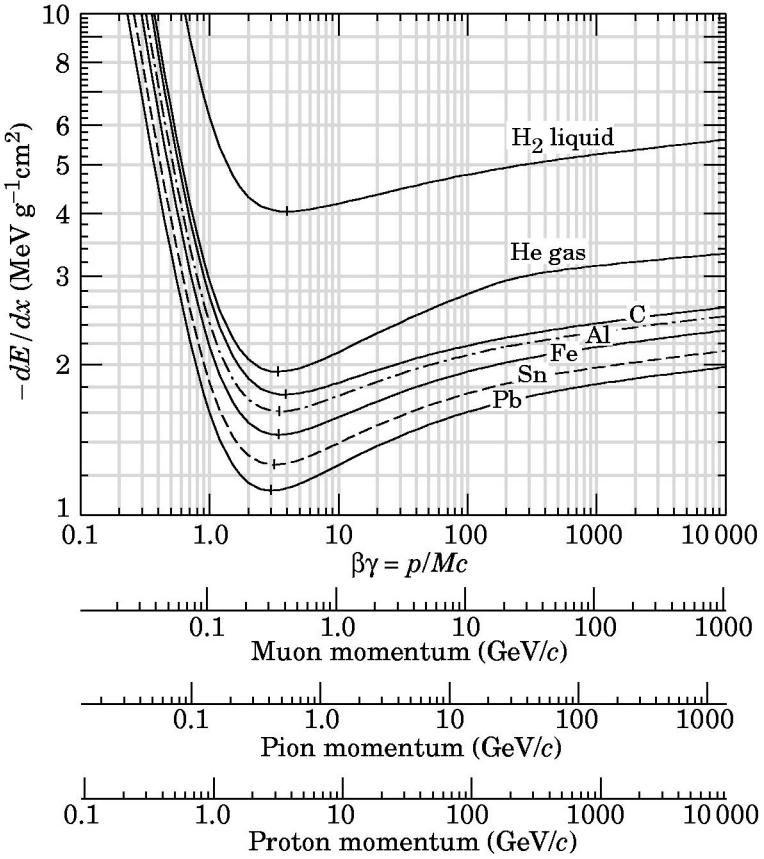

Figure 4.1: Density-normalized energy loss due to ionization in different materials [11].

loss increases with decreasing particle velocity proportional to $\frac{1}{\beta^2}$. This results from the increasing interaction time of the traversing particle with the matter for smaller velocities. In the region of $\beta\gamma \approx 3 - 3.5$ the energy loss has a minimum

for all heavy particles in all materials. The density-normalized energy loss in this minimum is around $\approx 2\,\mathrm{MeV\,g^{-1}\,cm^2}$, and particles in this region are called *minimum ionizing particles* (MIP). For higher particle energies the energy loss increases logarithmically due to the relativistic increase of the transverse electric field the traversing particles experiences. Finally the energy loss saturates and reaches a plateau (Fermi-plateau). The behavior of the energy loss in different materials is shown in Figure 4.1.
The mean ionization energy I is empirically and approximately given by (cf. [10])

$$I \approx 17.7 Z^{0.85}\,\mathrm{eV}\,. \tag{4.2}$$

Electrons and positrons

For electrons and positrons, energy loss due to ionization has to be described differently since the kinematics differ due to the much smaller mass. Additionally, in the case of electrons also differences arise due to the indistinguishability from the shell electrons. A detailed elucidation of the description of electron and positron energy loss due to ionization – from which the following formulae are taken – can be found in [12]. In the general case, the density-normalized energy loss in units of $\mathrm{MeV\,g^{-1}\,cm^2}$ is given as

$$-\frac{1}{\rho}\left\langle\frac{dE}{dx}\right\rangle = \frac{0.153536}{\beta^2}\frac{Z}{A}B(T) \tag{4.3}$$

with the atomic number A and the stopping number $B(T)$ depending on the kinetic energy T of the particle. For the case of electrons and positrons the stopping number differs from the one given in the Bethe-Bloch formula above an instead is

$$B(T) = B_0(T) - 2\ln\left(\frac{I}{mc^2}\right) - \delta \tag{4.4}$$

with different terms of $B_0(T)$ for electrons and positrons. With the substitution $\tau = \frac{T}{m_e c^2}$, for electrons this term is

$$B_0(T) = \ln\left(\tau^2(\tau+2)/2\right) + (1 + \tau^2/8 - (2\tau+1)\ln(2))/(\tau+1)^2 \tag{4.5}$$

and for positrons it is

$$\begin{aligned} B_0(T) = &\ln\left((\tau^2(\tau+2)/2)\right) + 2\ln(2) \\ &- (\beta^2/12)(23 + 14/(\tau+2) + 10/(\tau+2)^2 + 4/(\tau+2)^3)\,. \end{aligned} \tag{4.6}$$

With this model, and the energy-dependent density correction δ and the mean ionization energy I taken from [10], the energy loss shown in Figure 4.2 is obtained for the case of silicon. The density-correction in [10] is computed according to Sternheimer's parametrization (first introduced in [13]).

For particle energies beyond the minimum the electrons loose constantly more energy than the positrons, whereas the situation for small energies is inverse. Differences are caused by the indistinguishability of incident and scattered electrons, which is not given for positrons.
If the energy loss per collision is below the value of 0.255 MeV the process is

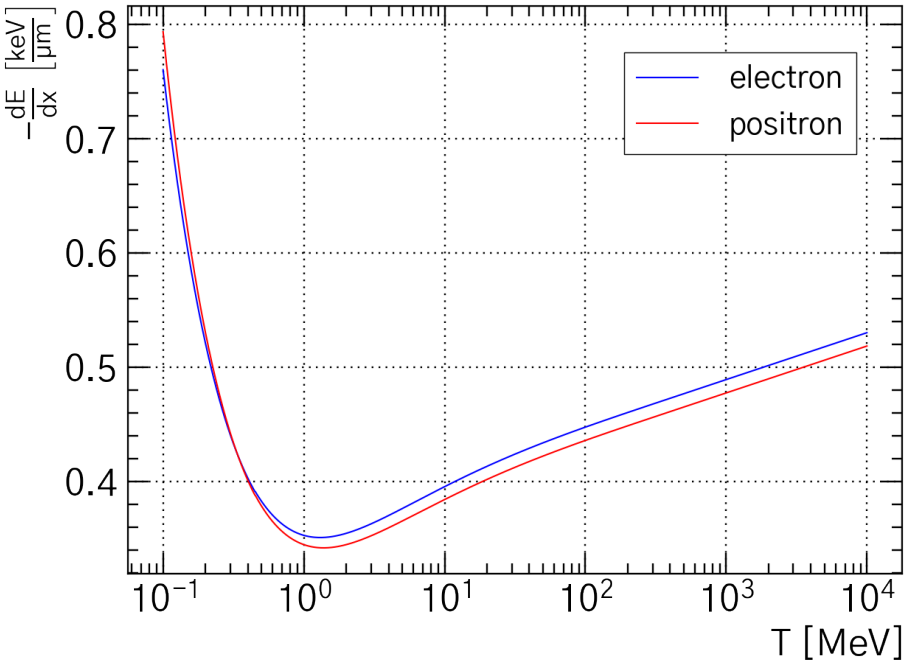

Figure 4.2: Energy loss of electrons and positrons in silicon due to ionization.

considered an ionization. For higher energies and therefore especially important for the creation of δ-electrons (see Section 4.1.2) the processes are called *Møller-* (e^-e^-) and *Bhabha-* (e^-e^+) scattering, respectively (cf. [14]).

4.1.2. δ-ELECTRONS

It is possible for electrons to absorb a big amount of energy from the traversing particle in central collisions. These so called δ-electrons have a sufficiently high kinetic energy to move away from the initial interaction point and perform further ionization along a secondary track. The number dN of such electrons which are produced in an energy range dT (with the kinetic energy T much larger than the ionization energy I) for a path length dx of the matter the particle is traversing is given in [14] as

$$\frac{d^2N}{dxdT} = \frac{1}{2}Kz^2\frac{Z}{A}\frac{1}{\beta^2}\frac{F(T)}{T^2} \tag{4.7}$$

with notations equally as for the Bethe-Bloch formula and a function $F(T)$ depending on the spin of the traversing particle. Formulas of $F(T)$ for spin-1/2 particles, like electrons and positrons, can be found in [15].

4.1.3. Energy loss fluctuations

The process for energy loss due to ionization only provides a formula for the mean energy loss. However, the actual energy loss of a particle traversing a material of thickness t underlies statistical fluctuations. These fluctuations are caused by two effects (cf. [16] and [17]). Firstly, the energy loss in a single collision of a particle with the electrons in the matter to be traversed is not constant, but the probability $p(\Delta)$ for an energy transfer Δ is given by the differential cross section $\frac{d\sigma(\Delta)}{d\Delta}$ divided by the total cross section $\sigma = \int_0^\infty \frac{d\sigma(\Delta)}{d\Delta}$

$$p(\Delta) = \frac{1}{\sigma}\frac{d\sigma(\Delta)}{d\Delta}\,. \tag{4.8}$$

With this, the probability of an energy loss Δ in N collisions becomes the N-fold convolution $F_N(\Delta)$ of $p(\Delta)$ with itself (adapted from [17]):

$$F_N(\Delta) = \int_0^\infty p(E)F_N(\Delta - E)dE \tag{4.9}$$

with

$$F_0(E) = \delta(E) \quad \text{and} \quad F_1(E) = p(E)\,. \tag{4.10}$$

Secondly, the overall number of collisions N – for a sufficiently thick sensor – follows a Poisson distribution $P_m(N)$ with the mean number of collisions m, depending on the sensor thickness t.
Altogether the probability $f(\Delta, t)$ for an energy loss Δ in a sensor of thickness t becomes the sum over N of the energy loss probabilities $F_N(\Delta)$ weighted with the Poisson distribution $P_m(N)$

$$f(\Delta, t) = \sum_{N=0}^{\infty} P_m(N)F_N(\Delta)\,. \tag{4.11}$$

The resulting distribution is called the *straggling function* and this method to obtain the straggling function in particular is called the *convolution method* (presented by Bichsel in [18]).
The determination of straggling functions using this method is, however, not trivial. The cross section differential in the energy loss has to be known and a large number of convolutions has to be computed, making the evaluation highly unwieldy.
A number of more convenient models has been developed and tested (see e.g. [18]) and a further discussion of some models of these straggling functions can be found in Section 10.
In general, the shape of these straggling functions is Gaussian-like for low energy losses and showing a strong asymmetry with a long tail towards high energy losses accounting for large energy transfers and δ-electrons.

4.1.4. Bremsstrahlung

For light particles, as electrons and positrons, the effect of Bremsstrahlung is dominant already at low energy. This effect is the loss of energy due to emission of radiation of a charged particle deflected in a Coulomb-field – mainly of atomic nuclei. The energy change dE of an incident particle per path length dx is given by

$$\frac{dE}{dx} = -\frac{E}{X_0} \tag{4.12}$$

with X_0 being the material-dependent radiation length (the mean length after which the initial energy has decreased by a factor of $\frac{1}{e}$). An empirical formula for this radiation length can be found in [19] (denotations are the same as in the Bethe-Bloch formula):

$$X_0 = \frac{716.408\,\mathrm{g\,cm^{-2}}A}{\rho Z(Z+1)\ln\frac{287}{\sqrt{Z}}}\,. \tag{4.13}$$

The energy of a particle lost due to Bremsstrahlung, however, is scarcely deposited in the detector with most of the emitted Bremsstrahlung photons leaving the sensor without substantial interactions.

4.1.5. Multiple Coulomb scattering

A charged particle traversing matter (e.g. a detector plane) will be scattered and deflected in the Coulomb-field of the nuclei and shell electrons. For fast particles the former are prime and for comparatively light particles, like electrons, the energy transfer to the nuclei is rather small, but the momentum can change significantly. Such scatterings occurring iteratively will lead to a distribution of the angles between the direction of the incident and final path. This distribution has approximately a Gaussian shape (the processes are described precisely in the Molière theory, cf. [20]).
The variance of the Gaussian distribution of the overall scattering angle θ is approximately given by

$$\sigma_\theta \approx \frac{21.2\,\mathrm{MeV}}{\sqrt{2}p\beta c}\sqrt{\frac{x}{X_0}} \tag{4.14}$$

with the momentum p of the particle and the velocity βc. The radiation length of the detector is X_0 and x denotes its thickness (cf. [10]).

4.2. Semiconductor physics

In order to fully understand the functionality of a pixel sensor it is important to understand the interaction between the sensor material and traversing particle. Since most pixel sensors are made of semiconducting materials, in this section the underlying physics of semiconductors will be discussed.
In a solid with lattice structure the wave functions of the single atoms overlap and

create continuous bands of energy levels. In the ground state these bands are filled beginning with the lowest energy level up to the so called *Fermi energy*, which, for semiconductors, is approximately the energy level at which the probability of an energy state to be occupied is 50 %. However, not all energies are allowed for electrons in such a system, there are certain "forbidden regions", so called *band gaps*. Such a band gap can occur between the highest lying fully occupied energy band (the *valence band*) and the next higher band (*conduction band*).

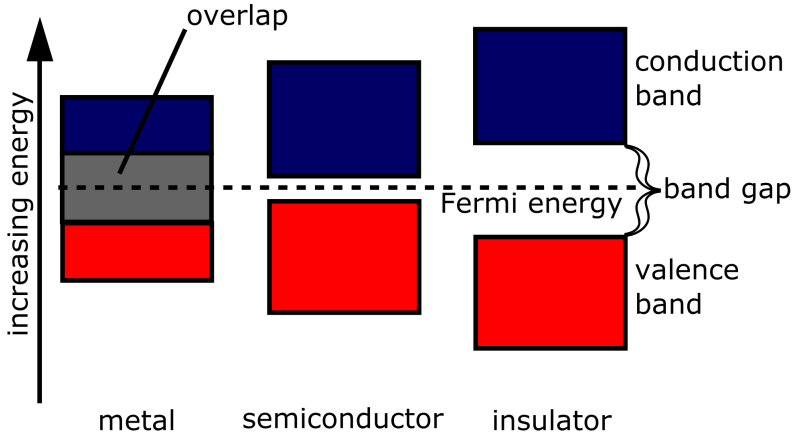

Figure 4.3: Electronic band structure model [21].

Based on the band structure of a solid material various properties can be explained qualitatively. For instance, the position of the Fermi energy has a direct influence on the charge transport in the material. Since fully occupied bands can not contribute to the charge transport, materials with the Fermi energy laying in the band gap are insulators. For metals the Fermi energy is located within an energy band, allowing electrons to move freely. A special case are semiconductors, here the band gap is small enough (e.g. 1.12 eV for silicon, [22]) that the thermal energy suffices to excite electrons into the conduction band, allowing them to contribute to charge transport. This makes semiconductors negative temperature coefficient thermistors, i.e. the resistivity increases with decreasing temperatures.

In a semiconductor the thermally excited electrons will leave a vacancy in the valance band . This vacancy ("*hole*") can be seen as a positive charge moving in the valence band similarly to the electron in the conduction band. The existence of electrons in the conduction and holes in the valence band is the basis for the conductivity of semiconductors. Since they occur jointly in the semiconductor, they are also called *electron-hole pairs*.

In a pure semiconductor the only charge carriers are the thermally excited electron-hole pairs. This kind of semiconductor is called *intrinsic*. The number of charge carriers can be obtained by using the density of states and the Fermi-Dirac statistics for electrons (for the calculations and the following results see e.g. [10]). The density of electrons in the conduction band is given by

$$n \approx 3.05 \times 10^{19}\,\mathrm{cm}^{-3} \cdot \exp\left(-\frac{E_C - E_F}{k_B T}\right) \tag{4.15}$$

and the density of holes in the valence band is

$$p \approx 2.55 \times 10^{19}\,\mathrm{cm}^{-3} \cdot \exp\left(-\frac{E_F - E_V}{k_B T}\right). \tag{4.16}$$

Here, E_F denotes the Fermi energy, k_B is the Boltzmann constant, E_C is the lowest energy level of the conduction band, E_V is the highest energy level of the valence band and T denotes the temperature.
Since electrons and holes appear jointly, the *mass action law* is applicable here, and (for intrinsic semiconductors)

$$n = p =: n_i \tag{4.17}$$

with the intrinsic charge carrier density n_i depending only on the temperature and the band gap of the semiconductor. For silicon at 300 K an intrinsic charge carrier density of $n_i \approx 1.01 \times 10^{10}\,\mathrm{cm}^{-1}$ is obtained.

4.2.1. Doping of semiconductors

For electronic applications the conductivity of intrinsic semiconductors is too low. In order to insert electron-hole pairs and hereby increase the conductivity of the silicon one can make use of the so called *doping*.
As described above, semiconductors have a lattice structure consisting of one or more types of different atoms. For the tetravalent silicon with four covalent bonds per atom, the lattice is of a face-centered cubic (*fcc*) structure. Replacing a small proportion of the silicon atoms (1 ppb - 1 ‰, [23]) with tri- or pentavalent atoms like aluminum or phosphorus yields a surplus of holes or electrons in the lattice increasing the conductivity by a factor of up to 10^6 (the material, however, is overall still neutral). The energy level of the additional electron of the *donor* (pentavalent atom) is close to the conduction band (the energy difference is of the order of 10^{-2} eV, [10]). This means that most of the donor electrons are thermally excited into the conduction band. Analogously the energy levels created by the *acceptors* (trivalent atoms) are just little above the valence band energy and electrons from the valence band can be easily thermally "excited" into these states.
Insetting trivalent atoms increases the number of holes in the lattice making them the majority charge carriers in this material, which is then called *p-doped*. Analogously for doping with pentavalent atoms the majority charge carriers are electrons and the material is called *n-doped*. The respective minority charge carriers are negligible for charge transport in the case of doped semiconductors, since their density is lower by a few orders of magnitude.
The doped semiconductors with impurities implanted on purpose are called *extrinsic* semiconductors.

4.2.2. p-n junctions

Boundary areas between p-doped and n-doped semiconductors are widely used in today's microelectronic world. At the same time, the p-n junction also forms the basis for the pixel sensors discussed in the scope of this thesis. Bringing an n- and a p-doped material into contact creates a *p-n junction* with certain properties, which will be discussed in the following.
As was described in the section before, the p-doped material has a surplus of holes whereas the n-doped bulk has a surplus of electrons. Bringing the materials in contact allows for electrons and holes to recombine in the boundary area. However, the initially electrically neutral p- and n-doped materials will create regions of space charge caused by the remaining donor and acceptor atoms after the electron-hole recombination. This means the acceptors of the p-doped material will attract electrons from the donors in the n-doped material leading to an effective negative charge on the side of the p-doped material and a positive charge with the n-doped part. This charge transport is called *diffusion*. The diffusion of the charge carriers and the resulting space charge of the remaining atomic cores is followed by the development of an electric field (*drift field*) in the boundary region counteracting the exchange of electrons and holes between acceptors and donors until eventually an equilibrium between the diffusion and the drift is reached (cf. Figure 4.4). This

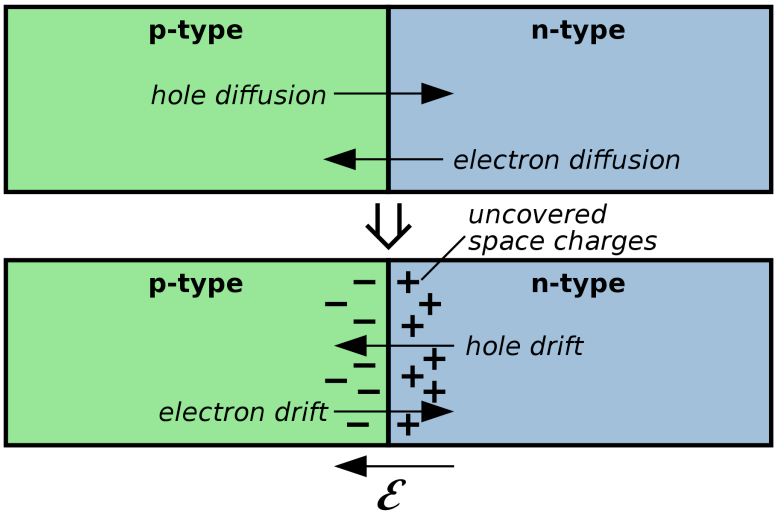

Figure 4.4: Charge carrier diffusion and drift at a p-n junction [24].

region, in which the electrons and holes recombined, is the so called *depletion region* where no free charge carriers are available anymore and therefore this part acts like an insulator. This region can be extended or reduced by applying an external voltage to the p-n junction.
Connecting the anode of a voltage supplier to the n-doped part and the p-doped material to the cathode (*reverse bias*) will increase the size of the depletion region by diverting the electrons and holes away from the junction and hereby making the junction non-conducting. Only a small leakage current will run through the p-n junction (diode) due to diffusion of the minority charge carriers until, at too high voltages, the diode breaks down and becomes conducting. Analogously, by

inverting the polarity of the voltage supplier (*forward bias*) the depletion region will decrease and the p-n junction becomes conducting even for low voltages.

5. Pixel detectors

To meet the requirement of high spatial resolution in the vertex detector the usage of pixel detectors is expedient. Pixel detectors in principle consist of a p-n junction as discussed above. A traversing particle will deposit energy and hereby create pairs of electrons and holes in the semiconductor material[4]. These charges can then be collected and used for signal generation.
Different construction principles for pixel sensors are available, which are mainly classifiable into the group of hybrid pixel sensors and monolithic sensors, both discussed in the following.

5.1. Hybrid pixel detectors

Hybrid pixel sensors were used most commonly in the last decades. They consist of two separate dies: One layer is for the readout electronics that each pixel has and one layer is the active p-n junction forming the detection volume in which the deposited energy is collected. A sketch of such a sensor type is depicted in Figure 5.1.

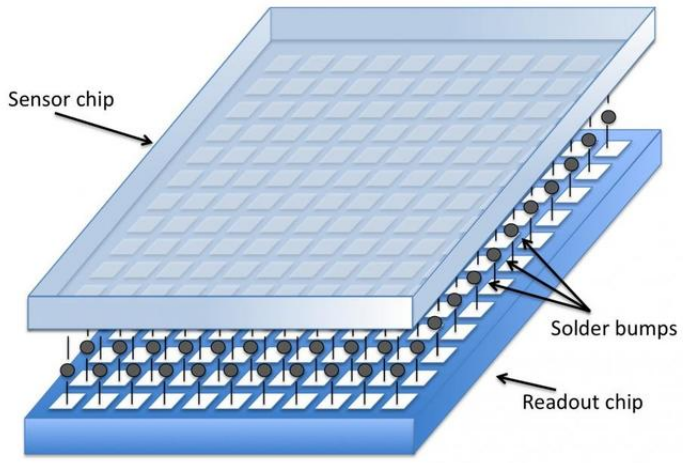

Figure 5.1: Sketch of a hybrid pixel sensor [25].

There are certain advantages for making this type of pixel sensor expedient for different applications. Due to the separate sensor and readout layer, the development for both can be done independently. More important, the application of

[4]For reasons of simplicity, they are termed just the *created* or *produced charge* in the following.

a high voltage as reverse bias to the active layer allows for full depletion of the sensor and a fast charge collection via drift resulting in a good time resolution and a high rate capability.
The bonding between the two layers, however, is rather expensive and the process is not trivial. Additionally, the material budget of the hybrid sensor is rather high increasing the probability and impact of multiple scattering.

5.2. Monolithic active pixel sensors

In contrast to the hybrid pixel sensors, the active part of a pixel and the readout electronics are realized on the same substrate for monolithic active pixel sensors (MAPS). A sketch of such a sensor can be found in Figure 5.2. These chips are

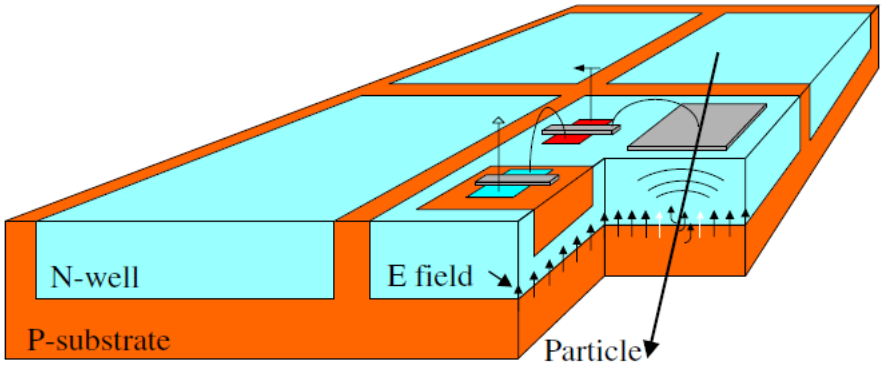

Figure 5.2: Sketch of a MAPS [26].

produced in commercial CMOS technology and therefore comparatively cheap. Due to the fact, that only one layer is needed, the MAPS can be produced rather thin reducing the effect of multiple scattering and hereby increasing the achievable spatial resolution for the tracking and vertexing.
Without the application of a high voltage or high doping, the created charge would be collected only by diffusion. This means a slow charge collection and also a small signal. There are two reasons for the small signal. Firstly, the charge will equally spread in all directions and only a small fraction will reach the collection electrode by chance. Secondly, charge may be lost due to recombination with impurities in the silicon. The probability for this effect increases with an increasing path a charge is traveling in the crystal and therefore is larger for diffusion than for drift. This drawback of the MAPS has been amended by the introduction of the high-voltage monolithic active pixel sensors (HV-MAPS). The HV-MAPS are MAPS, as discussed above, with the change that a high voltage is applicable to the sensor in order to deplete the active area and collect the charge via the drift in a strong field. This allows to thin down the sensors even more ($\mathcal{O}(50\,\mu\text{m})$), since the substrate is no longer needed for charge collection via diffusion – reducing multiple scattering even further.

Experimental setup

6. The MuPix10 chip

The development of the pixel sensors for the *Mu3e* experiment has lead frequently to the submission of new versions of sensors in the MuPix series. The latest version, the *MuPix10*, is designed to fulfill the requirements for the Mu3e experiment [9] and is the first full-size prototype for the final version. Its features and the operating principle are presented hereafter.

6.1. Features and geometry

The MuPix10 is an HV-MAPS consisting of 256×250 pixels of an $80 \times 80\,\mu m^2$ size. Each pixel has a digital partner cell in the periphery adding up to a total size of $20.66 \times 23.18\,mm^2$. The chip is produced in an 180 nm HV-CMOS process by TSI semiconductors. Sensors were produced on wafers with resistivities of 20 and $200\,\Omega\,cm$ (cf. [27]). The MuPix10 pixel matrix is shown in Figure 6.1. The pixel matrix is divided in three sub-matrices of 84/86/86 columns, which are read out separately. The periphery part on the lower end of the chip along the columns contains the HV and power pads, the readout control unit (RCU), the pixel configurations and temperature diodes.

6.2. Signal processing and readout

The electrons produced in the sensor material by an ionizing particle (cf. Section 4) are drifting to the collection electrode. The signal created by the collected charge is AC-coupled to the charge-sensitive amplifier (CSA). The CSA is implemented in the pixel and has a negative feedback circuit. These components are used to shape and amplify the signal.
Alternatively, the signal can be mimicked by a test-pulse injection by discharging a capacitance in the pixel.
A line driver sends the signal to the periphery. The periphery structure presented in the following is provided for each pixel on the sensor.
The signal is compared to a threshold by a comparator. The threshold is set globally but can be tuned for each pixel by so called Tuning Digital-to-Analog

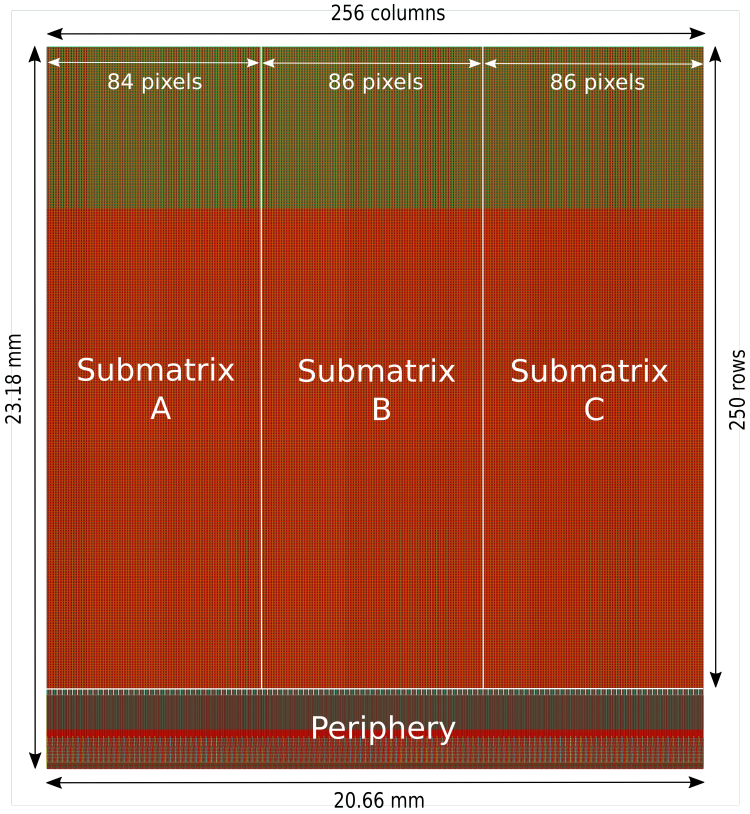

Figure 6.1: MuPix10 pixel matrix [28].

Converters (TDAC, for detailed information see [29]). Arriving at the comparator the analog signal is then digitized: A comparator output is obtained if the threshold is exceeded. By this digitization information of the analog signal shape is lost and the signal information is condensed to two timestamps (TS): The time of the first (TS1, leading edge) and the last (TS2, falling edge) exceeding of the threshold. The difference of the two timestamps yields the time-over-threshold (ToT).
A problem occurring in this readout procedure is the delay between the actual time of arrival of the hit and the time of detection of this hit, which is the TS1. This delay is called *time walk* and is caused by the finite rise time of the leading edge. Detailed studies of this effect have been carried out in [30] and corrections can be performed if the ToT of the signal is known.
A special feature of the MuPix10 chip is the possibility to use it in the so called 2-*threshold mode*. This means, the threshold for the timing information and hit detection can be set independently resulting in a better timing information of the hit. To achieve this, the first threshold (threshold for the timing information) is set comparatively low (only little above the noise level) to get the first time information (TS1) with as little time walk as possible. The second threshold (threshold for the hit detection) is used to determine the TS2. It can be set to a higher value in order to filter out the real hits from noise hits potentially provoked by the low first threshold.

Finally, the digitized signal is transmitted to the state machine, which is part of

the RCU in each sub-matrix. Here the data is $8b/10b$ encoded, serialized and sent out at a rate of 1.25 Gbits/s [31]. The readout scheme is outlined in Figure 6.2.

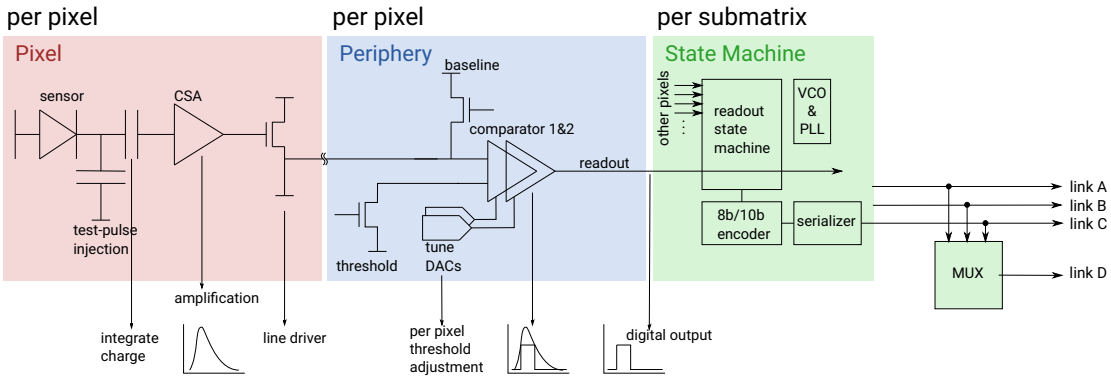

Figure 6.2: Readout scheme of the MuPix10 chip [32].

6.3. Sensor testing structures

For testing purposes, the chip is bonded to an insertable printed circuit board, short *insert*. An insert allows for application of the chip in the lab or at testbeam facilities. It can be used to supply the voltages provided by a motherboard (see below) to the chip. Furthermore, it is an interstation for the hit signal transmission from the sensor and provides test-points for the measurement of applied voltages [29]. A picture of a MuPix10 bonded to an insert can be found in Figure 6.3. The insert is applied to a motherboard providing the HV, necessary signals (e.g.

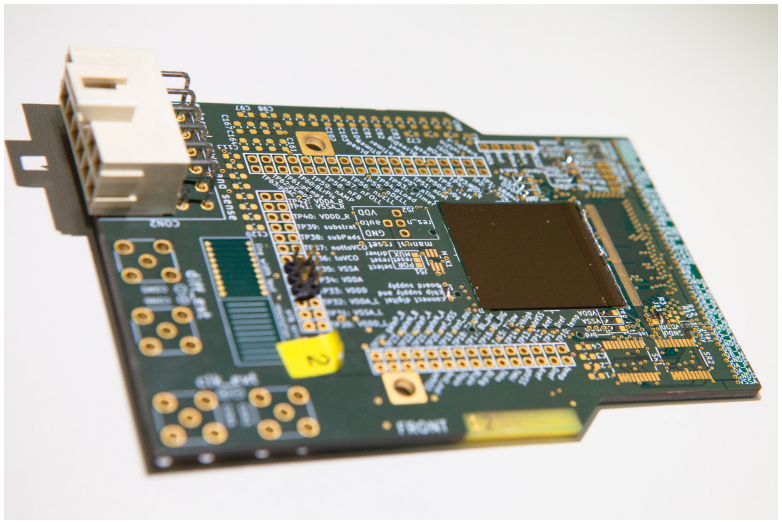

Figure 6.3: MuPix10 on an insert [28].

clocks) and the data links to the Field-Programmable Gate Array (FPGA). In turn, the FPGA provides the configurations for the sensor and receives the data to forward it to a computer for further processing and analysis. The data processing

on the FPGA and analysis on the computer is called *Data Acquisition* (DAQ). Data Acquisition Systems have been developed for different experimental setups of sensors: The DAQ can be performed for single sensor setups as well as for a setup of multiple sensors for testing purposes (*telescope*, cf. Section 7.1). A detailed description of the telescope DAQ System can be found in [33].

7. Testbeam

The characterization of the pixel sensors is crucial in order to find the best configurations and to understand the behavior of the chip for the use in the final experiment. The aim is to study the performance of the sensor, e.g. regarding the efficiency or time resolution, and improve it, subsequently. For this, dedicated testbeam campaigns are performed in which pixel sensors can be characterized using a particle tracking telescope, which is presented in the following.

7.1. Telescope setup

The telescope consists (in this case) of three reference layers and the device under test (DUT) in between, complemented by scintillating tile detectors up- and downstream the telescope. The latter are used as a timing reference. A sketch of the telescope setup can be found in Figure 7.1.

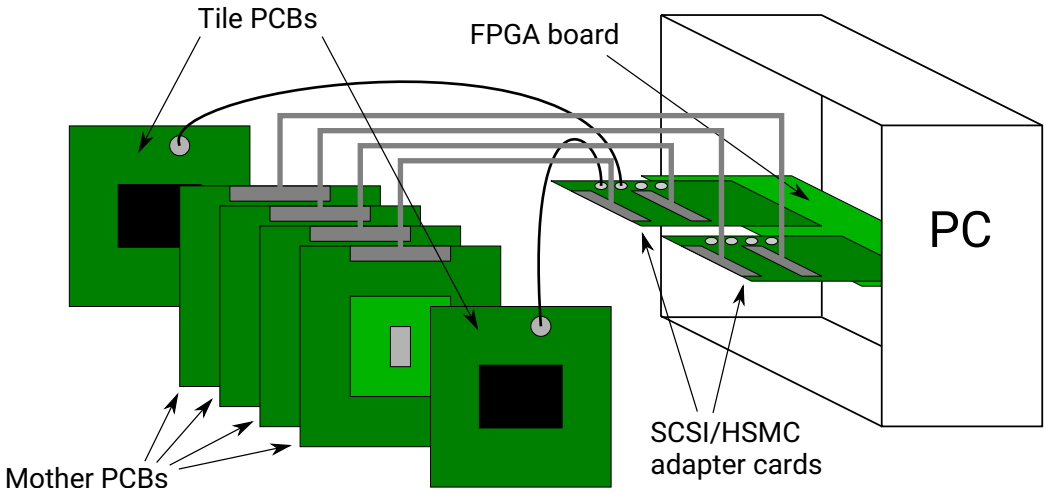

Figure 7.1: Telescope setup [34].

7.2. Particle tracking in a telescope

The telescope is subjected to a testbeam (beam of ionizing particles, e.g. electrons). In consequence of the use of such a multi-layer setup, the determination of the track of particles traversing the telescope is possible, as explained in the following:
A particle traversing the telescope induces hits at certain positions on the reference layers[5]. Knowing the exact positions of all layers a particle track from

[5]The reference layers can be of the same sensor type as the DUT.

the hits on the reference layers can be reconstructed and interpolated onto the DUT, which is excluded from the track reconstruction. On the DUT, hits within a certain time window and a certain spatial distance to the interpolated track intersection with the DUT are searched and, as the case may be, assigned to the track.
In order for the tracking to work properly, the telescope needs to be aligned and exact positions of the reference layers and the DUT need to be known. The telescope alignment is explained in more detail in the next part.
A detailed elucidation of the tracking procedure for the telescope setup can be found in [33].

7.3. Telescope alignment

As was mentioned in the previous part, a precise knowledge of all layer positions, and also rotations, is required. The lower left pixel of the first sensor layer along the beam direction marks the zero point of the global system of coordinates. Each layer position and rotation is then fully characterized by the position of the lower left pixel with regard to the global system of coordinates and three Euler angels (for an exact specification see [33]). All these quantities are saved to a file, which is then used by the analysis to take into account the shifts and rotations of the layers for further calculations.
The first estimation for the values are the positions measured by hand, and the rotations are assumed to be zero.

After data taking with the telescope is finished the correlations between the

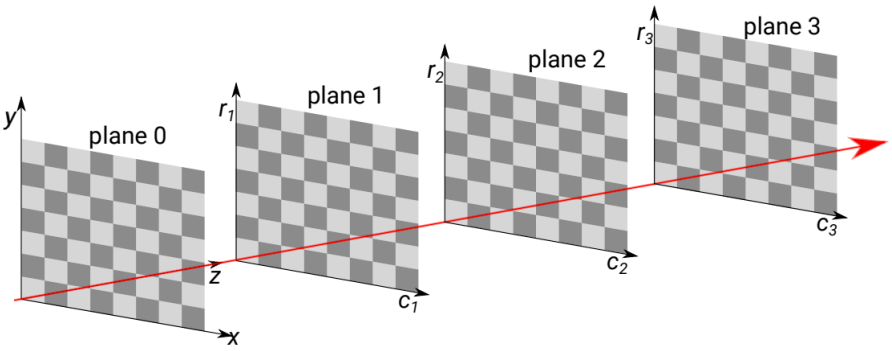

Figure 7.2: Track through telescope layers [33].

hits on the layers are used to do a coarse alignment of the layers along x- and y-direction (coordinates as in Figure 7.2). For all hits on one layer the residuals[6] to all hits on the fist layer are computed. For a perfectly aligned telescope the residuals show a peak (mean) at zero, and a misalignment would shift this peak allowing for an according correction in order to center the peak around zero.
A fine alignment is done by performing the tracking as described in Section 7.1. For the translational alignment the residuals between all the track intersection

[6]The residual is the hit position along on axis (x or y) of a hit on one layer minus the respective hit position of a hit on a second layer.

positions along on axis and the hit positions of the hits that are assigned to this track are calculated. Again, the shift of the peak indicates a misalignment, which is then corrected for. Exemplarily, a histogram containing the column residuals with a Gauss fit to determine the peak position is shown in Figure 7.3.

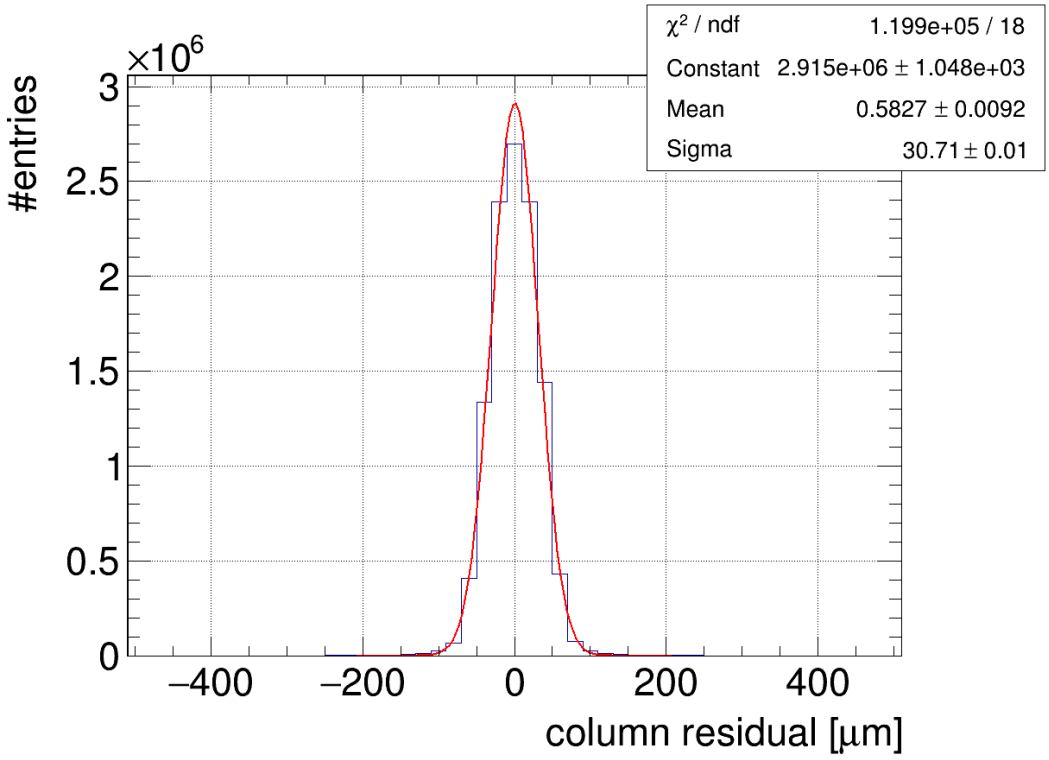

Figure 7.3: Example for the column residual distribution used for the translational alignment.

Additionally, the rotation of all layers can be determined. For this, the relation between the mean residuals along on axis and the row or column address[7] is taken into account. Rotations of a layer correspond to a – in first order linear – dependence of the mean residuals on the column or row address and can be corrected for by fitting of a linear function and consideration of the slope. An exemplary plot for this is shown in Figure 7.4. With this procedure the alignment of the layers better than 1.5 µm (translational) and 0.05 µm/pixel (rotational) is achievable in general.
For a few measurement runs, however, the positions of the layers changed considerably over time. Since the alignment was only done for the first run after a mechanical adjustment of the telescope, and is supposed not to change for the following runs of a measurement, this resulted in an increasing misalignment of the telescope represented by an increase of the mean residuals between track intersections and hit positions. An example of this effect is shown in Figure 7.5 for the mean residuals along the y-direction. This problem has been avoided by fitting

[7] Possible plots are x-residuals against row, x-residuals against column, y-residuals against row and y-residual against column.

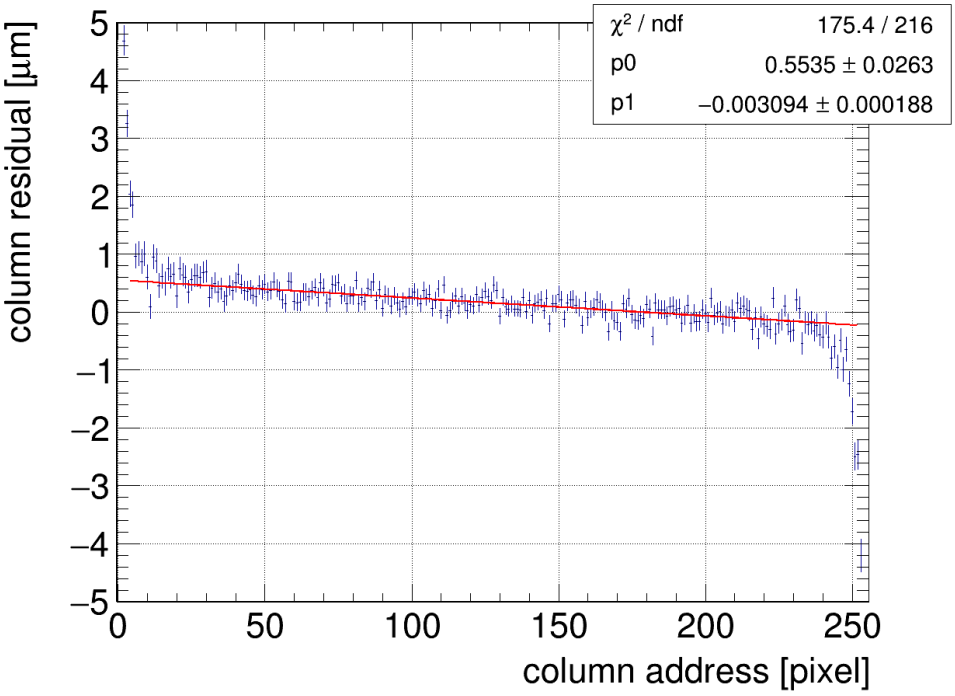

Figure 7.4: Example for the mean column residual dependence on the column address.

an appropriate function to the mean residual curves for each layer, and correcting for this residual for each run and layer in the data analysis. Subsequently, the according alignment plots have been checked to confirm that the correction works properly.
The cause for this issue is likely to be the mechanics of the telescope. A possible explanation is that the springs that are used to adjust the positions of the planes are expanding not immediately but over time leaving a scope for the planes to move.
The alignment of the telescope for the runs which are used for the analysis in this thesis can be confirmed by Figure 7.6 and Figure 7.7. In Figure 7.6 the mean residuals in x- and y-direction are added quadratically for the measurement runs 620 to 2486, and as can be seen, they are kept below 1.5 µm. For Figure 7.7 the four different combinations for the residual vs. row/column plots are considered and the largest slope of the linear fit in these plots is set as the rotational misalignment. This misalignment is consistently below 0.05 µm/pixel, which corresponds to a rotation of roughly 0.7 mrad.

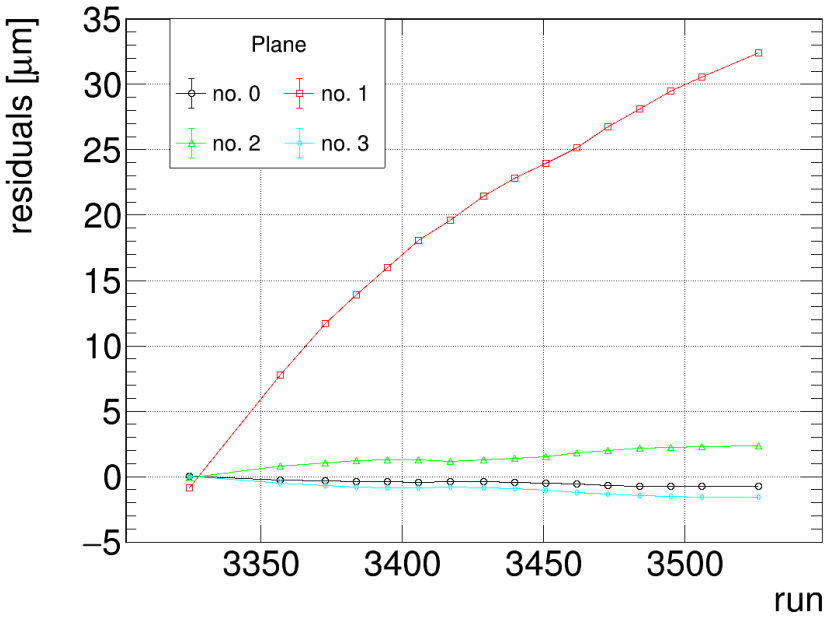

Figure 7.5: Telescope misalignment increasing over time.

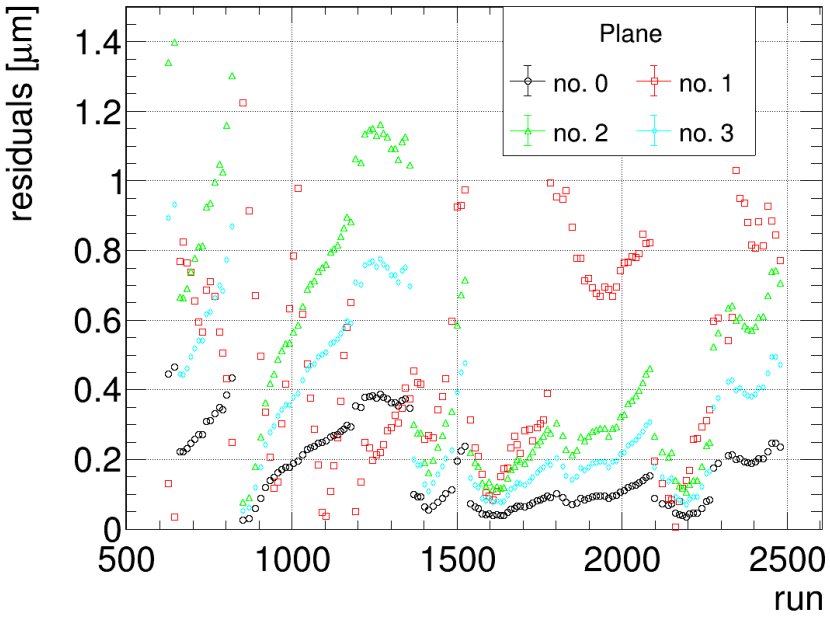

Figure 7.6: Translational alignment of the telescope for run 620 to run 2486.

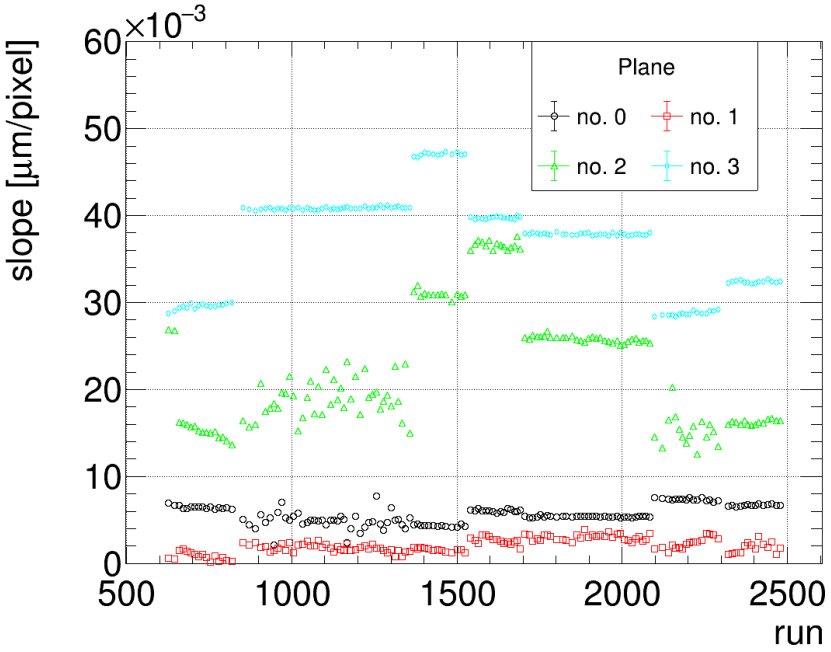

Figure 7.7: Rotational alignment of the telescope for run 620 to run 2486.

Analysis and Models

8. Sensor characterization

The raw data from the MuPix10 sensor provides only the hit information: The two timestamps (TS1 and TS2) for first and last exceeding of the threshold and the hit position (column and row address). Starting from these data obtained with a telescope on a testbeam campaign various properties – presented in the following – can be extracted in order to characterize a chip and draw further conclusions from the analysis.

8.1. Hit detection efficiency

The efficiency of a sensor can be determined from telescope data. The reference layers are used to determine particle tracks through the telescope. The track intersections with the DUT are calculated and hits on the DUT are searched within a certain time window and a certain distance. Finally, the efficiency ϵ is calculated as the number of tracks for which an hit on the DUT has been matched divided by the number of all tracks:

$$\epsilon = \frac{\#\text{tracks with associated hit on DUT}}{\#\text{all tracks}} . \tag{8.1}$$

Various factors can impact the efficiency:

- The threshold and high voltage (HV) which are applied to the sensor are the defining properties for the efficiency (cf. Section 10).
- Multiple Coulomb scattering can reduce the calculated efficiency, if a particle is deflected in a way that a track can be reconstructed from the reference layers but the hit on the DUT is out of the searching window. This effect is expected to be secondary.
- Coincident noise hits on the reference layers can mimic a track without a hit on the DUT adding to the obtained inefficiency. This can especially occur from crosstalk (see next section) as explained in the following:

A real particle track is causing hits on the reference layers. Due to the effect of crosstalk, these real hits can mimic noise hits somewhere else on the sensor (but for each sensor on the same position), which are in turn mimicking a track parallel to the real track. If the crosstalk probability is p_x, the probability p for this effect to contribute to the inefficiency is[8]

$$p = p_x^3 \cdot (1 - p_x)\,. \tag{8.2}$$

This could be avoided by rotating one of the reference layers with respect to the others ([35]).

8.2. Noise hits

A noise hit is a hit on the DUT which can not be assigned to any track through the telescope. Not only electronic noise can give rise to such a hit. Also the above mentioned effect of multiple Coulomb scattering can cause hits to be counted as noise. Inefficiencies of the reference layers can cause noise hits as well since a track is only reconstructed if an assignable hit on all reference layers is detected. For an inefficiency ι for one reference layer the probability q for a noise hit due to reference layer inefficiencies is

$$q = \iota(\iota^2 - 3\iota + 3)\epsilon_{DUT}\,. \tag{8.3}$$

A short derivation for this can be found in Appendix A.

A significant part of the noise is caused by the so called crosstalk. Crosstalk is the effect of capacitive coupling of neighboring signal transmission lines on the sensor. This allows real signals to induce fake signals in the readout part for pixels in which no charge deposition took place. The pixel positions in which the crosstalk hits can be induced are determined by the routing scheme of the transmission lines of the sensor. A detailed and theoretical introduction to crosstalk and a study for a MuPix8 have been performed in [33] and [36].

8.3. Time over Threshold spectrum

The ToT spectrum is a histogram obtained from the ToTs (differences between TS1 and TS2) of all the hits on the sensor. An example of such a spectrum is depicted in Figure 8.1. The spectrum consists of three main regions. It has a peak at low ToT values which is mostly caused by noise and crosstalk. This peak gets smaller for higher thresholds as more and more noise hits can not exceed the higher thresholds. The peak largely vanishes for the ToT spectrum of only the matched hits – also confirming the matching algorithm to work properly.
The middle part of the spectrum is the part representing the fluctuations of the

[8] for a telescope with four layers of same type

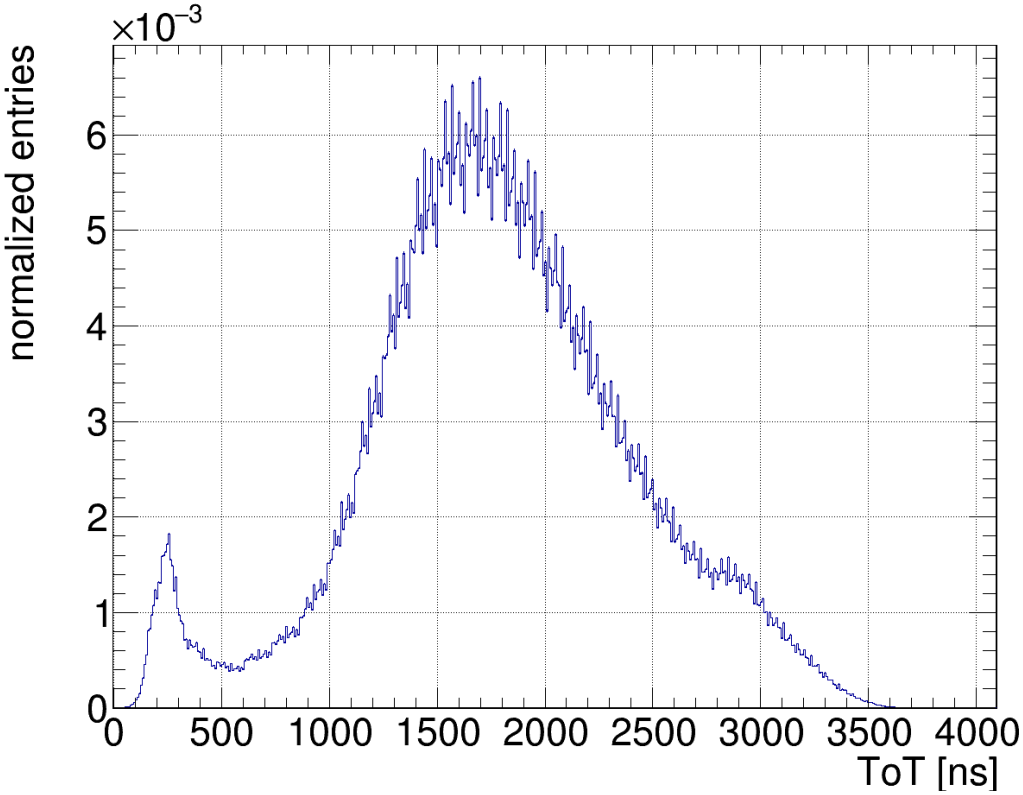

Figure 8.1: Example plot of a ToT spectrum of the MuPix10 chip.

energy deposition (cf. Section 4) and is therefore basically following a Landau-like distribution (see also Section 10). Pixel to pixel variations, variations in the readout and the particle energy, smear out this distribution, and for the fitting of this part a Landau function convoluted with a Gauss is expedient. The impact of the application of a threshold is as following: Not all signals will make the exceeding of the threshold meaning smaller signals – according to small charge deposition in the Landau distribution – will not be detected. This basically cuts away a certain part of the initial Landau spectrum with the cut not sharp but being smeared out with a Gaussian-like shape.
In the last part of the ToT spectrum the effect of the ToT cut becomes visible. In order to simplify the sorting of the data a limit for the signal duration is set. The cut is set to roughly 3000 ns. Hits signals with a larger ToT will be pulled down to a ToT in the range of the ToT cut, which underlies variations caused by the method which is used to cap the ToT. This leads to a small peak at around the value of the ToT cut. Detailed studies of the ToT cap can be found in [30].

8.4. Hit cluster size

A cluster is formed by adjacent hits on a pixel sensor. Cluster can be caused by charge sharing of two pixels meaning the charge of a traversing ionizing particle

spreads over more than one pixel.
Clustering can be performed for a pixel detector in order to improve the spatial resolution. With only the raw hit information the spatial resolution $\sigma_{x/y}$ is given by (see Appendix B)

$$\sigma_{x/y} = \frac{\text{pixel width in x/y}}{\sqrt{12}} \,. \tag{8.4}$$

This resolution can be improved by taking into account the cluster information since the probability of charge sharing and therefore cluster formation is increasing towards the edges of the pixel.

9. Charge diffusion in a silicon pixel detector

As extensively discussed in Section 4, an ionizing particle traversing the detector causes pairs of electrons and holes. The electrons are are collected and induce a signal. The directed movement of the electrons in an electric field is however superimposed by random thermal diffusion. A model for this movement and its effect on the cluster formation is presented in the following.

9.1. Model for charge diffusion

For the development of the sensors of the MuPix series it has been assumed that the charge collection via diffusion is negligible. Results from the testbeam at DESY in April 2021, however, suggested that charge collection via diffusion could be relevant for the signal generation (see also Section 12). It is therefore of interest to have a rough model for the charge diffusion in the sensor in order to asses its importance.
The starting point for the calculation of the charge spread over the time t is given by *Fick's law* [37]:

$$\frac{dQ}{dx}(\vec{x},t) = \frac{1}{8(\pi Dt)^{3/2}} \int Q_0(\vec{x}') e^{-\frac{(\vec{x}-\vec{x}')^2}{4Dt}} d\vec{x}' \tag{9.1}$$

with the diffusion constant D and the initial charge distribution $Q_0(\vec{x}')$. For a point charge this yields a Gaussian distribution with a spread of

$$\sigma = \sqrt{2Dt}\,. \tag{9.2}$$

This relation can be used as an estimation for the mean squared deviation (MSD) of a charge from its point of creation.
The diffusion constant D can be calculated using the *Einstein relation* [38]:

$$D = \mu_e \frac{k_B T}{q} \tag{9.3}$$

with the electron mobility μ_e, the temperature T and the electron charge q.
The electron mobility in silicon is only weakly depending on the resistivity (variation below 2 % in the range of 100 Ω cm to 1000 Ω cm, cf. [39]) but has a strong temperature dependence (cf. [10]). Taking into account these uncertainties the mobility is estimated to a value of $(1470 \pm 100)\,\mathrm{cm^2\,V^{-1}\,s^{-1}}$. For a temperature of (300 ± 10) K the diffusion constant can be computed to

$$D = (38.0 \pm 2.9)\,\mathrm{cm^2\,s^{-1}}\,.$$

9.1.1. Diffusion without electric field

The relevant time $t_{diffusion}$ to calculate the drift of a particle without electric field according to Equation 9.2 is the time from the beginning of the signal until the peak of the signal is reached[9], which can be estimated from fitting the amplifier output signal. Measurements of this signal shape have been performed in the scope of another thesis [40]. By using the results one can obtain the signal amplitude after a time of (410 ± 70) ns. The error is caused by the dependence of the signal shape on the amount of deposited charge.
Using this time, the Gaussian spread of an electron due to diffusion without an external field is calculated to be

$$\sigma = (56 \pm 8)\,\mu\text{m}\,.$$

This rough estimation can be used as a reference for the range which a charge can possibly travel outside the depleted region of the sensor and still contribute to the signal amplitude.

9.1.2. Diffusion with electric field

The diffusive spread of an electron once it has reached the drift field is much lower than the spread without a field since the diffusion times for the two cases differ. For an electron in the drift field the diffusion time is given by the drift time, whereas the time of diffusion for an electron outside the drift field is given by the time presented in Section 9.1.1 (the time in which an electron created outside the depletion zone can diffuse to the drift field and still contribute to the signal height). The latter is larger by roughly three order of magnitudes compared to the drift time, as is presented in the following. This causes the diffusive spread for electrons during the drift towards the electrodes to be much smaller.
In order to calculate the diffusive spread of a charge in the drift field the drift time t_{drift} has to be calculated and applied to Equation 9.2.
The drift velocity v_{drift} of an electron in an electric field E is given as

$$v_{drift} = \mu E\,. \tag{9.4}$$

The electric field in a diode is not constant, but it is (in first order approximation) rising linearly towards the junction. For the following calculations the drift velocity v_{drift} denotes the mean value, which is obtained by Equation 9.4 and the mean electric field

$$\overline{E} \approx \frac{1}{2}\frac{U}{x_{dep}} \tag{9.5}$$

with the width x_{dep} of the depletion zone and the high voltage U. For an electron traveling through the entire depletion zone width x_{dep} towards the collection

[9] Within this time, collected charge contributes to the signal amplitude.

electrode the drift time t_{drift} becomes (using Equation 9.2 and Equation 9.4)

$$t_{drift} = \frac{x_{dep}}{v_{drift}} = \frac{2x_{dep}^2}{\mu_e U} \,. \tag{9.6}$$

The depletion zone width x_{dep} is modeled, as described in [10], by

$$x_{dep} \approx 3.6 \times 10^3 \sqrt{\frac{U q \mu_h \rho}{\mathrm{V\,cm}}} \tag{9.7}$$

with the resistivity ρ of the sensor substrate and the hole mobility μ_h. For this equation, it is used that the resistivity in a p-doped material with doping concentration n_p is given by [41]:

$$\rho \approx \frac{1}{n_p \mu_h q} \,. \tag{9.8}$$

The contribution of the minority charge carriers to the conductivity is neglected in this equation.
With the depletion zone depth in Equation 9.7 the drift time in Equation 9.6 becomes

$$t_{drift} = 2.592 \times 10^7\,\mathrm{V^{-1}\,cm^{-1}} q \rho \frac{\mu_h}{\mu_e} \,. \tag{9.9}$$

This means, for the model created above, the electron drift time is only depending on the substrate resistivity and the electron and hole mobilities and therefore constant for different high voltages.
For the hole mobility, a value of $\mu_h = (470 \pm 20)\,\mathrm{cm^2\,V^{-1}\,s^{-1}}$ is assumed (cf. [39]). The MuPix10 sensors which are characterized within the scope of this thesis are made of $200\,\Omega\,\mathrm{cm}$ wafers, what actually means that the resistivity lies between $200\,\Omega\,\mathrm{cm}$ and $400\,\Omega\,\mathrm{cm}$ [35] with the real value unknown. It is therefore expedient to set the bounds of the models further discussed by using the upper and lower limit of the resistivity. With this, the drift time and charge spread can be calculated, and the values are listed in Table 9.1.

	$200\,\Omega\,\mathrm{cm}$	$400\,\Omega\,\mathrm{cm}$
drift time	$(0.266 \pm 0.021)\,\mathrm{ns}$	$(0.53 \pm 0.04)\,\mathrm{ns}$
charge spread	$(1.42 \pm 0.11)\,\mu\mathrm{m}$	$(2.01 \pm 0.16)\,\mu\mathrm{m}$

Table 9.1: Limits for drift time and charge spread.

9.2. Cluster size model

The average cluster size can be computed under the assumption of a certain spread of a particle in the drift field of the high voltage by using a geometrical reasoning. Depending on the region in which the charge is deposited it can spread to one, two or three adjacent pixels within the model presented in the following. Given a spread s, and with the pixel width $d = 80\,\mu\mathrm{m}$ the expected cluster size can be calculated by adding the, weighted with the cluster multiplicity, areas of the

different regions and dividing the result by the pixel pitch. A sketch illustrating the different areas can be found in Figure 9.1. The different colored areas depict

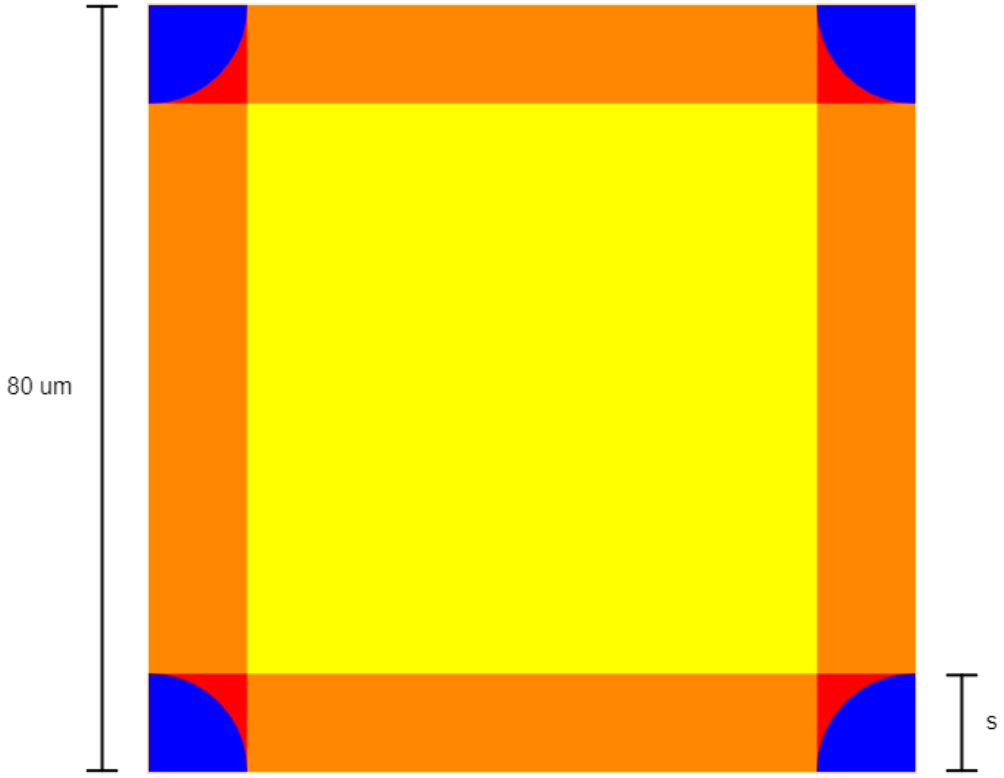

Figure 9.1: Sketch of a pixel of the MuPix10 sensor (not to scale). Yellow: cluster size one, orange: cluster size two, red: cluster size three, blue: cluster size four.

the regions in which a traversing particle can create clusters of different sizes. For instance, a particle traversing the orange area potentially induces a cluster of size two, if the charge is horizontally spreading a distance of s.
Following this argumentation, it is geometrically obtained

$$\text{cluster size} = \frac{1}{d^2}\left((d-2s)^2 + 8(d-2s)s + 12s^2\left(1-\frac{\pi}{4}\right) + 4\pi s^2\right) . \tag{9.10}$$

If charge is collected solely by drift, the charge is diffusing only for the drift time t_d. For the spread s in Equation 9.10 this means the values in Table 9.1 can be used for the calculations. Thus, using the upper and lower limits for the resistivity of the MuPix10 sensor (cf. Section 9.1.2), limits for the cluster size can be set by this model, which are shown in Table 9.2. For this calculation, the uncertainty on the pixel pitch can be neglected.

Certain assumptions are made in this model, which are described in the following. The model only works for a sensor at zero threshold since, within this model, even a single charge diffusing into an adjacent pixel is expected to create a cluster. This, of course, is only the case for a threshold level of zero and perfectly

	$200\,\Omega\,\mathrm{cm}$	$400\,\Omega\,\mathrm{cm}$
charge spread	$(1.42 \pm 0.11)\,\mu\mathrm{m}$	$(2.01 \pm 0.16)\,\mu\mathrm{m}$
cluster size	1.072 ± 0.006	1.102 ± 0.008

Table 9.2: Limits for the cluster size set by the model.

efficient readout, and also recombinations of electrons and holes (e.g. on defects or impurities in the lattice structure of the silicon) are neglected.
Furthermore, it is assumed that the ionizing particles are traversing the pixel perpendicularly and no charge sharing and cluster formation is caused by particles inciding under a tilted angle. This assumption is reasonable for the collimated particles from the testbeam.
A crucial point is that the spread of created electrons due to the kinetic energy gained from the ionizing particle is neglected in this model. This is only the case if the energy loss of the traversing particle in a single collision is low. Simulations for low energy electrons in silicon suggest a range of below $0.1\,\mu\mathrm{m}$ for electrons up to a few keV (cf. [42]). The spread of electrons produced with higher energies has a sizable contribution due to the initial kinetic energy that would be needed to be taken into account by the cluster size calculation in this model. However, calculations for $100\,\mu\mathrm{m}$ thick silicon detectors done in [43] suggest that the number of collisions with large energy transfer of more than $4\,\mathrm{keV}$ is comparatively low (≈ 1 out of 400).

10. Efficiency curve models

For a pixel detector to perform as intended, the hit detection threshold has to be lowered to a level to satisfy both efficiency and noise rate requirements: A too low threshold means that a large number of noise hits are detected, which badly affects the performance of the sensor. If the threshold level is set too high, the efficiency drops and real hits will remain undetected. In order to find the optimal working point of the sensor one can look at the relation between the threshold level and the efficiency. The resulting relation has the shape of a skewed S-curve, termed efficiency curve in the following.
Various model functions can be used to describe these efficiency curves, which will be described in this section. First, to understand the foundation of the models, the meaning of the efficiency curve is explained. As was discussed in Section 4, the energy deposition underlies fluctuations and follows a certain probability distribution. The charge deposited as per this distribution is read out and then transferred into a signal height. In the readout process Gaussian noise is superimposed to this signal height. Finally, a threshold is applied and effectively diminishes the signal height by a constant value[10]. If the threshold was set to zero all charge deposited would be detected and the efficiency would be 100 %. Increasing the threshold allows only larger signals to be detected, and by this, the deposited charge corresponding to a signal height below the threshold is not detected. This allows to calculate the efficiency as the fraction of the distribution of the signal height which corresponds to signals above the threshold as is depicted in Figure 10.1. Thus, to get a model for the efficiency curve, a model for the signal height distribution is needed. Assuming a linear relation between the signal amplitude and the deposited energy, the distribution function for the signal height is given by the distribution function f of the deposited energy folded with a Gauss G_{σ_n} with noise σ_n. As a result, the efficiency ϵ as a function of threshold t can be calculated as

$$\epsilon(t) = \int_t^\infty (f * G_{\sigma_n})(\lambda) d\lambda \,. \tag{10.1}$$

In turn, the derivative yields the signal height distribution after the comparator, which in principle follows the distribution of a straggling function as introduced in Section 4.1.3[11].
It is to be mentioned here that the signal height distribution, in contrast to the models presented for the straggling function in the following, is zero for negative values of thresholds and also for values above the amplifier saturation. Furthermore, the signal height distribution is a probability density function and therefore has to be normalized. This means, to obtain the efficiency curve from the integration of a straggling function modeling the signal height distribution the straggling function has to be set to zero for negative thresholds and for values above the

[10] This value is not actually constant, but underlies variations of $\approx 10\,\mathrm{mV}$ (untuned sensor, cf. [29]). Effects caused hereby can be taken into account for by the Gaussian noise.
[11] The straggling function is given by the negative of the derivative of the efficiency curve. In the following, this is assumed implicitly and not mentioned for reasons of simplicity.

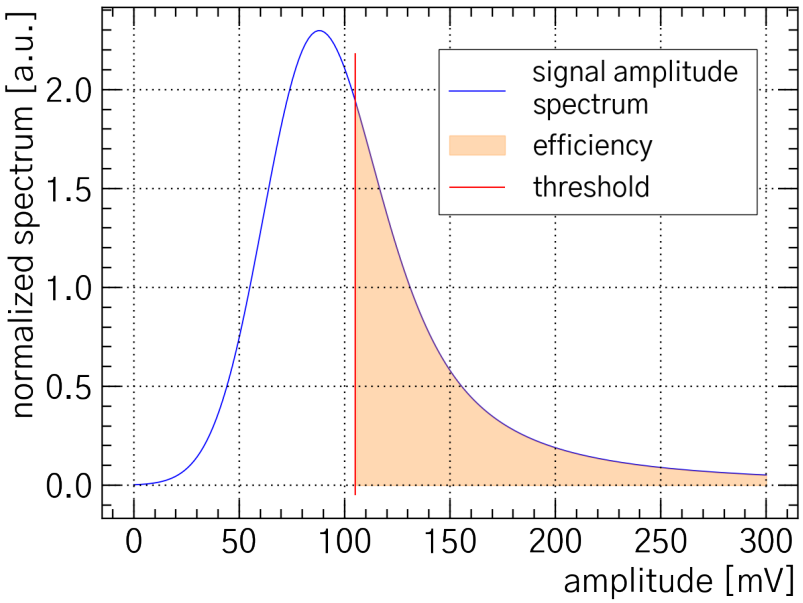

Figure 10.1: Efficiency calculation as the integral of a signal height distribution with arbitrary parameters.

amplifier saturation. For the fit of the efficiency curve this is expected to be insignificant. This is true if the fraction of signals in the amplifier saturation can be neglected. In this case it is sufficient to assume the upper integration bound to be infinity.
For the numerical integration a sufficiently large number is used as the upper bound. The condition for such a number N to be sufficient is the following: The ratio of the integral over the straggling function in the bounds of the largest threshold used and N and the integral in the bounds of 0 and N must not be sensitive to small changes of N.

10.1. Skewed error function

An empirical model to describe the shape of the efficiency curve is given by a skewed complementary error function, adapted from [44]:

$$f(t) = \frac{1}{2}\left(1 - \operatorname{erf}\left[x(t)\left(1 - 0.6\tanh\left(\xi x(t)\right)\right)\right]\right) \tag{10.2}$$

with the parameter $x(t) = \frac{t-\mu}{\sigma}$. In this function t denotes the threshold and μ is the median threshold, which corresponds to an efficiency of 50 % and therefore exactly the half of the signals. Thus, the median thresholds corresponds also to the

median charge deposition of a traversing particle[12]. The parameter σ is a measure for the width of the distribution and ξ describes the skewness of the function. The function describes the efficiency curves only empirically, which makes it hard to interpret the parameters physically. Furthermore, the median of the deposited charge is not a stable parameter to describe this function, since it has a strong dependence on the maximal possible energy transfer in a single collision.
However, for applications in which only an interpolation of the efficiency curve is required, the skewed error function provides a suitable model, and the fit is not very computation intensive.
In contrast to the skewed error function the three models described next start with a model for the straggling function, which is then integrated to get the efficiency curve. Therefore, these models allow for consideration of the readout noise by a Gauss convolution as noted in Equation 10.1. The convolution is implemented numerically based on [45].

10.2. Skewed Gaussian distribution

Another empirical model is the one of an integrated skewed Gauss. In this model the function of a skewed Gauss is used to describe the underlying straggling function, which is subsequently integrated to obtain the efficiency curve. A skewed Gauss can be described by

$$s(\lambda) = \exp\left(-\frac{1}{2}\frac{1}{\left(\frac{\sigma_0}{\lambda-\mu}+\sigma_a\right)^2}\right). \tag{10.3}$$

Here σ_0 corresponds to the width of the distribution at the peak, which is located at μ. The parameter σ_a is used to skew the distribution by increasing its with towards one side of the mean and decreasing it towards the other side. To model the shape of a straggling function in a reasonable way bounds should be set for this parameter to $0 \leq \sigma_a \lesssim 0.2$, as discussed in more detail in Appendix C.
With this, an efficiency curve model is given by

$$f(t) = \frac{1}{\mathcal{N}} \int_t^N s(\lambda) d\lambda \tag{10.4}$$

with

$$\mathcal{N} = \int_0^N s(\lambda) d\lambda \tag{10.5}$$

with N sufficiently large, as aforementioned.

[12]This only holds for the assumption of a linear relation between signal height and charge deposition.

10.3. Landau distribution

For sufficiently high absorber thicknesses[13] ($\gtrsim 2\,\mathrm{mm}$, [18]) the energy loss fluctuations follow a (scaled and shifted) Landau distribution. This distribution was introduced by Landau in 1944 under the assumption of arbitrarily large energy transfers ($T_{max} \to \infty$) and neglecting the shell-corrections and the absolute energy change of the particle traversing the detector material ([46]). The distribution (see Figure 10.2) shows a peak at ≈ -0.22278 and has a full-width at half maximum (FWHM) of ≈ 4.018.

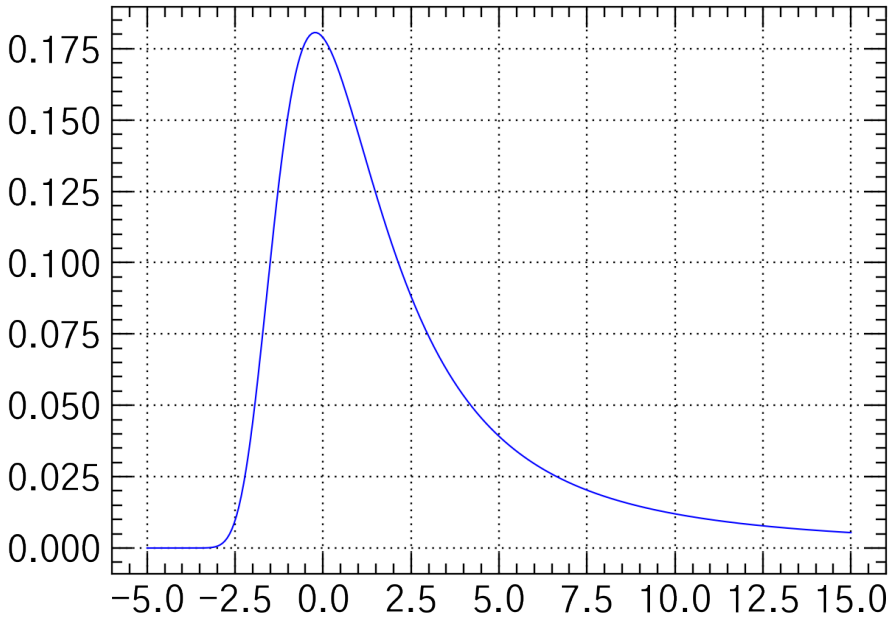

Figure 10.2: Probability density function (PDF) of a Landau distribution.

A formula by which the Landau distribution can be represented is given by the following integral ([10])

$$s(\lambda) = \frac{1}{\pi} \int_0^\infty e^{-t \ln(t) - \lambda t} \sin(\pi t)\, dt\,. \tag{10.6}$$

[13] The terms *absorber*, *detector* or *sensor thickness* in the context of energy loss straggling mean the material thickness in which deposited energy is contributing to the induced signal height weighted with the contribution to the height. This is not necessarily the actual thickness of a chip or the depletion depth since also charge which is collected by diffusion can potentially contribute to the signal height.

To shift and scale the width of this distribution a linear transformation

$$\lambda \rightarrow \frac{\lambda - \mu}{\sigma} - 0.22278 \tag{10.7}$$

can be done. With this, μ describes the *most-probable value* (MPV) of the distribution and σ is a measure for the width. In contrast to the skewed error function and the skewed Gaussian distribution the Landau distribution only has two parameters.

The Landau distribution is numerically implemented in the *ROOT* framework [47]. For the fitting procedure in the scope of this thesis the Landau is evaluated numerically with the *CERNLIB G110 denlan* algorithm [48].
As for the skewed Gauss distribution in Equation 10.4, to obtain the function for the efficiency curve the Landau has to be integrated and the integral has to be normalized.

For thin sensors, the use of a Landau distribution to describe the fluctuations is not justified anymore and different approaches have to be taken as has been pointed out in [18]. In [49], the breakdown of the model is described to be caused by the fact that the energy loss cross section which has been used by Landau to obtain the distribution is not entirely right. Deviations from the real cross section caused by the binding energy of the electrons in the traversing material have an increasing impact for thinner sensors. To account for these binding energies and, by this, model the real cross section more accurately it has been suggested in [50] to convolve the Landau distribution with a Gauss distribution. Consequently, for thin sensors the straggling distribution is broader than a simple Landau.

10.4. Moyal distribution

A distribution to model the straggling function has been introduced by José Enrique Moyal in [16]. This distribution is given by a double-exponential function:

$$s(\lambda) = \frac{1}{\sqrt{2\pi}} e^{-\frac{1}{2}\left(\lambda + e^{-\lambda}\right)} . \tag{10.8}$$

As for the Landau distribution, a scaling and shifting of this distribution can be performed by the transformation

$$\lambda \rightarrow \frac{\lambda - \mu}{\sigma} \tag{10.9}$$

with the two parameters μ and σ corresponding to the peak position and width of the distribution. In order to get the model for the efficiency curve, the Moyal distribution is integrated and normalized as in Equation 10.4.

Compared to the Landau distribution, the Moyal distribution decreases faster

towards high energies. A comparison of the Landau and Moyal distribution can be found in Figure 10.3.

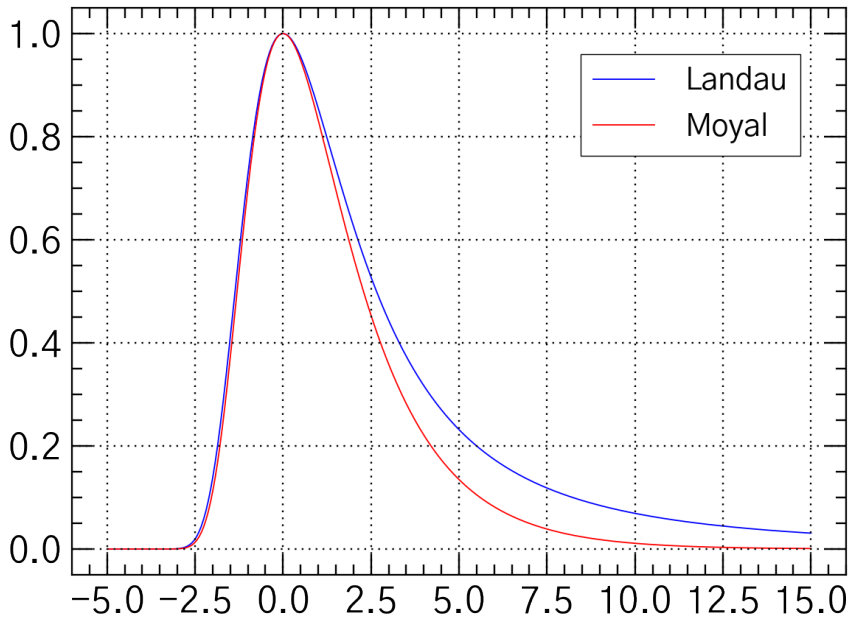

Figure 10.3: Comparison of a Landau[14] and Moyal distribution – scaled to same peak height.

[14]MPV shifted to zero

11. Sensor thickness model and calculation

The thickness of the material in which charges are created contributing to the signal (simply *sensor thickness* in the following) can be determined by the shape of the straggling function for the energy loss. First, it is important to understand what *sensor thickness* in this context means. As previously mentioned, this is not the depletion depth or the actual thickness of a chip.

11.1. Model for a weighted sensor thickness

The sensor thickness discussed in the following corresponds to the thickness in which energy is deposited. Therefore, it seems reasonable to assume this thickness to be given by the actual sensor thickness weighted with the fraction of deposited energy which creates charges contributing to the signal. For this, the following function, which is representing a model for the signal height contribution depending on the position of the energy loss along the depth x of the sensor, can be used:

$$f(x) = \frac{1}{r} \begin{cases} e^{-\frac{(x-a)^2}{2\sigma_0^2}} & , \ 0 < x < a \\ 1 & , \ a < x < d - a \\ e^{-\frac{(x-(d-a))^2}{2\sigma_1^2}} & , \ a < x < r \end{cases} . \tag{11.1}$$

Within this model, the sensor thickness as it is described above is given by

$$t = r f(x) . \tag{11.2}$$

The meaning of the parameters is explained in the following, and a schematic elucidation of the function f can be found in Figure 11.1. The parameter r denotes the full sensor depth. The depletion depth is given by d, and the charge deposited in this region is assumed to fully contribute to the signal height. Along the range between the top of the sensor ($x = 0$) and a depth a the electronics of the sensor are located. Charge from this region can contribute to the signal height in principle but the contribution is assumed small. The importance of charge collection via diffusion decreases with the distance of the initial charge deposition to the depleted area. This can be accounted for by a Gaussian distribution with a width σ_0. Analogously, the charge collection via diffusion beyond the depletion zone can be taken into account with a Gauss with a width σ_1, which most likely is not the same as σ_0 since the charge diffusion in the electronics part is expected to differ from diffusion in simple bulk material due to the microelectronic structures. The parameters in this model – the depth a of the electronics part, the diffusion

parameters σ_0 and σ_1 and the depletion depth d – are unknown for the MuPix10 chip.

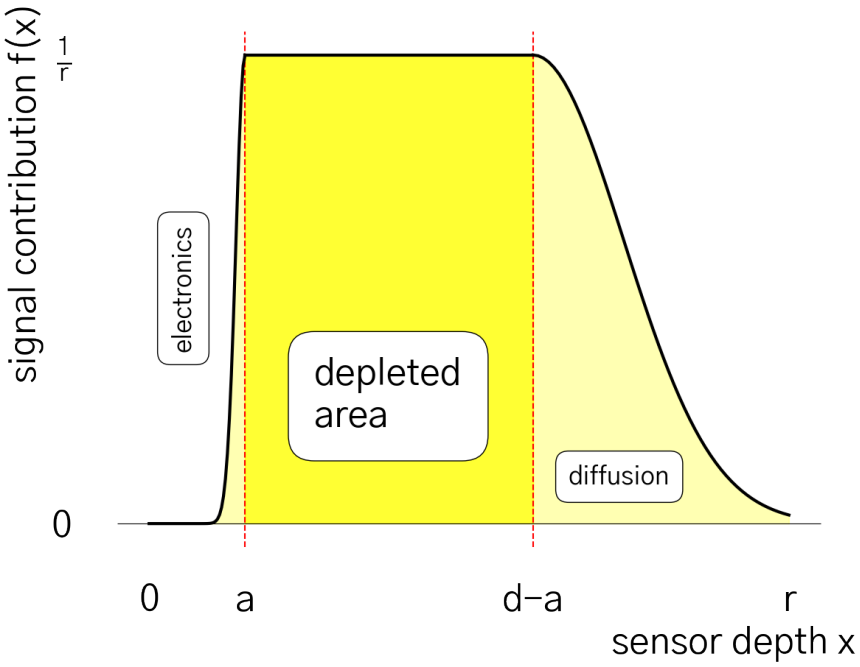

Figure 11.1: Model for the contribution of the different sensor depths to the signal height.

11.2. Sensor thickness dependence on the straggling function

As described in [18] and [17] the parameter λ in the Landau distribution (see Equation 10.6) is given by

$$\lambda = \frac{\Delta - \overline{\Delta}}{\xi} - (1 - \Gamma) - \beta^2 - \ln \kappa \,. \tag{11.3}$$

In this equation Δ is the energy loss and $\overline{\Delta}$ is the mean energy loss, given by

$$\overline{\Delta} = 2\xi B \tag{11.4}$$

with the stopping power B and the factor ξ, which can be obtained from the Bethe-Bloch formula in Equation 4.1:

$$B = \frac{1}{2}\ln\left(\frac{2m_e c^2\beta^2\gamma^2 T_{max}}{I^2}\right) - \beta^2 - \frac{\delta(\beta\gamma)}{2} \tag{11.5}$$

and

$$\xi = \frac{1}{2}K\frac{Z}{m_A}\rho\frac{z^2}{\beta^2}t\,. \tag{11.6}$$

Furthermore, t is the sensor thickness (see Section 11.1), $\Gamma \approx 0.5772$ denotes Euler's constant and the ratio κ is defined as

$$\kappa = \frac{\xi}{T_{max}}\,. \tag{11.7}$$

With this, comparing the expression in Equation 11.3 to the form of Equation 10.7 yields (note: the σ in this case is not a Gaussian width, but it is the scaling parameter for the Landau distribution – often called ξ as well)

$$\frac{\Delta-\mu}{\sigma} - 0.22278 = \frac{\Delta - \left(\overline{\Delta} + (1-\Gamma-0.22278)\xi + \beta^2\xi + \xi\ln\kappa\right)}{\xi} - 0.22278\,. \tag{11.8}$$

This means, the value for the MPV is given by

$$\mu = \xi(2.2000 + \beta^2 + \ln\frac{\xi}{T_{max}}) \tag{11.9}$$

and the ratio of the MPV μ and the width σ can be identified with

$$\frac{\mu}{\sigma} = \frac{\overline{\Delta}}{\xi} + (1-\Gamma-0.22278) + \beta^2 + \ln\kappa \tag{11.10a}$$

$$= \ln\left(\frac{K\rho Z m_e c^2 z^2\gamma^2}{m_A I^2}t\right) - \beta^2 - \delta(\beta\gamma) + 0.2000\,. \tag{11.10b}$$

For 4 GeV/c electrons and positrons in silicon this becomes

$$\frac{\mu}{\sigma} = 10.05 + \ln\frac{t}{\mu\mathrm{m}}\,. \tag{11.11}$$

For this case the following values have been used:

- $\rho = 2.329\,\mathrm{g\,cm^{-3}}$, [22]
- $Z = 14$, $z = 1$
- $\gamma = 7827.8$, $\beta = 1$
- $m_A = 28.085\,\mathrm{u}$, [22]
- $I = 173\,\mathrm{eV}$, [10]
- $\delta(\beta\gamma) = 13.495\,.$

The density correction $\delta(\beta\gamma)$ has been calculated with Sternheimer's parametrization given in [10].
With this in general the determination of the sensor thickness is possible by fitting an integrated Landau to the efficiency curve. Under the assumption of a linear dependence between signal height and deposited charge no further information is needed. In particular, no energy calibration of the sensor is necessary for this method. However, the sensor thickness depends exponentially on the ratio $\frac{\mu}{\sigma}$:

$$t\,[\mu\mathrm{m}] = e^{\frac{\mu}{\sigma} - 10.05}\,. \tag{11.12}$$

This means small systematic errors in the model and statistical errors in the determination of the ratio heavily compromise the result for the thickness.

An alternative way is to use the width parameter ξ of the Landau distribution and Equation 11.6 to obtain the thickness t. The scaling in this relation is linear and therefore much less error-prone than the determination according to Equation 11.12. One drawback with this is that an energy calibration is required for this method, i.e. it demands a relation between deposited energy and signal height. Such a calibration can be obtained by exploiting the characteristics of particles of definite energies, which deposit all their energy in the sensor. With such particles a threshold scan can be performed and the number of hit counts as a function of the threshold has the shape of a skewed S-curve given by the integrated straggling function as introduced in Section 10. The MPV of the underlying straggling function obtained from this fit corresponds to the particle energy. This measurement performed for different particle energies allows to determine the relation between the MPV for signal height and the deposited energy, which can be fitted by a reasonable function and yields the desired energy calibration. Alternatively this fit can be done for the median instead of the MPV, but the method using the MPV is assumed to perform better since the MPV is a more stable parameter to describe a straggling function than the median. In any case, such an energy calibration is complex and has not been performed for this thesis.

12. Sensor resistivity

The resistivity of the sensor material determines important quantities of the sensor like the depletion depth (see Equation 9.7). It is therefore of great interest to know it to a high precision. Since the manufacturer of the silicon wafers used for the sensors analyzed in the scope of this thesis specifies the value of the resistivity only to the range from $200\,\Omega\,\mathrm{cm}$ to $400\,\Omega\,\mathrm{cm}$ it is desirable to obtain a more precise value. One possible procedure to get the resistivity uses just the relation in Equation 9.7 and is explained in the following:
The efficiency curve of the sensor is determined for different HV values (for details see Section 10 and Section 14) and the MPV of the underlying straggling function is obtained from a fit to this efficiency curve. An energy calibration with the MPV as explained in Section 11.2 can then be used to obtain the corresponding energy deposition for the MPV of each HV value. With this a relation between the energy deposition and the HV is obtained. To get the resistivity from this relation the MPV is expressed as a function of the thickness t (see Equation 11.9 with $\xi \propto t$). Thus, the relation between the thickness and the MPV can be described by a function of the form

$$MPV = at \cdot (b + \ln t) \tag{12.1}$$

with parameters $a,\ b$.
Furthermore, the relation between the HV U and the sensor thickness is adapted from Equation 9.7 and assumed to be

$$t = c + \sqrt{dU} \tag{12.2}$$

with parameters c and d. The parameter d contains the resistivity ρ as

$$\rho = 4.8 \times 10^{11} \frac{d}{\mu_h} \Omega\,\mathrm{cm\,s^{-1}} \tag{12.3}$$

with notations as in Equation 9.7. The parameter c in Equation 12.2 is due the diffusion. As can be understood from the model presented in Section 11.1, the sensor thickness contributing to the signal height is non-zero even for no depletion because charge for the signal is still collected via diffusion. This justifies the offset in Equation 12.2.
If Equation 12.2 is applied to Equation 12.1, a relation between the MPV and the HV is obtained, which can be fitted with the parameters $a,\ b,\ c$ and d in Equation 12.1 and Equation 12.2. Subsequently, the resistivity is obtained from the parameter d according to Equation 12.3.
Furthermore, the importance of the effect of charge collection via diffusion can be assessed from such a fitting procedure. For this, the fitting as aforementioned can be performed for sensors of different actual thicknesses and the fit parameter c allows to draw conclusions on the diffusion contribution. In particular, if diffusion plays a substantial role one would expect the fit parameter c to be smaller for the thin sensor in which potentially less bulk material can contribute to the charge collection via diffusion leading to a smaller diffusion offset. In turn, no major

difference is expected if diffusion is not important.
This procedure, as has been mentioned before, needs an energy calibration and therefore goes beyond the scope of this thesis. It is thought to serve as the basis for further studies.

Results

The following results are obtained for a MuPix10 sensor at the *Deutsches Elektronen-Synchrotron* (DESY) testbeam facility with 4 GeV/c electrons and positrons. Threshold scans have been performed for high voltages between −10 V and −100 V[15] in steps of 10 V for a 100 µm thick sensor from a 200 Ω cm wafer[16]. Additionally, threshold scans for a 50 µm, 60 µm and 70 µm sensor have been carried out for high voltages of −20 V, −40 V and −70 V, respectively.

13. Results for the cluster size model

The cluster sizes have been analyzed for the HV-scan and the results are compared to the model derived in Section 9.2. For each threshold at each HV a clustering algorithm is performed and the cluster sizes of all clusters that could be matched to a particle track[17] is determined. The mean value of the cluster size is the quantity of interest, that corresponds to the cluster size obtained by the model. However, since the model for cluster formation assumes a threshold level of zero, it is necessary to extrapolate the obtained mean cluster sizes from each threshold scan to a threshold of zero in order to compare the data and the model. In Figure 13.1 the mean cluster sizes are plotted for the threshold scans in the HV-scan. There are two effects mainly affecting the shape of theses curves:

In the low threshold region (for each HV roughly the region below the minimum cluster size in Figure 13.1) the cluster size decreases with increasing thresholds. The reason for this is that more and more pixels which gain only little charge by the effect of charge sharing will not make the threshold yielding smaller cluster sizes.

For the region of high thresholds (for each HV roughly the region beyond the minimum cluster size in Figure 13.1) this effect becomes secondary. In this region the efficiency drops and even clusters of size 1 can remain undetected. This means the share of very large energy depositions, finally energy depositions that can even cause δ-electrons that lead to large clusters increases. This explains the rise of

[15] For reasons of simplicity in the following the minus sign is disregarded if no confusion is to be expected.
[16] In the following, these measurements are referred to as the HV-scan.
[17] By this, noise clusters can be excluded.

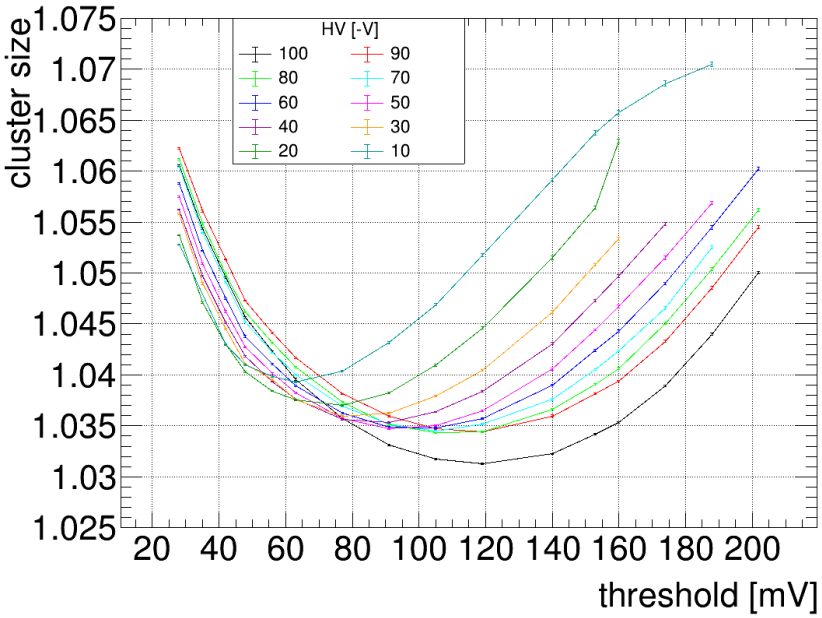

Figure 13.1: Mean cluster sizes for the HV-scan.

the cluster size for high thresholds.
Since the extrapolation towards a threshold of zero is done in the region where the first effect is dominating, it is sensible to use the range of low thresholds for the fit. However, for different HV values the rise of the cluster size begins at different thresholds and for the lowest HV values this rise starts for comparatively low thresholds already. This makes it difficult to determine a fit range, which is large enough to contain a reasonable number of data points for the fit but not too much data points which are affected already by the drop of the efficiency and the resulting increase of the cluster size.
A fit of a quadratic polynomial to the first 5 data points, corresponding to a fit range of 0 to 60 mV, is assumed to work best[18]. Additionally, the fit of a polynomial of degree 4 is performed to all data points for comparison.
The results which are obtained for the extrapolated cluster sizes at zero threshold are plotted in Figure 13.2 along with the predicted cluster sizes for resistivities of 200 Ω cm and 400 Ω cm. No significant dependence on the high voltage is visible as predicted by the model in Section 9.2 and the measured cluster sizes lie within this range. The data points suggest – given the model for the cluster size – a resistivity close to 400 Ω cm, which is consistent with measurements of the sensor breakdown voltage that have been taken [51].

To verify the consistency of the results and the model an alternative approach can be chosen by starting from the obtained cluster size. The ratio of the number of clusters of size two and the number of all clusters can be used to calculate the according spread in the geometrical model in Section 9.2, which than should agree

[18] For the 10 V scan there are only 4 data points in the applied fit range, which lowers the significance of the corresponding fit.

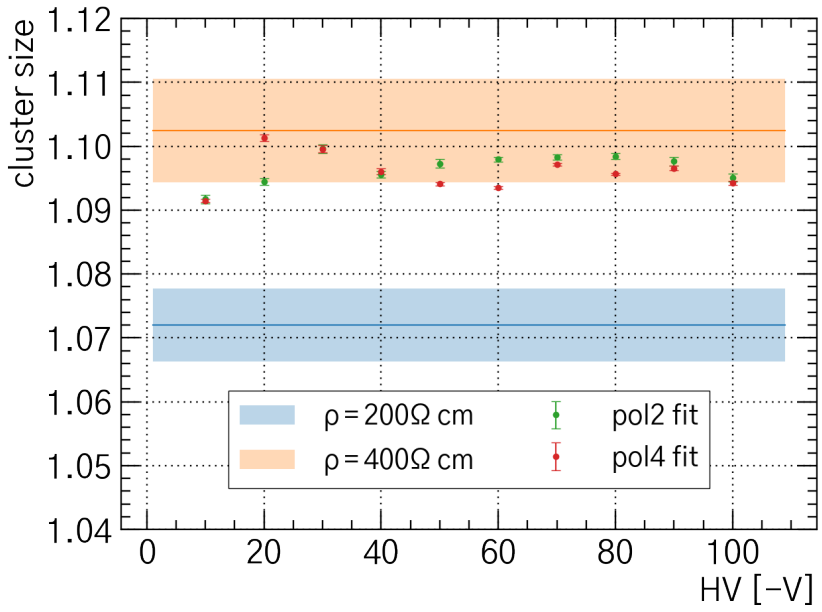

Figure 13.2: Extrapolated cluster sizes at zero threshold.

with the charge spread range obtained in Table 9.1.
In Figure 13.3 the ratio of clusters of size 2 and all clusters is plotted for the HV-scan and for the various thresholds. The ratios used for further calculation are obtained by fitting the ratios in each threshold scans with a quadratic polynomial in the same range as described above and extrapolating to a threshold of zero. As expected, also in this plot no significant HV dependence of the cluster sizes is obtained. To get a value for the fraction of clusters of size two the mean of the fractions for all HV values is used, and it is calculated to

$$f_{2/all} := \frac{\#\text{clusters of size 2}}{\#\text{all clusters}} = 0.075 \pm 0.003\,.$$

Using the areas for the different cluster sizes in Figure 9.1 yields the following equations (with denotations as in Equation 9.10)

$$f_{2/all} = \frac{4s(d-2s)}{d^2} \tag{13.1}$$

$$\Rightarrow \quad s = \frac{1}{4}\left(d - \sqrt{d^2(1-2f_{2/all})}\right)\,. \tag{13.2}$$

Finally, the charge spread is calculated with this model to a value of

$$s = (1.55 \pm 0.07)\,\mu\text{m}\,,$$

which agrees with the range obtained in Table 9.1.

A further check of the validity of the model can be done by considering the

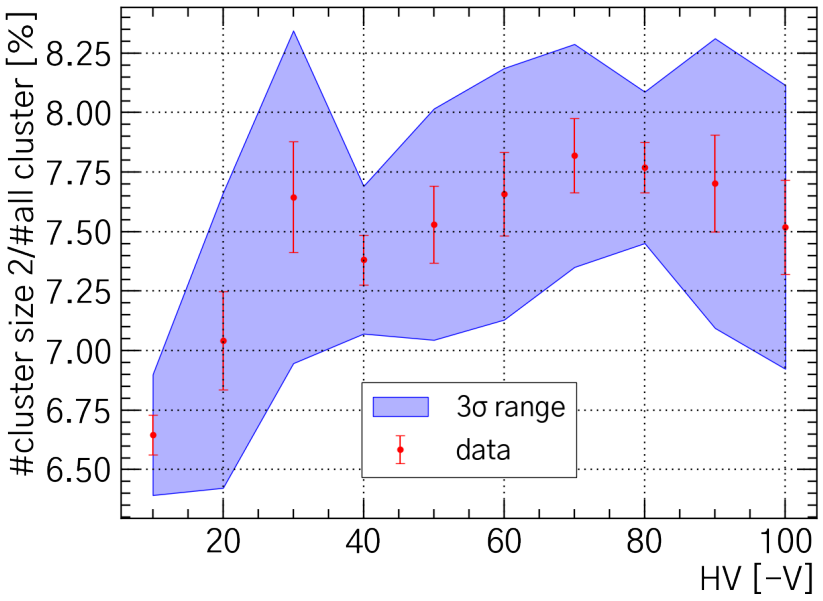

Figure 13.3: Ratio of clusters of size 2 and all clusters.

fraction for the different cluster sizes and comparing the predictions from the model to the data obtained by the testbeam measurements.
For this, the fractions of clusters of size 3 and 4 for the HV-scan have been obtained by the same procedure as for the clusters of size 2. The resulting plots are shown in Figure 13.4 and Figure 13.5. For the clusters of size 4 the lower error was bound for physical reasons since a negative fraction of clusters is not reasonable. The mean fraction is calculated for each cluster size and compared to the cluster sizes that are geometrically obtained by the model. For a charge spread s and the pixel of size $d \times d$ the model yields for the fractions $f_{i/all}$ of clusters of size i ($i \in \{1, 2, 3, 4\}$)

$$f_{1/all} = \frac{(d-2s)^2}{d^2} \tag{13.3}$$

$$f_{2/all} = \frac{4(d-2s)s}{d^2} \tag{13.4}$$

$$f_{3/all} = \frac{s^2(4-\pi)}{d^2} \tag{13.5}$$

$$f_{4/all} = \frac{\pi s^2}{d^2}\,. \tag{13.6}$$

With this, results for the lower limit of the sensor resistivity of 200 Ω cm and the upper limit of 400 Ω cm are obtained by using the corresponding charge spread (cf. Table 9.1). The model results for the 200 Ω cm resistivity are presented in Figure 13.6 and compared to the measured data (obtained as aforementioned). In Figure 13.8 the same plot can be found for a sensor resistivity of 400 Ω cm.

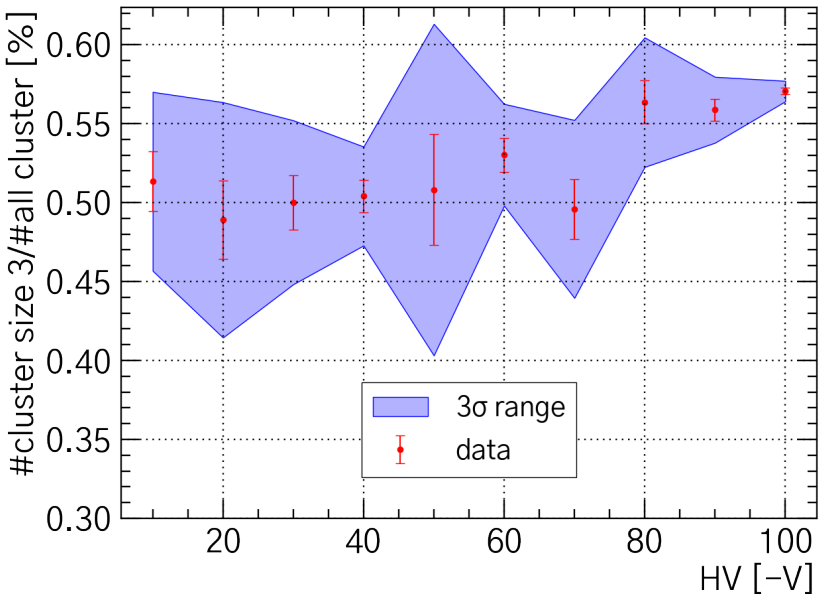

Figure 13.4: Ratio of clusters of size 3 and all clusters.

The differences between the model with the according resistivity and the data are shown in Figure 13.7 and in Figure 13.9, respectively.
Especially from the plots in Figure 13.7 and Figure 13.9 one can obtain the limits of the model. For the clusters of size 1 and 2 the difference between model and data is not significant ($< 3\sigma$). To assess the suitability of the model for these cluster sizes a precise knowledge of the sensor resistivity would be desirable. For the clusters of size 3 and 4 a significant deviation between model prediction and data is obtained independent from the sensor resistivity. Thus, one can infer that the model is not capable of describing clusters of size 3 and 4. The modeled values for these cluster sizes are significantly smaller than the ones obtained from the data.
This can be understood qualitatively considering that large energy transfers causing electrons which are capable of secondary ionizations are disregarded in the model. Such secondary ionizations are expected to create large clusters and, thus, mainly affect the clusters of size 3 and 4 within this model. Furthermore, these secondary ionizing particles can cause clusters of size even larger than 4, which also is not considered within this model.
It is therefore expected that for further improvement of the model a quantitative consideration of large energy transfers would yield better results.

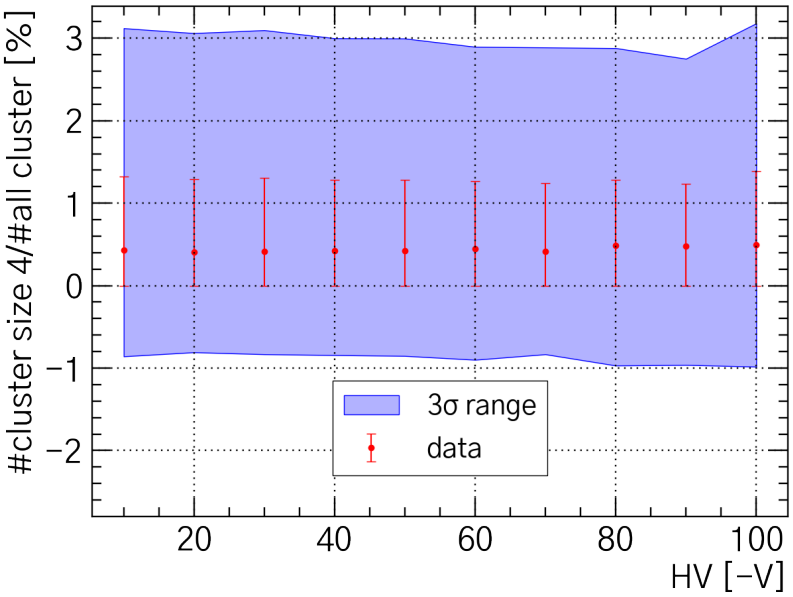

Figure 13.5: Ratio of clusters of size 4 and all clusters.

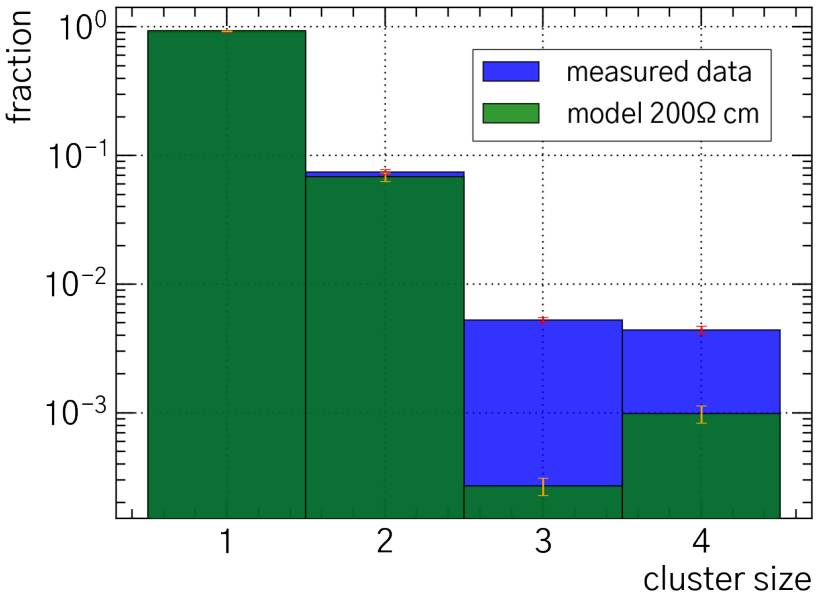

Figure 13.6: Fractions of different cluster sizes for the 200 Ω cm resistivity.

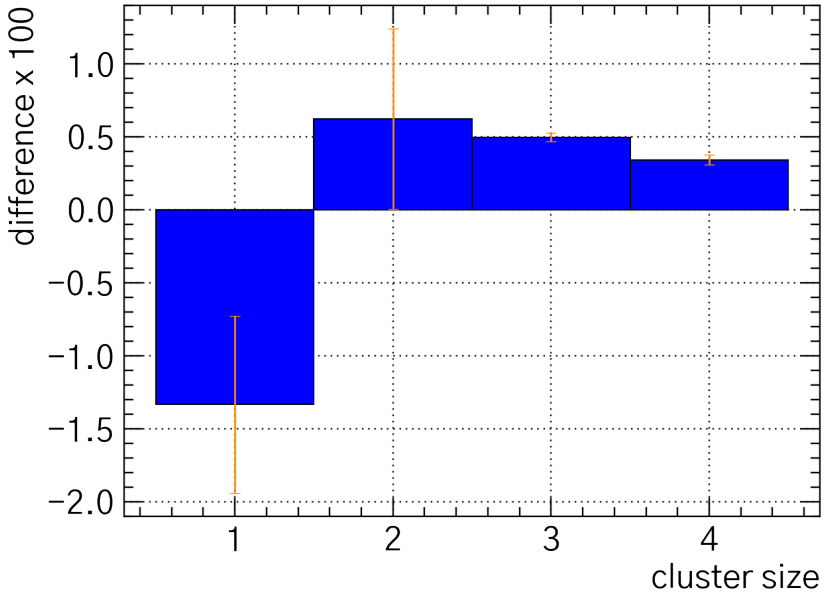

Figure 13.7: Difference of fractions of cluster sizes of the measured data and the model for the 200 Ω cm resistivity.

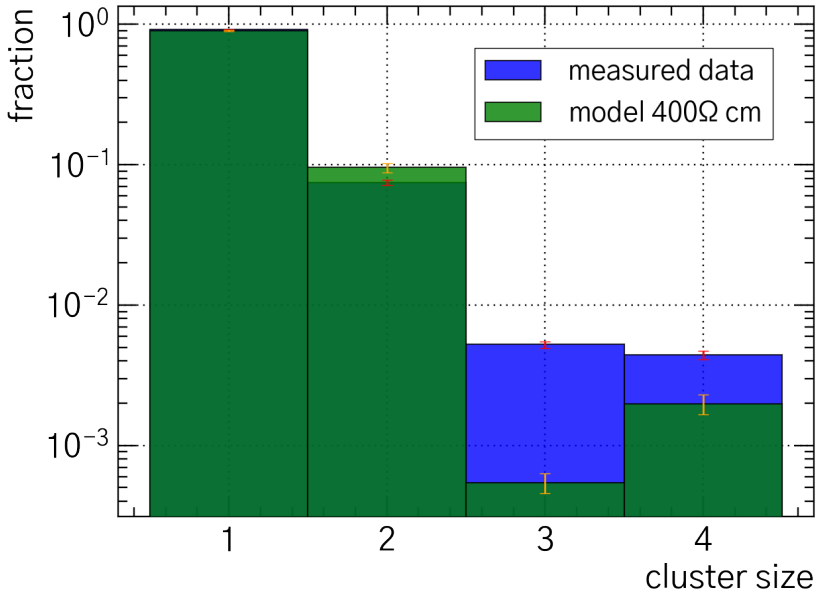

Figure 13.8: Fractions of different cluster sizes for the 400 Ω cm resistivity.

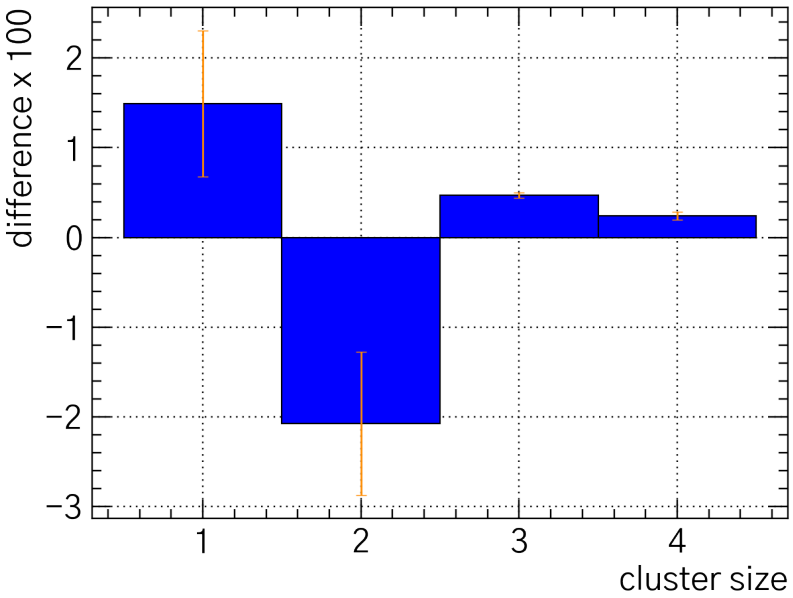

Figure 13.9: Difference of fractions of cluster sizes of the measured data and the model for the 400 Ω cm resistivity.

14. Efficiency curves

The different models introduced in Section 10 have been applied to the efficiency curves of the HV-scan. The underlying measurements have been conducted at a DESY testbeam campaign with a telescope setup (see Section 7.1) for a MuPix10. For this, threshold scans were performed for HV values between $-20\,\mathrm{V}$ and $-100\,\mathrm{V}$. For these scans the efficiency has been calculated as explained in Section 8.1. A 3D visualization of the efficiency dependence on the HV and the threshold is shown in Figure 14.1.

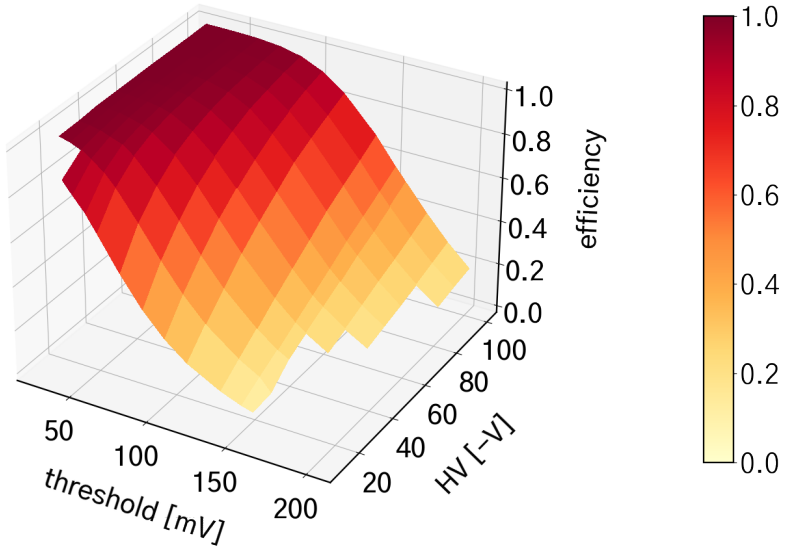

Figure 14.1: 3D visualization of the efficiency obtained in the HV-scan.

14.1. Error calculation

The errors on the efficiency are given by binomial statistics and, thus, are in principle asymmetric (see [33]). They are calculated with the `TEfficiency` class of the *ROOT* framework [52].
The error of the threshold is caused by uncertainties in the measurement procedure for which a digital multimeter with a read-off accuracy of 1 mV is used [31]. This accuracy has been estimated to be the error of the threshold. It has

to be mentioned that the threshold is not directly measured but determined by the difference of the actually set threshold voltage and the baseline voltage. Both values are measured and therefore the error of both measurements would have to be propagated to the thresholds.
The baseline is assumed to be constant for the whole threshold scan and its systematic measurement uncertainty is expected to be the same for all measurements in the threshold scan. This would mean that all threshold errors are correlated, which makes the fitting procedure very complicated.
However, because the uncertainty in the baseline is assumed to only shift the whole efficiency scan and have no effect on the relative positions of the data points, it is reasonable to disregard it for the threshold error and add it quadratically to the fit result of the MPV or median, respectively, which are the only values depending on the absolute position of the thresholds. For the parameters depending only on the relative positions of the thresholds, the baseline has no effect at all.
In order to regard the threshold errors in the least-square fit they are converted into equivalent efficiency errors by the following procedure:
For all data points in one threshold scan the gradient at the threshold position of the data point is estimated. For this, the gradient to the next higher and lower[19] data point is determined by the ratio of the difference in efficiency $\Delta\epsilon$ and of the difference in the threshold Δt:

$$grad = \frac{\Delta\epsilon}{\Delta t}\,. \tag{14.1}$$

Subsequently, the mean of the two gradients is assumed to be the slope of the efficiency curve at this specific data point. This is a reasonable assumption in a quadratic approximation of the efficiency curve.
With this, equivalent efficiency errors are obtained by multiplying the gradient by the threshold error:

$$\text{equivalent efficiency error} = grad \cdot \text{error}_{threshold}\,. \tag{14.2}$$

For the lowest/highest data point no gradient to a lower/higher data point can be calculated. For these data points, the gradient is assumed to be constant, which is a reasonable assumption for approximately linear regions of the efficiency curve. Thus, the gradient is not given by the mean of the upper and lower gradient but just by the upper/lower gradient, respectively.
The errors obtained by this are added quadratically to the errors obtained by the `TEfficiency` class yielding the overall asymmetric efficiency error. The asymmetry of the errors, characterized by

$$\text{error asymmetry} = \frac{error_{low}}{error_{up}} - 1\,, \tag{14.3}$$

is however negligibly small, as can be seen in Figure 14.2. It is therefore justified to assume the error to be symmetric and for the fitting procedure the mean of the upper and the lower error is used as the efficiency error.
In addition to the uncertainties just discussed, systematic deviations from the measured efficiency curve and the models can arise. One effect, especially affecting

[19] *Higher* and *lower* in this context refers to the threshold.

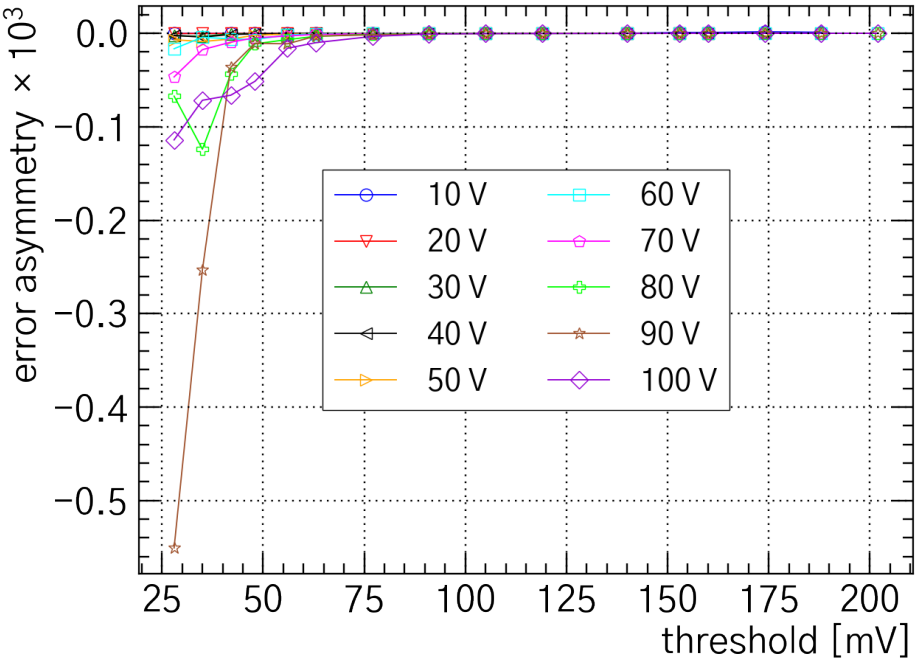

Figure 14.2: Asymmetry of the efficiency errors for the HV-scan.

the data points at low thresholds, is the following:
To get efficiencies close to 100 % (corresponding to low thresholds) signals with only small energy depositions have to be detected. Only few electron-hole pairs are created for these energy depositions. The decrease of the signal height due to recombination of the charge carriers during the collection is in particular crucial for these signals, and it can eventually lead to the signal not crossing the threshold. This causes a systematic deviation between the model and the actually measured efficiency curve.
Furthermore, the decrease of the signal height due to charge sharing for particle hits close to the pixel edges can have the same effect on signals and also add a systematical deviation. With studies on the importance of these effects they can be assessed reasonably and they can be regarded in the calculations. Such a study goes beyond the scope of this thesis and has not been performed. The deviations are therefore disregarded.

14.2. Efficiency curve fitting

The efficiency curves have been fitted to by

- an integrated simple Landau and Gauss-convolution,
- an integrated simple Moyal and Gauss-convolution,

- an integrated skewed Gauss and
- a skewed error function

as introduced in Section 10.
The fit is performed using the `iminuit` *Python* interface of the *C++* based `Minuit2` library [53]. A least-square method is used and the according minimization function has been defined as

$$\chi^2(\vec{\theta}) = \sum_i \frac{\left(\epsilon_i - f(t_i, \vec{\theta})\right)^2}{\sigma_i^2} \tag{14.4}$$

with the efficiency ϵ_i and the threshold t_i of the data point i and error σ_i of the efficiency as calculated above. The fit function is denoted f and parametrized by the set of parameters $\vec{\theta}$.
This function is minimized with regard to the parameters $\vec{\theta}$. The parameters in the global function minimum are assumed to be the best estimate. For the minimization the *MIGRAD* algorithm has been used.
The data point for 160 mV threshold in the 20 V-scan has been excluded from the efficiency curve fitting. This value is systematically lower than expected as Figure 14.3 indicates. In this plot, the efficiency for all HV values in the HV-scan are plotted for the threshold of 160 mV. An empirical linear fit has been performed excluding the 20 V data point. All data points agree within the 1σ-range with this fit except the 20 V point, which is deviating systematically. The reason for this is expected to be an incorrect sensor configuration.

14.3. Comparison of the efficiency curve models

The results obtained by this fitting procedure are presented in the following. Plots of the fit results of the HV-scan for the different models which have been used can be found in Figure 14.4 to Figure 14.11.

The simple integrated Landau fit (Figure 14.4) does, as expected, not work properly. This confirms the prediction in Section 10.3, stating that the Landau function can not be used to describe the energy loss straggling in thin detectors. Therefore, the results obtained from this fit should not be used for physical interpretations.

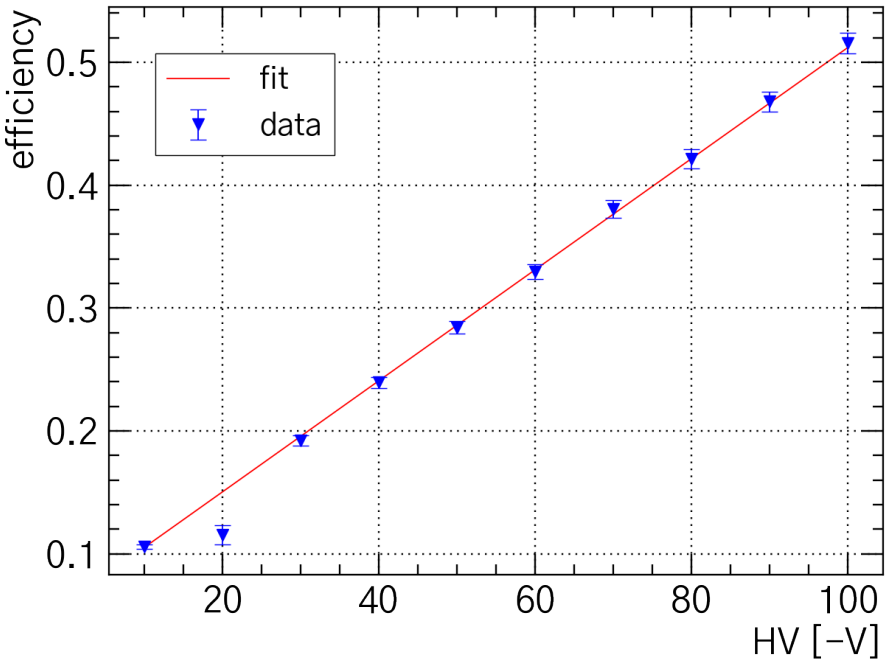

Figure 14.3: Efficiencies depending on the HV for a threshold of 160 mV.

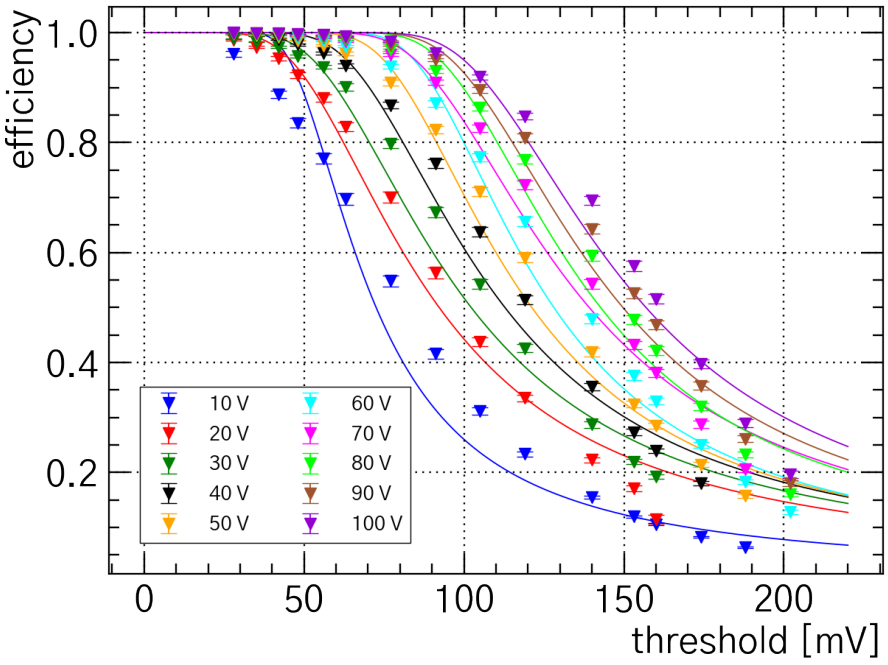

Figure 14.4: Fit of the HV-scan with an integrated Landau distribution.

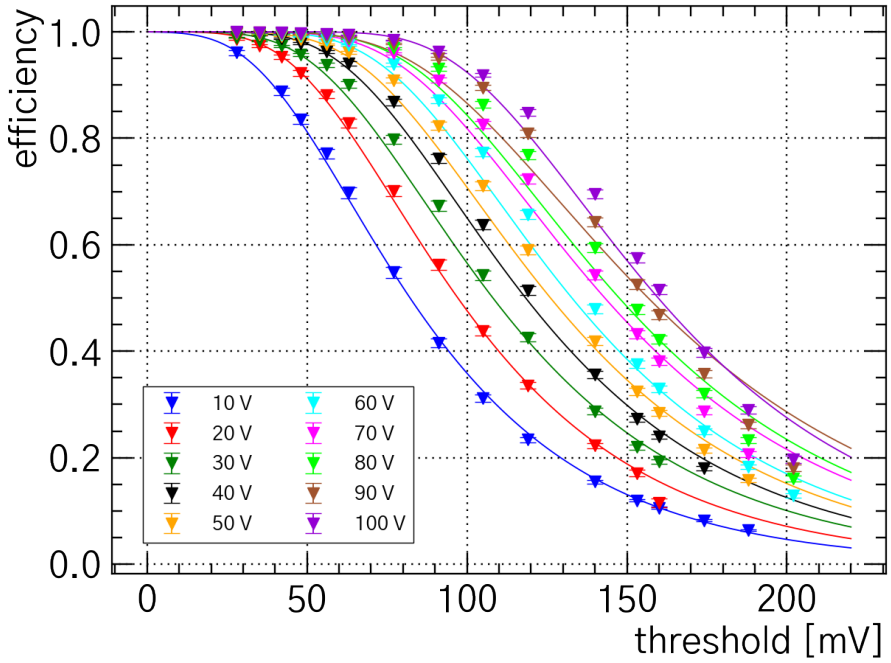

Figure 14.5: Fit of the HV-scan with an integrated Moyal distribution.

The integrated Moyal fit (cf Section 10.4) is a suitable but empirical model to describe the energy loss straggling for very thin sensors. Considering the reduced χ^2 for the Moyal fit of the HV-scan (see Figure 14.12) this model works best for low HV values as the reduced χ^2 is increasing for higher HV values. As for increasing HV values the depletion depth increases (see Equation 9.7) and with this also the weighted thickness (cf. Section 11.1), this means the Moyal distribution suits only the straggling distribution of thin sensors.

The convoluted Landau and Gauss ("*Langau*") has a physical motivation as has been explained in Section 10.3 and its parameters can be related to underlying properties of the sensor material and the interacting particle. It is therefore found to has the best interpretability. In order to obtain physical information from different models, certain properties of these models – like the FWHM or other width parameters – have to be associated with properties of the Landau distribution first before physical interpretation is possible.
The integrated Langau in particular has been found to describe the efficiency curve rather well, with the reduced χ^2 of the fits reasonably low (below 10 for most HV values, see Figure 14.12). The high χ^2_{red} for the high HV values may be caused by a too small error estimation for efficiencies close to one as explained in Section 14.1. This would in particular compromise the threshold scans with the most data points in this high-efficiency region, which are the threshold scans for high HV values. Additionally, the high χ^2_{red} for the 10 V scan may be caused by missing data points for high efficiencies in the plateau region, which has been found to make the fit unstable.

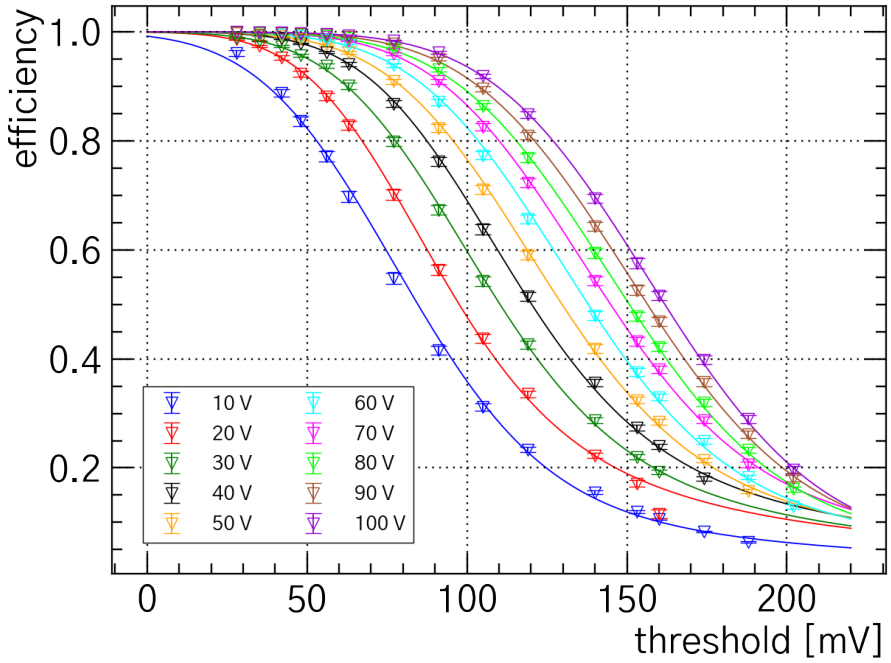

Figure 14.6: Fit of the HV-scan with an integrated Landau and Gauss convolution.

A drawback of the Langau model is the strong (anti-)correlation between the Landau scaling parameter ξ and the Gauss width σ. The correlation between these two parameters, mainly determining the width of the distribution, is obtained from the covariance matrix of the fit result and plotted in Figure 14.7. The values close to -1 mean that the parameters are nearly fully anti-correlated. This is assumed to make the fit result for these parameters highly unreliable. The outlier at 10 V is assumed to be due to the missing data points in the high-efficiency plateau as aforementioned.

The Gaussian width obtained in this fit has two causes: One is the readout noise accounted for by a Gaussian convolution (this is explained in Section 10). The width of the convoluted Gauss can, however, not merely be explained by readout noise, which is assumed to be $\approx 10\,\text{mV}$ (cf. [29]). The second effect broadening the Landau distribution is given by the corrections of the energy loss cross section, introduced in Section 10.3 and results in the large width of the convoluted Gauss.

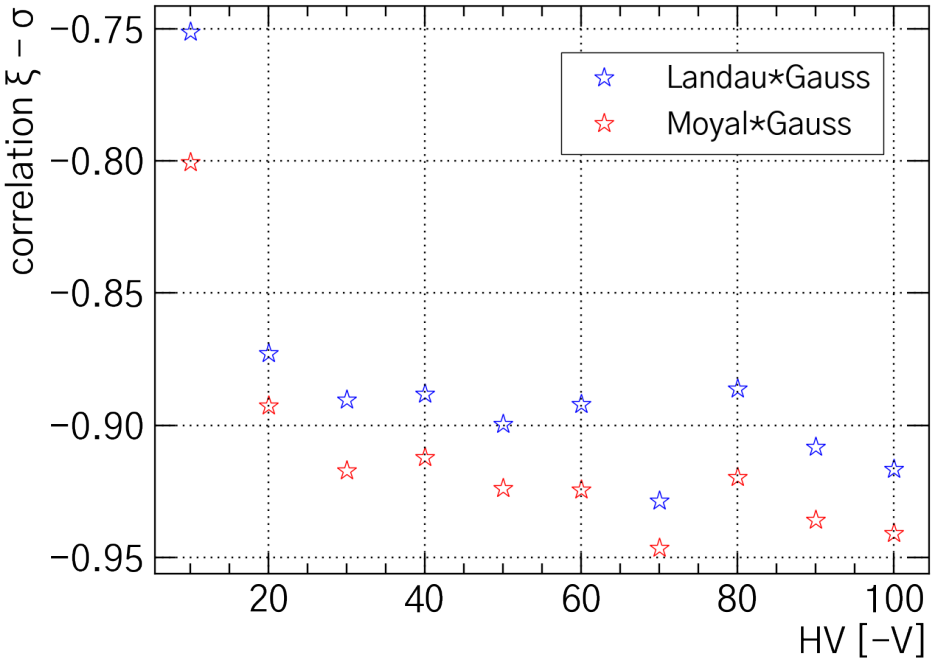

Figure 14.7: Parameter correlation between ξ and σ for the Langau and Moyal and Gauss convolution.

The model with an integrated convoluted Moyal and Gauss distribution shows a similar performance to the Landau and Gauss convolution model as the χ^2_{red} values of the two models are similar for the different HV values. As the simple Moyal distribution already described the threshold scan for the low HV values (thin sensor thicknesses), the Gauss convolution width is expected to be mainly determined by the readout noise. The Gauss width of this convolution is shown in Figure 14.9. In fact, for the low HV values, the width of the Gauss is in the order of what is expected for the readout noise ($\approx 10\,\text{mV}$ as aforementioned). For higher HV values the simple Moyal model does not work, as presented before. The increasing width of the convoluted Gauss in corrects for this inaccuracy, which makes the model suitable for the whole HV range.
As for the Langau, the width parameter ξ of the Moyal distribution and the width σ of the convoluted Gauss have a strong anti-correlation (see Figure 14.7).

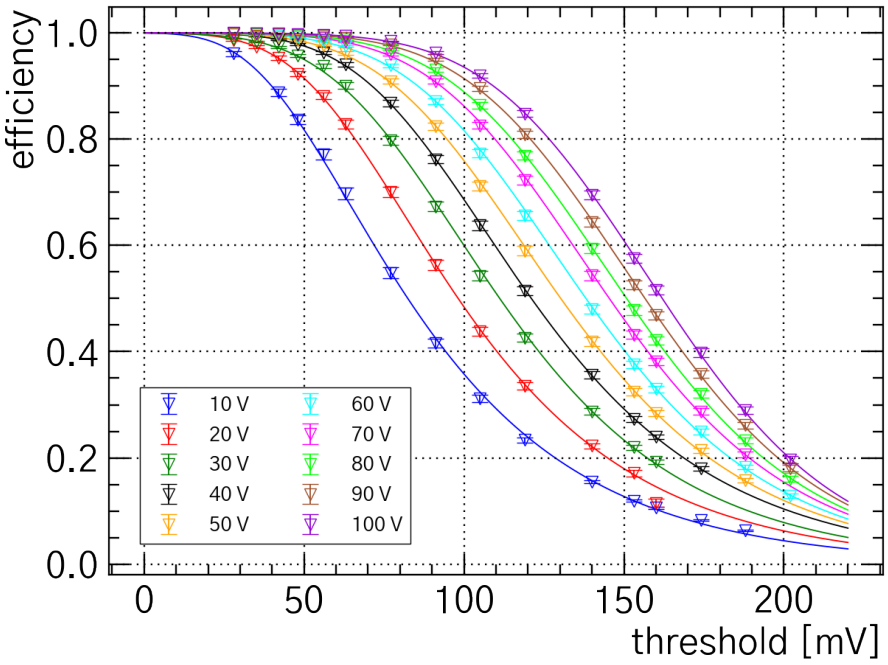

Figure 14.8: Fit of the HV-scan with an integrated Moyal and Gauss convolution.

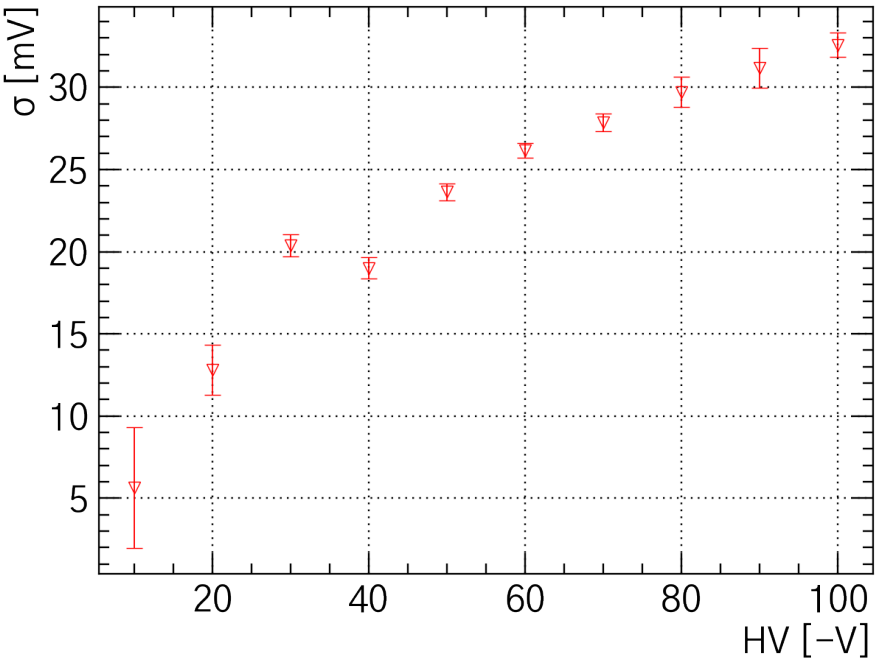

Figure 14.9: Width of the Gauss for the convolution with the Moyal distribution.

The two models of the integrated skewed Gauss and the skewed error function are rather similar. Both basically start with a Gaussian distribution to describe the straggling function and give this distribution a skewness. The only difference is the way how this skewing is obtained. Compared to the Langau and Gauss-convoluted Moyal the skewed Gauss and skewed error function perform similarly regarding the χ^2_{red} with a small tendency to higher χ^2_{red} values for large HV values, i.e. increasing sensor thicknesses. Compared to each other the skewed error function fits the data better for the threshold scans of all HV values except for the 10 V scan, which, as aforementioned, is assumed unreliable due to low statistics in the high efficiency-plateau. The plot containing these results regarding the χ^2_{red} can be found in Figure 14.12.

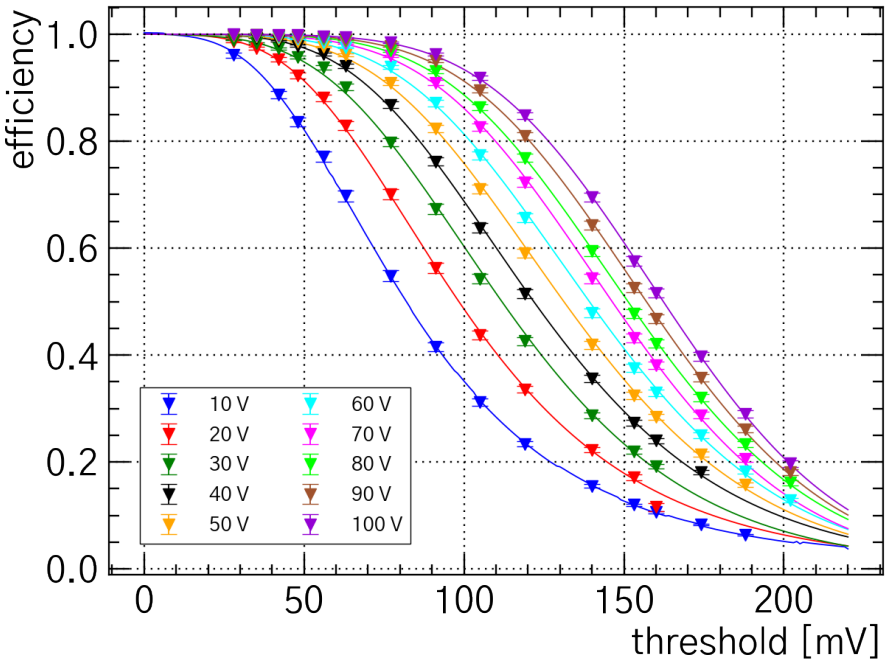

Figure 14.10: Fit of the HV-scan with an integrated skewed Gauss distribution.

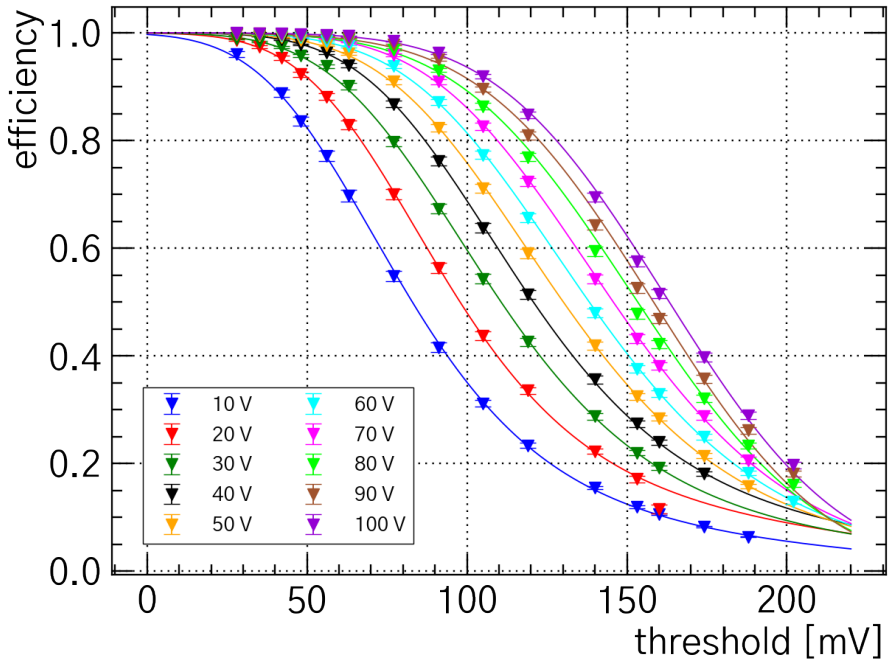

Figure 14.11: Fit of the HV-scan with an skewed error function.

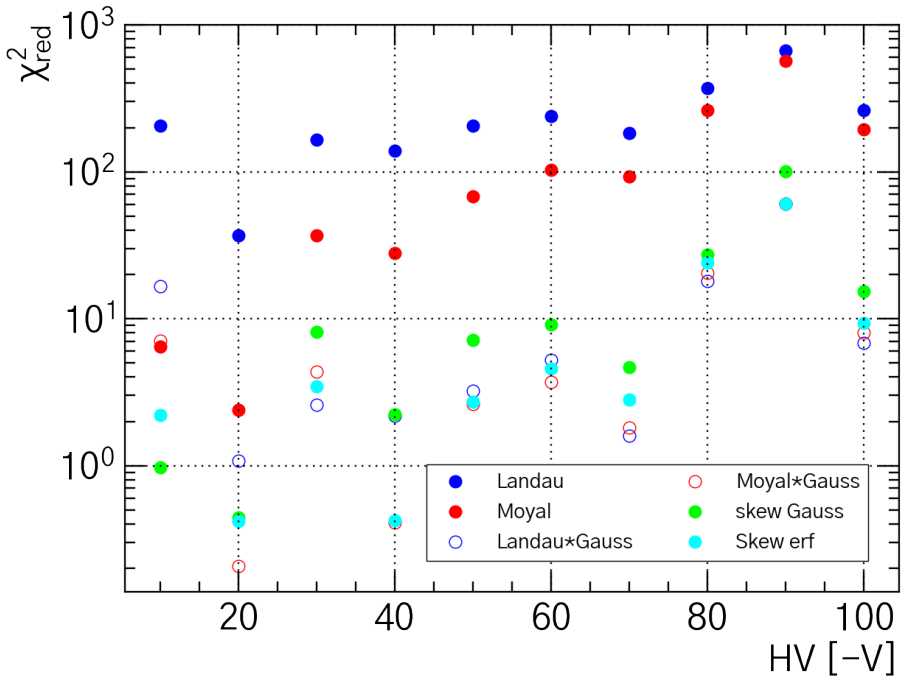

Figure 14.12: Reduced χ^2 of the efficiency curve fits for the HV-scan.

14.4. Determination of the underlying straggling functions

To determine the underlying straggling function the derivative of the efficiency curve is calculated. For the cases in which analytical expressions are complicated or do not exist, this is done numerically. From the obtained straggling functions the MPV and FWHM can be determined, also numerically. Errors for the MPV and FWHM are computed by the following procedure: The fit parameters obtained for the efficiency curve are randomly chosen according to a Gaussian distribution with the width of the according parameter error. Subsequently, the derivative is computed numerically and the MPV and FWHM are calculated. This is repeated sufficiently often and the standard deviation from the obtained MPV and FWHM distribution is used as the error of these values. Since the evaluation of the efficiency curves for the integrated Gauss-convolution of the Landau/Moyal is very CPU-intensive the number of repetitions in this procedure has been chosen to be 100, yielding a reasonable number of statistics to compute the standard deviation and keeping the computation time within reason. For the integrated Landau, Moyal and skewed Gauss the most probable value is given directly by a fit parameter and analytical forms for the FWHM can be calculated (see Appendix D).
For the integrated Langau and Gauss-convoluted Moyal distribution the fit parameters μ defining the peak position of the underlying Landau and Moyal, respectively, are not identical with the MPV as shown in Figure 14.13. As can be seen, the MPV is shifted towards higher values due to the convolution. This is caused by the asymmetry of the Landau and Moyal, respectively.

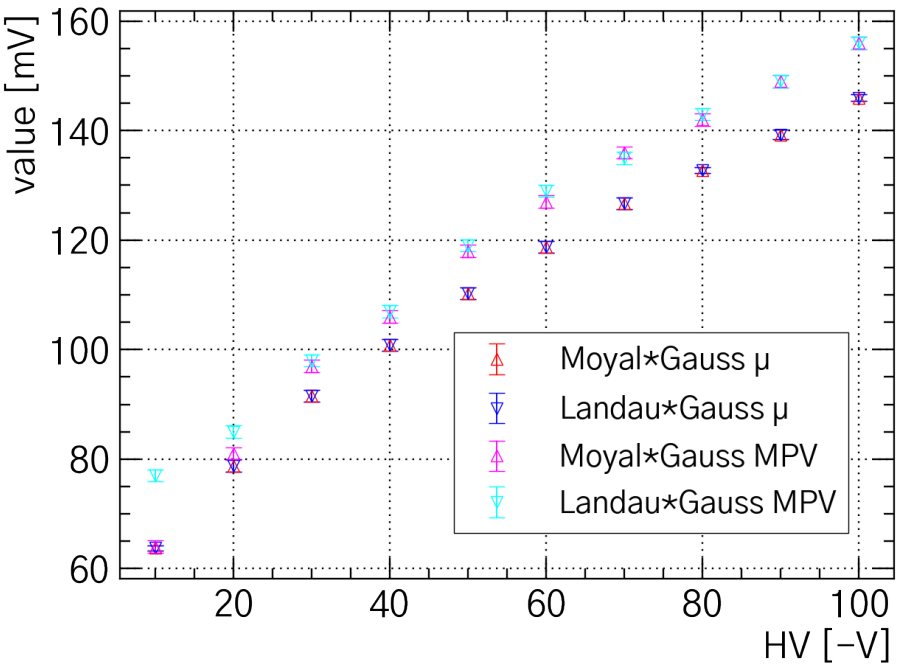

Figure 14.13: Comparison of the Landau/Moyal peak position and the MPV of the according Gauss convolution.

15. Sensor thickness

The method introduced in Section 11.2 in general can be used to determine the weighted sensor thickness (see Section 11.1). For this, the ratio of the peak position μ and the scaling parameter ξ of a Landau distribution are used. Since it has been found that the simple integrated Landau is not suitable to describe the efficiency curves, this model can not be applied here and different approaches are tested.
One way is to use the Langau model to obtain the Landau parameters μ and ξ from the fit. The ratio of these values is calculated and with this the thickness can be obtained according to Equation 11.12. The results for the ratio and the thickness are depicted in Figure 15.1 and Figure 15.2.

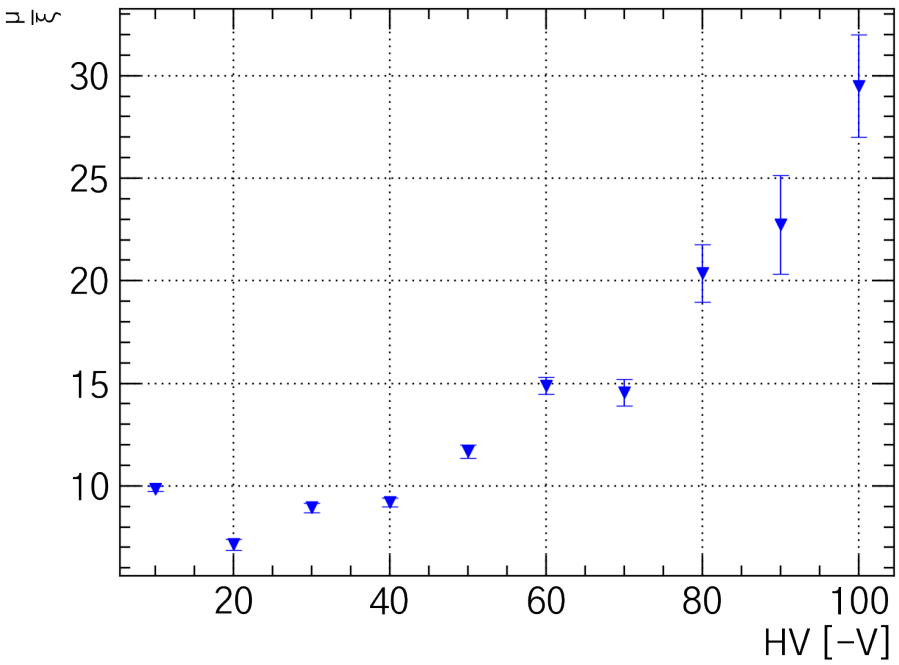

Figure 15.1: Ratio $\frac{\mu}{\xi}$ in the Langau model.

The sensor thickness show an HV dependence which seems exponential, reaching from highly nonphysical sensor thicknesses below 0.1 µm up to $\mathcal{O}(10^8\,\mu\text{m})$. This means, the relation between the ratio of the Landau peak position and width and the sensor thickness as derived in Section 11.2 gets lost if the correction for thin sensors (Gauss convolution as introduced in Section 10.3) is applied or systematic errors, which will be discussed in Section 16, strongly compromise the result. As not only the order of magnitude of the sensor thickness is not right, but also the exponential HV dependence is not consistent with the sensor thickness model

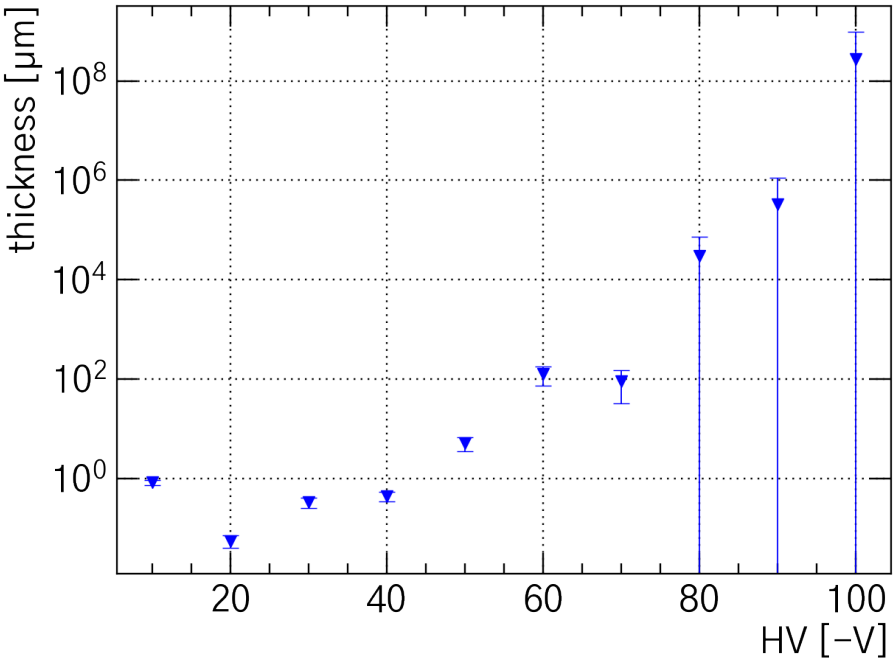

Figure 15.2: Sensor thickness from the ratio $\frac{\mu}{\xi}$ obtained with the Langau model.

presented in Section 11.1, this approach does not work in the framework used here. The ratios shown in Figure 15.1 depend exponentially on the HV, which is not expected from Equation 11.12. Since the thickness depends exponentially on the ratio and is expected to go roughly with the square root of the HV U (cf. Equation 9.7) one would assume the following relation

$$\frac{\mu}{\xi} \propto \frac{1}{2} \ln U + const.. \tag{15.1}$$

The observed relation in Figure 15.1 deviates strongly from this dependence. For a further study of the applicability of this approach, a quantitative knowledge of the systematic errors is needed in order to correct for them.
A second approach is the following: Instead of using the Landau-specific ratio $\frac{\mu}{\xi}$ one can look at the ratio of the MPV and the FWHM, which is defined for all straggling functions. For the Landau, the MPV is given by μ and the FWHM is $\approx 4.018\xi$ (see Section 10.3) and therefore

$$\frac{\mu_{Landau}}{\xi_{Landau}} = 4.018 \frac{MPV}{FWHM}\,. \tag{15.2}$$

Thus, Equation 11.12 can be written as

$$t\,[\mu\text{m}] = e^{4.018\frac{MPV}{FWHM} - 10.05}\,, \tag{15.3}$$

which can be applied to all models of straggling functions. The results obtained with this are shown in figure Figure 15.3.

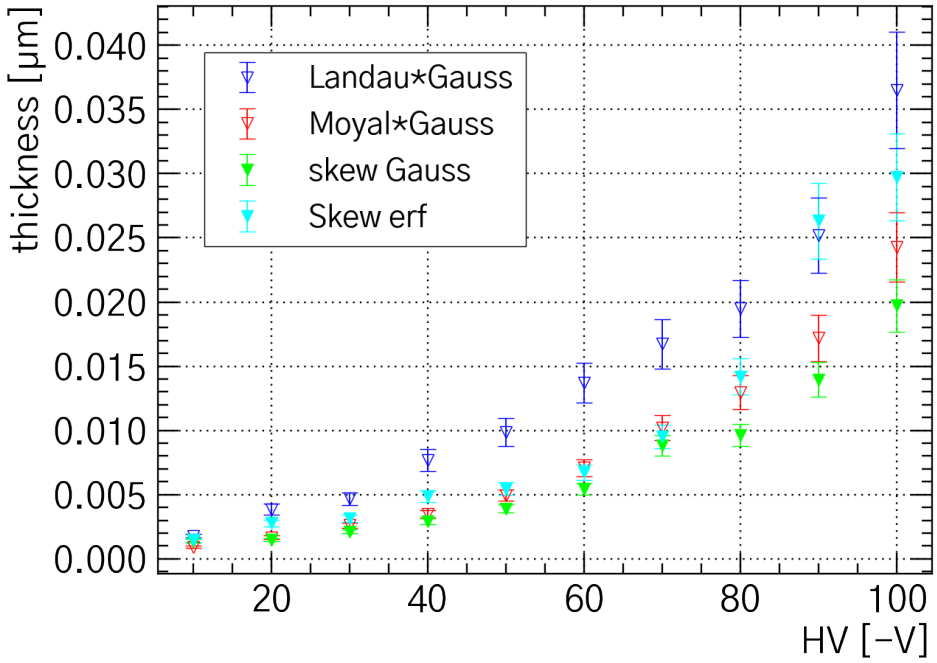

Figure 15.3: Thickness obtained from the ratio $\frac{MPV}{FWHM}$ for different models.

Also in this approach the order of magnitude for the sensor thickness is nonphysical ($< 0.1\,\mu m$) and the thickness rises exponentially with increasing HV values, which is expected to be unrealistic as aforementioned.
However, in contrast to the first approach, the relation between the ratios of the MPV and FWHM and the HV is more reasonable as for the exponential case in Figure 15.1 for the ratios $\frac{\mu}{\xi}$ obtained from the Langau model. The expected behavior in this case is

$$r(U) := \frac{MPV}{FWHM} \propto \frac{1}{8} \ln U + const\,. \tag{15.4}$$

This model can not describe the HV dependence of the ratios $r(U)$ of the MPV and FWHM.
Instead, a linear fit

$$r(U) = m \cdot U + c \tag{15.5}$$

for the skewed Gauss and skewed error function is found to work best, and a function of the form

$$r(U) = a \cdot \ln U + m \cdot U + c \tag{15.6}$$

is fitted to the Langau and Gauss-convoluted Moyal. The results are shown in Figure 15.4 and Figure 15.5 and the according parameters are listed in Table 15.1

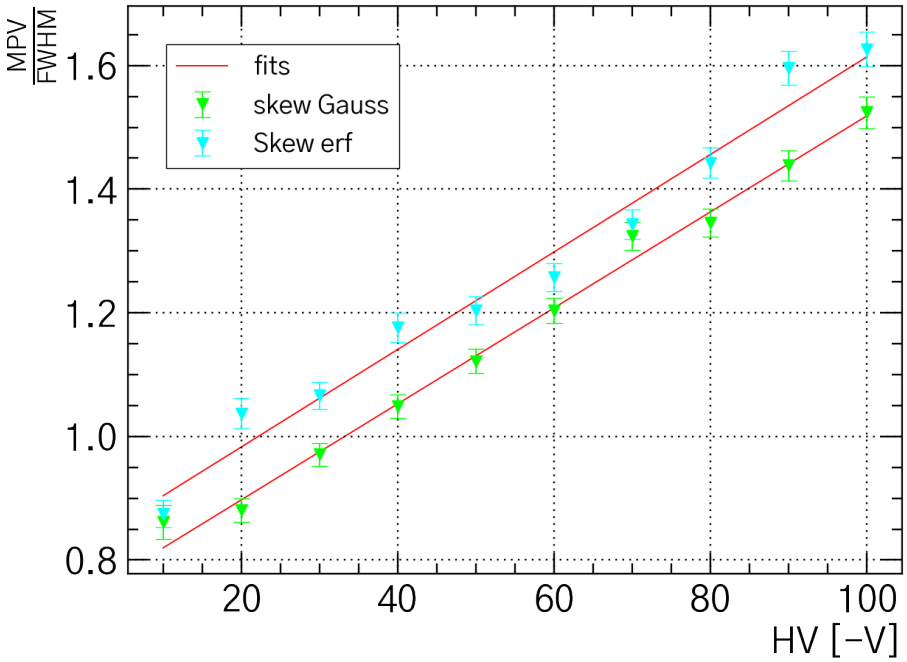

Figure 15.4: Linear fit to the ratio $\frac{MPV}{FWHM}$ for the skewed Gauss and skewed error function model.

	m	c	a
Langau	0.0036 ± 0.0007	0.51 ± 0.07	0.170 ± 0.029
Gauss-convoluted Moyal	0.0060 ± 0.0003	0.44 ± 0.03	0.113 ± 0.013
Skewed Gauss	$0.007\,77 \pm 0.000\,24$	0.742 ± 0.014	-
Skewed error function	0.0079 ± 0.0004	0.825 ± 0.025	-

Table 15.1: Fit result parameters for the fits according to Equation 15.5 and Equation 15.6 with the voltages in V.

The fits for the Langau and Gauss-convoluted Moyal according to Equation 15.6 describe the data particularly well. Thus, it is assumed that they can be used to determine the sensor thickness if a calibration is done. The knowledge of the actual sensor thicknesses for the data points would allow for such a calibration between the sensor thickness and the ratio $\frac{MPV}{FWHM}$. It is therefore assumed that with this calibration once done, the determination of the sensor thickness from just the ratio of the MPV and FWHM of the underlying straggling function, which can be obtained comparatively easy, is possible.

A problem with this method in general is the exponential dependence of the thickness on the ratio of the MPV and the FWHM. This means, errors have to be well in hand and understood quantitatively in order to correct for them. The exponential dependence in Equation 15.3 means that the relative error of the

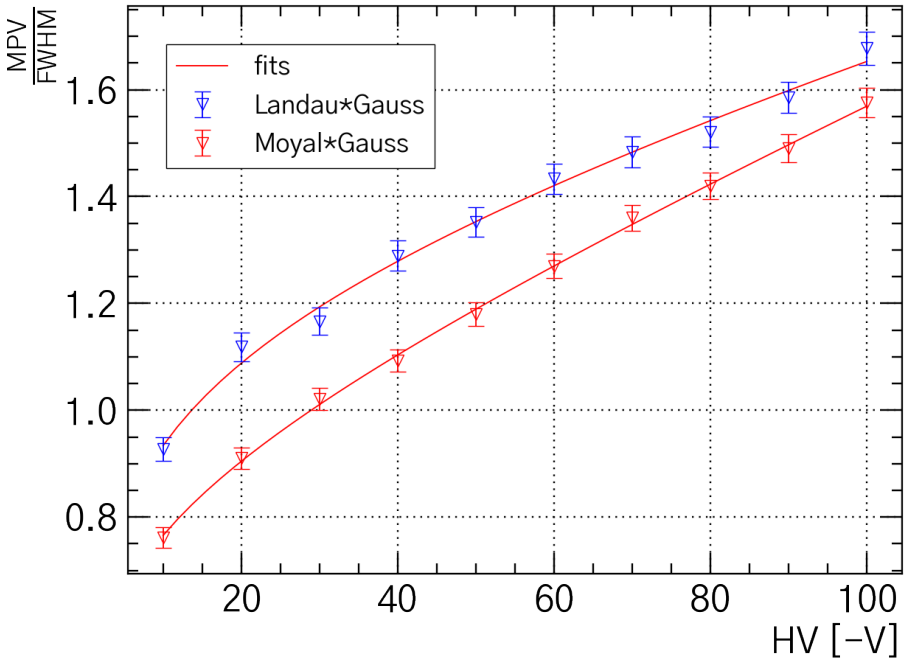

Figure 15.5: Fit to the ratio $\frac{MPV}{FWHM}$ for the Langau and Gauss-convoluted Moyal model.

thickness $\frac{\Delta t}{t}$ is given by roughly four times the absolute error Δr of the ratio $\frac{MPV}{FWHM}$:

$$\frac{\Delta t}{t} = 4.018 \Delta r \,. \tag{15.7}$$

Conclusion

16. Discussion and Summary

In this section the models and methods introduced in this thesis are discussed critically in view of the shown results, and potential possibilities for improvements are presented.
First, a diffusion model for charges in silicon has been presented as a starting point for a thereon based model for cluster formation in pixel detectors.
The characteristic quantity within this model is the diffusive spread of a particle given by the mean squared displacement (MSD). This quantity depends on properties of the charge and the material in which it is moving, as well as on the diffusion time. The material properties determining the spread show a strong temperature dependence, which means significant uncertainties on the diffusion had to be assumed for the model since the relevant temperature of the sensor material in unknown and expected to vary over time and depending on the sensor configurations. In order to minimize the systematic error that had to be regarded for this, cooling of the sensor to a constant temperature and a logging of the temperature to validate the cooling would be necessary.
The relevance of diffusion for signal generation in the MuPix10 has been assessed for electrons created inside and outside the depletion region of the sensor, i.e. with and without an external electric field. Subsequently, the MSD has been estimated for the two cases. Since charge collection is only relevant if it contributes to the signal height of the amplifier output, only charge collected before the signal peak is reached has to be regarded. Therefore the relevant diffusion time for the MSD calculation for an electron created outside the depletion zone is determined by the time between the charge deposition and the reaching of the peak of the amplifier signal. This time underlies statistical fluctuations and is also depending on the overall charge deposition. Thus, the resulting MSD obtained for this case can only be used as a rough estimation.
For the relevant diffusion time in the electric field of a p-n junction the drift time of the charge towards the collection electrode has been used. To calculate this time the mean electric field was calculated assuming a linear increase starting from the depletion depth and towards the junction – homogeneously over the whole pixel. This is known to be not completely right since in particular at the corners the electric field differs. It is however assumed to be a reasonable approximation. A crucial point in this model is the linear dependence of the drift time on the resistivity of the sensor, which is not known for the MuPix10 that was used. With this linear dependence of the drift time on the resistivity, the MSD is only

proportional to the square root of the resistivity, which in principle lowers the effect of the propagated errors on the error of the MSD. But with the range of the resistivity being as large as from 200 Ω cm to 400 Ω cm no significant predictions are possible with the cluster size model, which is based on this diffusion model. A more precise knowledge of the resistivity would be highly desirable.
The cluster size model introduced here uses a geometrical reasoning to obtain the fraction of clusters of size 1 to 4 by assuming a charge spread of created charge in the sensor. Depending on the position of the charge creation within one pixel the formation of a cluster of according size is assumed. For this, one has to assume the electric field to be the same over the whole sensor pitch which, as aforementioned, is not correct at the edges and especially at the corners. Since these parts have the largest impact on the cluster formation, this point is assumed to leave room for improvements, e.g. by using more sophisticated electrical field models obtained with TCAD. The incorrect electric field in the corners could well contribute to the differences of clusters of size 3 and 4 between the model and the measured data. If the electric field is lower in the pixel corners the drift time of charges created there would increase leading to a larger charge spread and thus larger clusters of size 3 and 4.
A difficulty in this model is the assumption of zero threshold. No data can be taken with zero threshold, the consequence being that the cluster size has to be extrapolated to this value from the cluster sizes obtained in a threshold scan. This extrapolation is done with an empirical fit without physical motivation. This means, the cluster size value at zero threshold obtained by this extrapolation depends on the chosen fit model and is not necessarily reasonable. The results can be improved by taking data with lower thresholds if procurable (a lower bound for the threshold is set by the noise level at which the hit rate of the sensor becomes to large to be read out).
Another uncertainty in this model is the initial spread of created charge due to kinetic energy gained in a collision with an ionizing particle. The spread of this has been estimated to be negligible for most charges, but the fraction of charges for which this is not the case is assumed to be in the order of the fraction of clusters of size 3 and 4. These fast charges can move away from the point of creation and lead to cluster sizes larger than predicted by the model. This is consistent with the result that the model in principle could work for clusters of size 1 and 2, but deviations are obtained for clusters of size 3 and 4. Intrinsically, the model deviates for clusters of size larger than 4. Such clusters can be produced by very high energetic δ-electrons, which are not taken into account in the model.
Finally, the validation of the model regarding the prediction of a mean cluster size is not possible since this value depends on the unknown resistivity. However, if the model is assumed to be suitable for the determination of the mean cluster size the resistivity obtained in turn is consistent with measurements that have been performed and indicate the resistivity to be rather close to 400 Ω cm than to 200 Ω cm.

Furthermore, models for the straggling distribution of ionizing particles in silicon have been presented and a method to obtain the sensor thickness from only the shape of a Landau distribution has been derived. This method has been applied to data obtained at a testbeam campaign.
In principle, the integral of the energy loss distribution of an ionizing particle

yields the efficiency curve of a sensor. This assumption has been used for the derivation of the relation between the distribution shape and the sensor thickness. In the following possible deviations from this assumption are presented.
First of all, the actual straggling function is not known but only modeled making certain assumptions (the full straggling function depends on the differential energy loss cross section, which is not known exactly). Therefore, these models, which are the starting point for the whole method used in the following, have to be chosen carefully taking into account their applicability. Different models for these functions have been used and the results are discussed below. However, even with a perfectly suitable model for the straggling function further errors can arise:
For a start, the energy loss which is described by the model of the straggling function is not necessarily equal to the energy deposition. Energy that is lost by the particle can in principle leave the detector. For radiative losses this is nearly always the case for thin silicon detectors. For very thin sensors even fast δ-electrons caused by ionization losses can leave the sensor in principle and remain undetected. This has an effect on the distribution of deposited energy in a way that its tail towards high energies becomes less pronounced.
A second, effect causing differences between the (integral of the) initially modeled straggling function and the finally obtained efficiency curve is the non-linearity of the amplifier. For the method used to determine the sensor thickness, a linear relation between the energy loss of a particle and the corresponding amplifier output signal has to be assumed. This assumption is expected to be incorrect especially for very high charge depositions in which the saturation of the amplifier becomes important. This effect can be assessed and also corrected for by an energy calibration, which thus would be desirable for an improvement of the method of the sensor thickness determination.
Further deviations are caused by the comparator, which does not respond to very small ToTs and hereby causes an offset of the zero threshold for the actually observed straggling distribution. Another effect causing differences between the physical straggling function and the observed one is the recombination of charge carriers in the sensor yielding an overall shift of the distribution.
The noise in the readout procedure is expected to be a minor problem if its extent is known. In this case this can be regarded for by fitting a convolution of the straggling function model with a Gauss of width corresponding to the noise.
The models for the straggling function in principle have to be cut at zero threshold and at the amplifier saturation and set to zero beyond these cuts since signals in these regions can not be obtained.
The performance of the different models for the straggling functions that have been used is compared and discussed in the following.
As has been expected, the simple Landau distribution can not describe the energy loss fluctuations in the thin sensors in which the effect of the in the Landau theory assumed but incorrect energy loss cross section becomes perceptible.
The Moyal distribution with a smaller tail towards higher energies than the Landau is working empirically for very thin sensors. The reason could be that the escape of δ-electrons plays an important role here making the small-tailed Moyal distribution a suitable model.
The skewed Gauss and skewed error function are suitable functions that can be

used to describe the efficiency curves empirically for the whole range of HV values, and thus sensor thicknesses, applied here. For these models a clear dependence of the fit parameters on the HV could be obtained. The models are empirical and therefore no relation to physical quantities could be obtained. It is however assumed that a calibration of these values to the sensor thickness can be done and used universally. A problem with these models are the correlations of the fit parameters, which are assumed to make the fit unstable.
The models using the Gauss-convoluted Landau and Moyal suit the data of the efficiency curves well but also for these models strong parameter correlations are obtained.
For the efficiency curves that have been fitted an error on the efficiency and on the threshold of the corresponding efficiency data point is given. The error on the efficiency becomes negligibly small for large statistics (many particle tracks). In that case the threshold errors are dominating. Thus, for more precise results of the efficiency curves it would be desirable to measure the threshold more precisely. In this case an estimation of the fluctuations of the threshold would be possible and the dominating error. Furthermore, it has been found that to obtain a stable fit of the efficiency curve, data in the low threshold region (efficiencies close to 100 %) and for high thresholds (efficiencies close to 0 %) are needed. Measurements in these regions are expected to improve the results of the fits and also allow for an assessment of the validity of the used model in the region of high energy transfers (tail region corresponding to low efficiencies, i.e. high thresholds).

With the different models fitted to the efficiency curve the underlying straggling function parameters could be obtained and the method for the sensor thickness determination could be tested.
At first, the meaning of the sensor thickness in this context has to be understood. The sensor thickness in the physical model of the straggling functions corresponds to the range in which an ionizing particle looses energy. Since, in the case of the sensors used here, not all energy that is lost is actually measured, the thickness corresponding to the measured deposited energy is considered to be the sensor thickness. This is the thickness from which charge is collected and contributes to the signal height. It has to be assumed that the contribution of the deposited charge to the signal height depends on the depth in which the charge was created: Charge created in the electronics part is assumed to be negligible since the chance of it to be captured by the transistors is large. Charge created in the depletion region is assumed to contribute fully to the signal meaning that every charge created in this region is assumed to be collected and independently of where in the depletion region the creation took place. Finally, charge created beyond the depletion region can in principle contribute to the signal via diffusion as has been aforementioned. The contribution is modeled to depend in a Gaussian shape on the distance to the depletion region. A rough estimation for the width of the corresponding Gauss can be achieved with the presented diffusion model. It is not taken into account within this model that charge is possibly captured at the backside of the sensor due to cracks or impure manufacturing.
With this a model for a weighted sensor thickness has been introduced, which corresponds to the sensor thickness used in the context of the method of the sensor thickness determination from the shape of the straggling function.

This method has been derived using the Landau theory and uses only the ratio of the MPV and the width of the straggling distribution. Thus, in contrast to the some other methods to determine the sensor thickness from the straggling function no energy calibration is needed for this method. But a straight problem is the derivation using the Landau theory since the Landau distribution is not applicable for the thin sensors. Therefore, different approaches had to be taken. The first one was to use the Landau parameters obtained from the suitable fit of a Langau. However, the results that have been found in this case are nonphysical and it thus has to be assumed that either the relation between sensor thickness and straggling distribution shape derived from the Landau theory is lost for the advanced method of the Gauss-convoluted Landau or the systematic errors discussed above compromise the results.
The second approach taken was to derive a relation between the universal parameters of the MPV and FWHM and the sensor thickness from the initially derived relation. The results obtained with this also showed a nonphysical behavior leading to the conclusion that the introduced method either is not applicable for thin sensors intrinsically due to a wrong model or the systematic errors are dominating and have to be corrected for in order to make the presented method applicable.
Additionally, a big problem with the derived relation is the exponential dependence of the sensor thickness on the parameters defining the shape of the straggling function. This means the absolute error of the parameter in the exponent yields the relative error of the thickness. This potentially results in such large errors that no significant results can be obtained.

Finally, it is assumed that for a straggling function shape dependent sensor thickness determination a calibration to a chosen property of the straggling function is required, which afterwards can be used universally.

17. Outlook

In the course of this thesis data have been taken at a further testbeam campaign, which will allow for an enhancement of the studies performed in the scope of this thesis. Especially, the importance of diffusion is expected to be assessed analyzing the data obtained in HV-scans for sensors of different actual thicknesses. A qualitative study of this is possible even without an energy calibration.
However, as has been mentioned several times throughout this thesis, an energy calibration is desirable anyhow. Important information on the sensor can be obtained from such an, albeit complex, calibration and with the determination of the sensor resistivity, this will also allow for a theoretical calculation of the depletion depth and further checks of the models presented in this thesis.

Appendix

A. Noise hit probability

The formula for the noise hit probability q due to reference layer inefficiencies is obtained by the assumption of independent inefficiencies. In this case, the number of inefficient reference layers for a particle track follows a binomial distribution $B(k|n,\iota)$ with $0 \leq k \leq n$ being the number of inefficient reference layers, $n = 3$ the number of reference layers and ι the probability of one reference layer being inefficient. The probability q is then given by the probability of at least one inefficient reference layer times the probability ϵ_{DUT} of the DUT being efficient:

$$q = (B(1|3,\iota) + B(2|2,\iota) + B(3|3,\iota))\,\epsilon_{DUT} \tag{A.1a}$$
$$= (3\iota(1-\iota)^2 + 3\iota^2(1-\iota) + \iota^3)\epsilon_{DUT} \tag{A.1b}$$
$$= \iota(\iota^2 - 3\iota + 3)\epsilon_{DUT}\,. \tag{A.1c}$$

For different efficiencies of the DUT and reference layers the probability q is plotted in Figure A.1 and Figure A.2.

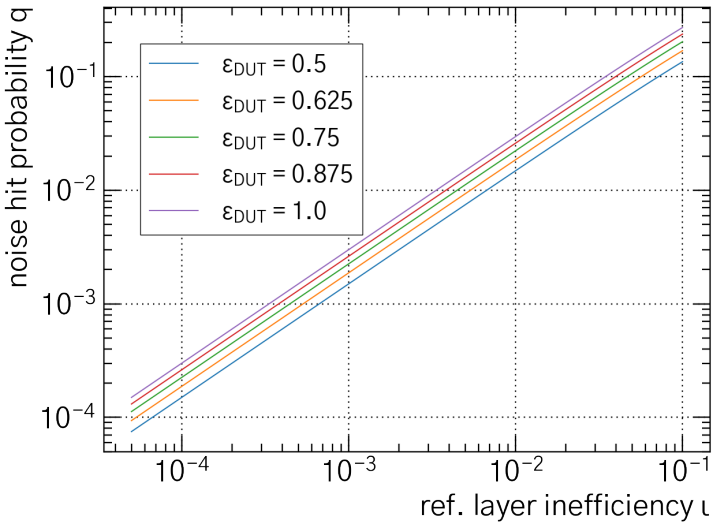

Figure A.1: Probability for a noise hit due to reference layer inefficiencies for different DUT efficiencies.

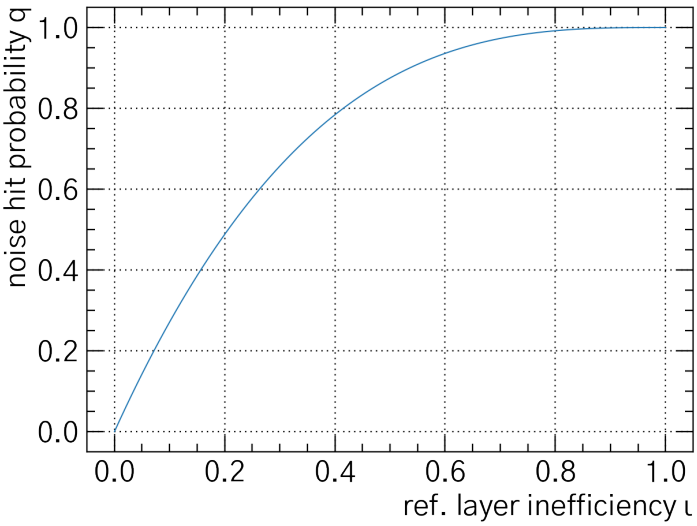

Figure A.2: Probability for a noise hit due to reference layer inefficiencies for a fully efficient DUT.

B. Pixel resolution

The spatial resolution of a sensor with pixel size $d_x \times d_y$ is computed as following: The probability distribution $p_x(x)$ (exemplarily for the x-direction here) for a hit within a pixel is equal for the whole pixel pitch and zero elsewhere since no spatial information about the hit position within the pixel is provided. The probability distribution has to be normalized and is therefore

$$p_x(x) = \frac{1}{d_x}\theta(x - d_x/2)\theta(d_x/2 - x) \tag{B.1}$$

with the step-function $\theta(x)$. The mean μ_x of this distribution is zero and the variance is

$$\sigma_x^2 = \int_{-\infty}^{\infty} p_x(x)x^2 dx - \mu_x^2 \tag{B.2a}$$

$$= \frac{1}{d_x}\int_{-d_x/2}^{d_x/2} x^2 dx \tag{B.2b}$$

$$= \frac{d_x^2}{12}\,. \tag{B.2c}$$

This yields a spatial resolution of

$$\sigma_x = \frac{d_x}{\sqrt{12}}\,. \tag{B.3}$$

C. Skewed Gauss distribution

The skewed Gauss distribution as presented in Equation 10.3 is applicable for the description of straggling functions only empirically in a reasonable parameter range. There are, however, fundamental systematic dissents from the physically motivated straggling functions.
A skewed Gauss with scaling factor $\mathcal{N}$ is given (see Equation 10.3) by

$$f(\lambda) = \mathcal{N} \exp\left(-\frac{1}{2} \frac{1}{\left(\frac{\sigma_0}{\lambda - \mu} + \sigma_a \right)^2} \right). \tag{C.1}$$

This function does not, as expected for a straggling function, converge to zero for high energies ($\lambda \to \infty$), but the limit is

$$f(\lambda \to \infty) = \mathcal{N} \exp\left(-\frac{1}{2\sigma_a^2} \right). \tag{C.2}$$

For a sufficiently small asymmetry, this however does not compromise the fit. E.g., for $\sigma_a \lesssim 0.2$ the ratio of the limit and the peak height at $\lambda = \mu$ is smaller than 10^{-5}. The shape of the skew Gauss is depicted in Figure C.1 for a σ_a of 0.2 and 1.0, respectively. As can be seen, for $\sigma_a = 0.2$ the shape of a straggling function in general is modeled adequately.

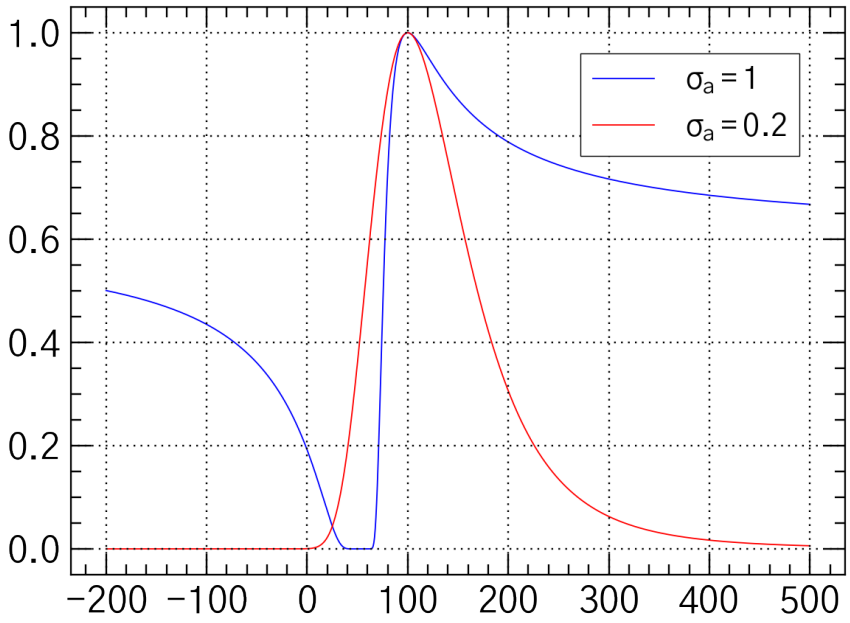

Figure C.1: Comparison of a skewed Gauss with $\mu = 100$, $\sigma_0 = 45$ for two values of σ_a.

D. Analytical expressions for the MPV and FWHM

The MPV and FWHM of the straggling function models introduced in Section 10 are used for further analysis, in particular for the determination of the sensor thickness according to the model introduced in Section 11.2. For the models of the simple Landau and Moyal distribution and the skewed Gauss the MPV and FWHM can be determined directly from the fit parameters. For the convolutions and the skewed error function no closed expression for the MPV and the FWHM have been found and they are computed numerically. The relations for the analytical results are presented in the following.

D.1. Landau distribution

For the Landau distribution the determination of the MPV and the FWHM from the fit parameters is plain. With the parametrization as in Equation 10.7 the MPV is given by

$$MPV = \mu \tag{D.1}$$

and the FWHM is

$$FWHM = 4.018 \cdot \sigma\,. \tag{D.2}$$

D.2. Moyal distribution

To determine the MPV of the Moyal distribution given in Equation 10.8 one can use the derivative

$$s'(\lambda) \propto e^{-\frac{1}{2}\left(\lambda + e^{-\lambda}\right)} \left(1 - e^{-\lambda}\right) \stackrel{!}{=} 0 \tag{D.3}$$

$$\Leftrightarrow \quad e^{-\lambda} = 1 \tag{D.4}$$

$$\Leftrightarrow \quad \lambda = 0\,. \tag{D.5}$$

With the transformation in Equation 10.9 this means the peak position (MPV) is

$$MPV = \mu\,. \tag{D.6}$$

With this, the FWHM is obtained by determining the positions $\lambda_{1,2}$ at which the function has the half of the height of the peak:

$$\frac{s(\lambda_{1,2})}{s(0)} = \frac{1}{2} \tag{D.7}$$

$$\Leftrightarrow \quad \lambda_{1,2} + e^{-\lambda_{1,2}} = 1 + \ln\sqrt{2} \tag{D.8}$$

$$\Rightarrow \quad \lambda_1 \approx -1.30634 \quad \vee \quad \lambda_2 \approx 2.28447\,. \tag{D.9}$$

To solve this equation the Lambert W function is used [54].
Regarding the re-scaling in Equation 10.9 the FWHM is then obtained as

$$FWHM = (2.28447 + 1.30634)\sigma = 3.59081\sigma\,. \tag{D.10}$$

D.3. Skewed Gauss

As can be seen in Figure C.1 the skewed Gauss (defined in Equation 10.3) has two extreme points. The same result can be obtained by investigating the derivative:

$$s'(\lambda) \propto \exp\left(-\frac{1}{2}\frac{1}{\left(\frac{\sigma_0}{\lambda-\mu} + \sigma_a\right)^2}\right)\frac{\sigma_0(\lambda-\mu)}{\left(\sigma_a(\lambda-\mu)+\sigma_0\right)^3} \stackrel{!}{=} 0 \tag{D.11}$$

$$\Leftrightarrow \lambda_1 = \mu - \frac{\sigma_0}{\sigma_a} \quad \vee \quad \lambda_2 = \mu\,. \tag{D.12}$$

The first result (λ_1) is the minimum, which goes to minus infinity for small values of σ_a. The maximum is at the position $\lambda_2 = \mu$ yielding

$$MPV = \mu\,. \tag{D.13}$$

This value can be used to determine the FWHM from the two values $\lambda_{3,4}$ at which the function has half the height of the peak:

$$\frac{s(\lambda_2)}{s(\lambda_{3,4})} \stackrel{!}{=} 2 \tag{D.14}$$

$$\Leftrightarrow \quad \left(\frac{\sigma_0}{\lambda_{3,4}-\mu} + \sigma_a\right)^2 = \frac{1}{2\ln 2}\,. \tag{D.15}$$

For the relevant range of σ_a (see Appendix C) this is the case if

$$\lambda_3 = \frac{\sqrt{\alpha}\mu + \sigma_0 - \sigma_a\mu}{\sqrt{\alpha} - \sigma_a} \quad \vee \quad \lambda_4 = \frac{\sqrt{\alpha}\mu - \sigma_0 + \sigma_a\mu}{\sqrt{\alpha} + \sigma_a} \tag{D.16}$$

with the definition $\alpha = \frac{1}{2\ln 2} \approx 0.7213$.
Finally the FWHM can be computed by the difference of the two values:

$$FWHM = \frac{2\sqrt{\alpha}\sigma_0}{\alpha - \sigma_a^2}\,. \tag{D.17}$$

List of Tables

List of Figures

References

[1] Pauline Gagnon. *The Standard Model: a beautiful but flawed theory.* URL: https://www.quantumdiaries.org/2014/03/14/the-standard-model-a-beautiful-but-flawed-theory/.

[2] The Super-Kamiokande Collaboration and Y. Fukuda et al. "Evidence for oscillations of atmospheric neutrinos". In: *Physical Review Letters* 81:1562-1567 (1998).

[3] Particle Data Group. *Muon properties.* URL: https://pdg.lbl.gov/2020/listings/rpp2020-list-muon.pdf.

[4] D. Wiedner and N. Berger. *Public Mu3e Web Site at PSI.* URL: https://www.psi.ch/de/mu3e/introduction.

[5] Asmaa Abada et al. "Enhancing lepton flavour violation in the supersymmetric inverse seesaw beyond the dipole contribution". In: *Journal of High Energy Physics* (2012). DOI: 10.1007/JHEP09(2012)015.

[6] M. Malinsky, J. C. Romao, and J. W. F. Valle. "Novel Supersymmetric SO(10) Seesaw Mechanism". In: *Physical Review Letters* (2005). DOI: 10.1103/PhysRevLett.95.161801.

[7] A. Blondel et al. *Research Proposal for an Experiment to Search for the Decay $\mu \to eee$.* 2012. URL: https://www.psi.ch/sites/default/files/import/mu3e/DocumentsEN/ResearchProposal.pdf.

[8] *The Mu3e Experiment.* URL: https://www.physi.uni-heidelberg.de/Forschung/he/mu3e/wiki/index.php/File:Schematic-9.png.

[9] K. Arndt et al. "Technical design of the phase I Mu3e experiment". In: *Nuclear Instruments and Methods in Physics Research Section A* 1014 (2021). DOI: 10.1016/j.nima.2021.165679.

[10] Hermann Kolanoski and Norbert Wermes. *Teilchendetektoren.* 2016. DOI: 10.1007/978-3-662-45350-6_1.

[11] *Detektoren.* URL: https://physik.fandom.com/de/wiki/Detektoren.

[12] Stephen M. Seltzer and Martin J. Berger. "Evaluation of the collision stopping power of elements and compounds for electrons and positrons". In: *The International journal of applied radiation and isotopes* 33 (1982), pp. 1189–1218. DOI: 10.1016/0020-708X(82)90244-7.

[13] R.M. Sternheimer. "The Density Effect for the Ionization Loss in Various Materials". In: *Physical Review* 88.4 (1952), pp. 851–859.

[14] Particle Data Group and S. Eidelman et al. "Review of Particle Physics". In: *Physics Letters B* 592 (2004). DOI: 10.1016/j.physletb.2004.06.001.

[15] Bruno Benedetto Rossi. *High-energy particles.* Prentice-Hall physics series. New York, NY: Prentice-Hall, 1952.

[16] J.E. Moyal. "Theory of Ionization Fluctuations". In: *The London, Edinburgh, and Dublin Philosophical Magazine and Journal of Science* 46:374 (1955), pp. 263–280. DOI: 10.1080/14786440308521076.

[17] Bernhard Ketzer. *Gaseous Detectors*. 2017. URL: https://indico.cern.ch/event/630418/contributions/2813727/attachments/1577581/2491690/ketzer_lecture1b_sub.pdf.

[18] Hans Bichsel. "Straggling in thin silicon detectors". In: *Reviews of Modern Physics* 60 (1988), pp. 663–699.

[19] "Review of Particle Physics". In: *Journal of Physics G: Nuclear and Particle Physics* 37 (2010). DOI: 10.1088/0954-3899/37/7A/075021.

[20] Gert Molière. "Theorie der Streuung schneller geladener Teilchen II Mehrfach-und Vielfachstreuung". In: *Zeitschrift für Naturforschung A* 3 (1947), pp. 78–97. DOI: 10.1515/zna-1948-0203.

[21] *Band gap Band diagram Valence and conduction bands*. URL: https://www.pngwing.com/en/free-png-hhwwx.

[22] *Silicon*. URL: https://en.wikipedia.org/wiki/Silicon.

[23] *Halbleitertechnologie von A bis Z*. URL: https://www.halbleiter.org/grundlagen/dotieren/.

[24] *Depletion region*. URL: https://en.wikipedia.org/wiki/Depletion_region.

[25] L. Vigani et al. "Study of prototypes of LFoundry active and monolithic CMOS pixels sensors for the ATLAS detector". In: *Journal of Instrumentation* 13 (2018). DOI: 10.1088/1748-0221/13/02/C02021.

[26] H. Augustin et al. "The MuPix high voltage monolithic active pixel sensor for the Mu3e experiment". In: *Journal of Instrumentation* 10 (2015). DOI: 10.1088/1748-0221/10/03/C03044.

[27] Alena Weber, Heiko Augustin, and Ivan Perić. *MuPix10 Documentation*. 2021. URL: https://www.physi.uni-heidelberg.de/Forschung/he/mu3e/restricted/notes/Mu3e-Note-0052-MuPix10_Documentation.pdf.

[28] David Maximilian Immig. *The Very Large HV-MAPS Tracking Telescope*. 9th Beam Telescopes and Test Beams Workshop. 2021. URL: https://indico.cern.ch/event/945675/contributions/4184873/attachments/2186614/3694678/bttb9_immig.pdf.

[29] Marius Wilm Menzel. "Calibration of the MuPix10 Pixel Sensor for the Mu3e Experiment". Bachelor thesis. University of Heidelberg, 2020.

[30] Florian Frauen. "Characterisation of the time resolution of the MuPix10 pixel sensor". Bachelor thesis. University of Heidelberg, 2021.

[31] Private communication with David Maximilian Immig (09/2021).

[32] Heiko Augustin et al. "MuPix10: First Results from the Final Design". In: *Physics Instrumentation and Detectors* (2020).

[33] Lennart Huth. "A High Rate Testbeam Data Acquisition System and Characterization of High Voltage Monolithic Active Pixel Sensors". PhD thesis. University of Heidelberg, 2018. DOI: 10.11588/heidok.00025785.

[34] Adrian Herkert. "Characterization of a Monolithic Pixel Sensor Prototype in HV-CMOS Technology for the High-Luminosity LHC". PhD thesis. University of Heidelberg, 2020. DOI: 10.11588/heidok.00027893.

[35] Private communication with Heiko Augustin.

[36] H. Augustin et al. “Performance of the large scale HV-CMOS pixel sensor MuPix8”. In: (2018). Prepared for submission to JINST. DOI: 10.1088/1748-0221/14/10/C10011.

[37] E.J. Schioppa et al. “Study of Charge Diffusion in a Silicon Detector Using an Energy Sensitive Pixel Readout Chip”. In: *IEEE Transactions on Nuclear Science* 62.5 (2015). DOI: 10.1109/TNS.2015.2475124.

[38] *Einstein relation*. URL: https://en.wikipedia.org/wiki/Einstein_relation_(kinetic_theory).

[39] Inc. Virginia Semiconductor. *Resistivity and Carrier Transport Parameters in Silicon*. URL: https://www.virginiasemi.com/pdf/ResistivityCarrierTransportinSilicon.pdf.

[40] Stephan Lachnit. “Pulse Shape Characterization and Allpix Squared Simulation of the MuPix10”. Bachelor thesis. University of Heidelberg, 2021.

[41] Jörg Vollrath. *Elektronik 3*. URL: https://personalpages.hs-kempten.de/~vollratj/Elek3/2017_09_12_03_Elektronik3_Halbleiter.html.

[42] “Geant4 physics processes for microdosimetry simulation: Very low energy electromagnetic models for electrons in silicon”. In: *Nuclear Instruments and Methods in Physics Research B* 288 (2012), pp. 66–73. DOI: 10.1016/j.nimb.2012.07.028.

[43] J.F. Bak et al. “Large departures from Landau distributions for high-energy particles traversing thin Si and Ge targets”. In: *Nuclear Physics B* 288 (1987), pp. 681–716.

[44] F. Campabadal et al. “Beam tests of ATLAS SCT silicon strip detector modules”. In: *Nuclear Instruments and Methods in Physics Research* 538 (2005), pp. 384–407. DOI: 10.1016/j.nima.2004.08.133.

[45] *Numerical Gauss and Landau convolution*. code provided by David Maximilian Immig.

[46] Lev Davidovich Landau. “On the energy loss of fast particles by ionization”. In: *J. Phys. U.S.S.R.* 8, 201 (1944).

[47] *ROOT Data Analysis Framework*. URL: https://root.cern/.

[48] *Algorithm for Landau PDF*. URL: https://root.cern.ch/doc/master/PdfFuncMathCore_8cxx_source.html#l00021.

[49] D. Passeria S. Meroli and L. Servolia. “Energy loss measurement for charged particles in very thin silicon layers”. In: *Journal of Instrumentation* 6 (2011).

[50] S. Hancock et al. “Energy loss and energy straggling of protons and pions in the momentum range 0.7 to 115 Gev/c”. In: *Physical Review A* 28.2 (1983), pp. 615–620.

[51] Private communication with Luigi Vigani (09/2021).

[52] *ROOT TEfficiency class Reference*. URL: https://root.cern.ch/doc/master/classTEfficiency.html.

[53] *iminuit package*. URL: https://iminuit.readthedocs.io/en/stable/.

[54] *Lambert W-Function*. URL: https://mathworld.wolfram.com/LambertW-Function.html.

Acknowledgments

First of all I want to thank Prof. Dr. André Schöning, who gave me the great opportunity to work on this thesis and the interesting topic that are the HV-MAPS and pixel detectors in general.

I am also very thankful to Prof. Dr. Silvia Masciocchi for being the second examiner of this thesis.

Particularly, I want to thank David Immig, Dohun Kim, Heiko Augustin and Dr. Luigi Vigani for the much and valuable time they spent answering all my questions regarding the broad topic of data analysis and pixel detectors.
I would also like to thank Stephan Lachnit for providing me with answers to all my questions regarding simulations.

I am grateful to Benjamin, David, Dohun, Jan, Julian, Sebastian and Thomas for reading this thesis.

Furthermore, thanks are due to all of the Mu3e and ATLAS group for making my time during the work on this thesis a great time.

Finally, I owe my deepest gratitude to my parents and brothers for their continuous love and support.

Erklärung

Ich versichere, dass ich diese Arbeit selbstständig verfasst und keine anderen als die angegebenen Quellen und Hilfsmittel benutzt habe.

Heidelberg, den 07.10.2021